Article:
Xin, C., Zeng, L., Wang, Z. orcid.org/0000-0002-4054-0533 et al. (4 more authors) (2025) Characterizing Dynamic Responses of Rock Slopes to Near-Fault Pulse-Like Ground Motions. Rock Mechanics and Rock Engineering. ISSN: 0723-2632

https://doi.org/10.1007/s00603-025-04798-w

Characterizing Dynamic Responses of Rock Slopes to Near-Fault Pulse-Like Ground Motions

Chunlei Xin [a, b], Lei Zeng [b], Zhao Wang [c*], Wenkai Feng [a, b*], Fei Yang [d], Iman Hajirasouliha [e], Xinyuan Yu [e]

[a] *State Key Laboratory of Geohazard Prevention and Geoenvironment Protection, Chengdu University of Technology, Chengdu, China*

[b] *College of Environment and Civil Engineering, Chengdu University of Technology, Chengdu, China*

[c] *Institute for Transport Studies, University of Leeds, Leeds, UK*

[d] *Institute of Mountain Hazards and Environment, Chinese Academy of Sciences, Chengdu 610299, China*

[e] *School of Mechanical, Aerospace and Civil Engineering, The University of Sheffield, Sheffield, UK*

**Corresponding author Email: z.wang13@leeds.ac.uk; fengwenkai@cdut.cn*

Abstract:

This research examines the dynamic response and failure mechanisms of slopes in near-fault regions subjected to pulse-like ground motions (PLGM). Utilizing shaking table tests and numerical simulations, a categorization method is developed using the analytic hierarchy process (AHP) to assess the effects of PLGM quantitatively. An energy-based approach, incorporating the ratio of seismic energy release (RSER), quantifies dynamic response variations more accurately. Results indicate that the acceleration amplification factor (AAF) values for PLGM (QP, MY, and LD seismic motions) are 114.22%, 62.22%, and 31.11% higher than those for NPLGM (WL seismic motion) at the slope shoulder (A8), and 131.1%, 73.33%, 44.44% higher at the trailing edge of slope top (A9). Additionally, the Arias intensity amplification factor (AlAF) values for PLGM are 397.26%, 195.33%, and 64.32% stronger than those for NPLGM at A8, demonstrating that PLGM amplifies the dynamic response compared to NPLGM at increased elevations. Disaggregated average amplification factors (DAAF) analysis shows that PLGM trigger diverse responses based on their characteristics, with pronounced nonlinear amplification effects as elevation increases. Peak Fourier spectrum amplitude (PFSA) analysis shows that high rock masses are particularly sensitive to the high-frequency components of PLGM, while wavelet package transform analysis confirms that energy release is concentrated in the velocity pulse segment, significantly influencing the frequency domain response at various elevations. Seismic motions with different pulse characteristics induce varied behaviors, with higher frequency components causing stronger responses. These insights enhance understanding of rock slope responses in near-fault earthquakes and support seismic slope design in such regions.

Keywords: Rock slopes; Shaking table test; Pulse-like ground motions; Dynamic response analysis; Numerical

simulation.

Highlights

- Quantitatively analyzed differences in pulse-like ground motions using DAAF.
- Observed shifts in high-frequency components of PLGM along slope elevation.
- Demonstrated a strong correlation between pulse energy and time-frequency domain responses.
- Explained the destructiveness of NPLGM and PLGM through AIAF and RSER.

1 Introduction

The southwestern region of China is predominantly characterized by mountainous terrain, resulting in the widespread presence of natural slopes. With population growth and economic development, many important projects, such as highways, hydropower stations, railways, and airports, are being constructed on these natural slopes. The unique terrain conditions have resulted in the formation of numerous cut slopes due to extensive highway construction, with bedding rock slopes being particularly prevalent in this region (Miao et al., 2024). The region straddles two major seismic zones, the Circum-Pacific seismic zone to the east and the Himalayan seismic belt to the west, making it one of the most seismic-prone areas globally. Southwest China, encompassing Sichuan, Yunnan, and Guizhou, lies at the intersection of China's north-south seismic belt and the southeastern margin of the Qinghai-Tibet Plateau. This unique geological position, shaped by the ongoing collision between the Indian and Eurasian plates, renders the region highly susceptible to seismic activity, with active fault zones such as the Longmenshan, Xianshuihe, and Xiaojiang faults inducing major earthquakes (Cui et al., 2024). Historical records indicate that the region is capable of producing earthquakes with magnitudes as high as 8.0, as evidenced by seismic events such as the 2008 Wenchuan (Mw 8.0), 2013 Ya'an (Mw 7.0), and 2014 Ludian (Mw 6.5). While such large earthquakes are infrequent, the area's complex geological structure and active fault zones maintain a consistently elevated seismic risk (Fan et al., 2016). Furthermore, the vast land area has numerous active faults. During a major earthquake, the stress released by fault rupture generates strong ground motion that propagates in the surrounding regions (Zou et al., 2017). However, these strong earthquakes exhibit variable intensity and impact along fault lines. A notable example is the Mw 6.5 earthquake that struck Ludian County, Zhaotong City, Yunnan Province, on 3rd August 2014. The China Seismic Network Center reported the epicenter to be located at 27.10º N, 103.34º E, with a focal depth of 12 km. The earthquake was caused by the Baogunao-Xiaohe fault, a branch of the Zhaotong-Ludian fault (Zhou et al., 2024). This medium-strong earthquake occurred in the boundary tectonic zone between the Sichuan-Yunnan rhombic block and the South China block on the southeastern edge of the Qinghai-Tibet Plateau, triggering numerous landslide geological disasters. The earthquake caused a significant landslide at Ganjiazhai, with an estimated volume of about 5 million m^3 (Fu et al., 2020). Additionally, it triggered a large landslide at Wangjiapo, with a volume of 1.2 million m^3 (Luo et al., 2020), as illustrated in **Figure 1 (a)**, and a massive landslide at Hongshiyan, with a volume of up to 12.24 million m^3 (Luo et al., 2019), as illustrated in **Figure 1 (b)**. It is highly unusual for a Mw 6.5 moderate earthquake to induce such large-scale landslide disasters, emphasizing the particularly severe dynamic response of slopes to near-fault ground motion, leading to more significant damage. Consequently, there is an urgent need to study the dynamic response characteristics of slopes under near-fault ground motion. In general, near-fault ground motions, occurring within 20 km of a fault, can have significant impacts,

particularly for PLGM generated by earthquakes with magnitudes exceeding 6.5. These events often result in more extensive damage over a broader area. For instance, the 1999 Chi-Chi earthquake in Taiwan (Mw 7.6), the Loma Prieta earthquake (Mw 6.9), the Northridge earthquake (Mw 6.9), and the Hector Mine earthquake (Mw 7.1) all produced strong ground motions with magnitudes above 6.5. As a result, their effects typically extended beyond a 20 km radius and influenced even larger regions (Chen et al., 2019). These earthquakes are particularly dangerous due to velocity pulse effects and forward directivity effects (Zhang et al., 2024). The velocity pulse effect is characterized by short-duration, high-energy pulses in the ground motion velocity time history, causing significant structural impacts, displacements, and deformations (Zeng et al., 2024). The forward directivity effect can be explained by the Doppler effect.

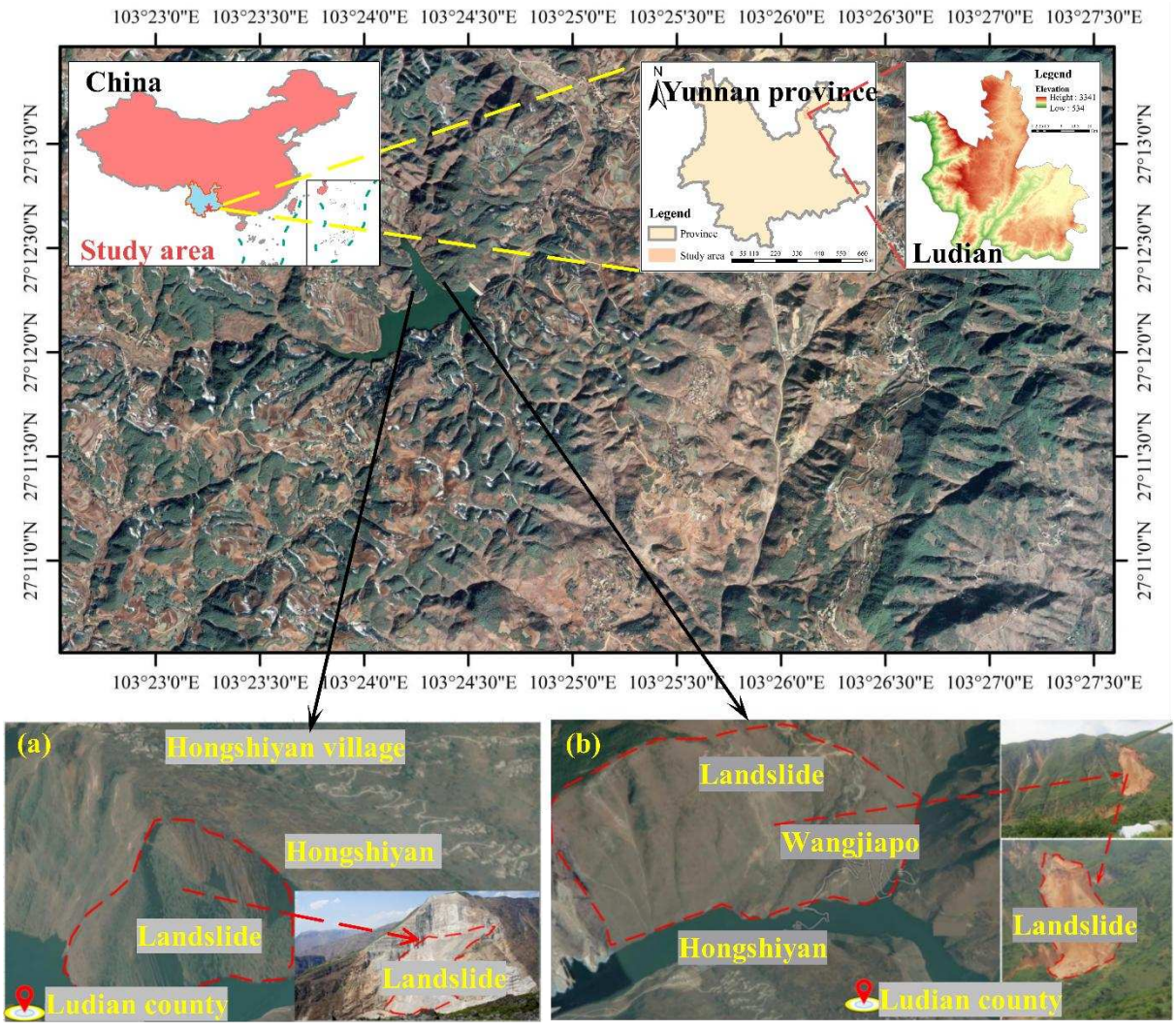

Figure 1 Typical landslide hazards triggered by the Ludian earthquake: (a) Hongshiyan giant landslide; (b) Wangjiapo landslide.

Based on the direction of fault rupture and the site location, the effects of seismic waves can be classified as

forward directivity and backward directivity, as illustrated in **Figure 2**. When the rupture propagation velocity of the fault plane approaches the shear wave velocity and the rupture moves toward the observation station, most of the fault plane's energy arrives at the station nearly simultaneously. The accumulation of energy over a short period creates PLGM, resulting in a prominent pulse at the start of the station record, known as the forward directivity effect (Li et al., 2024). PLGM can transmit substantial seismic energy to the structure within a short period, significantly enhancing its dynamic response.

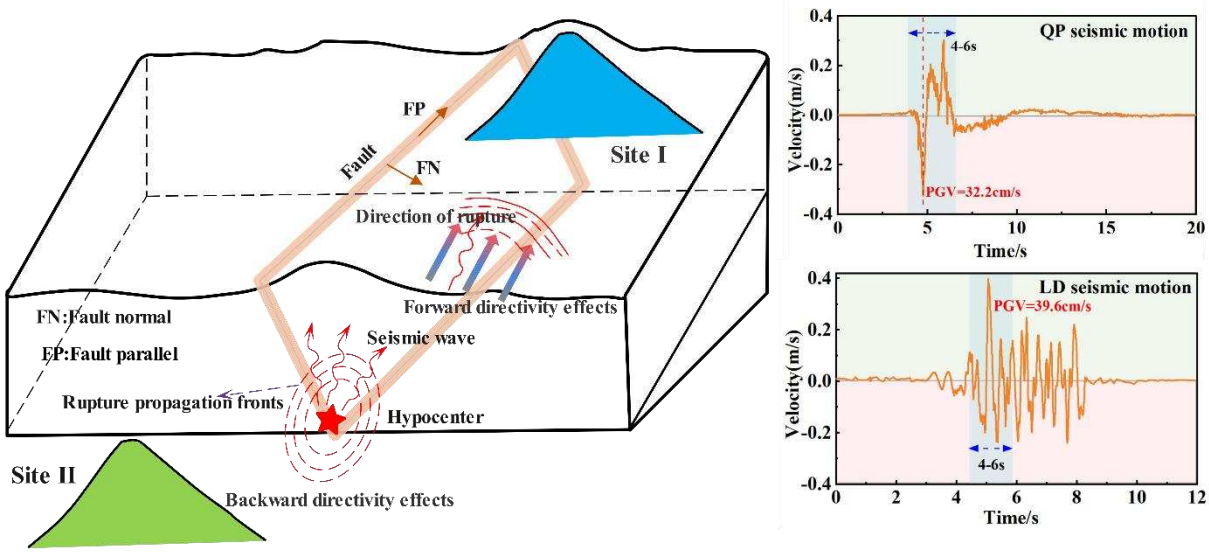

Figure 2 The rupture directivity effect.

Currently, three primary methods are employed to analyze the dynamic response of slopes under strong near-fault ground motions: field investigations (on-site monitoring), shaking table model tests, and numerical simulations (Zhou et al., 2022; Pai et al., 2011). However, on-site monitoring alone often lacks the comprehensive insight required to fully understand the dynamic behavior of actual slopes during earthquakes (Song et al., 2021). The shaking table tests are regarded as one of the most effective methods for studying rock slopes (Xin et al., 2022). This method allows for precise control of model size, input seismic motions, and boundary conditions to mirror actual conditions closely and provides an intuitive reflection of the dynamic response characteristics and damage instability process of slopes under seismic excitations (Xin et al., 2019). For instance, Xin et al. (2024a) employed large-scale shaking table tests to clarify the seismic failure mechanism of a bedding parallel stepped rock slope, focusing on acceleration, displacement, and earth pressure responses, along with shattering failure phenomena. In another study, Xin et al. (2024b) investigated the dynamic interactions and failure mechanisms within the tunnel-slope system. They evaluated the effectiveness of the frame-anchor support method by analyzing the acceleration responses of the slope and the peak strain of the tunnel, and assessing damage to both the slope

and the tunnel using damage identification techniques based on the Marginal Hilbert Spectrum (MHS) obtained through the Hilbert-Huang transform. Similarly, Bao et al. (2023) investigated the influence of ground motion intensity and pulse characteristics on the dynamic response of slopes under near-fault conditions, conducting analyses in both time and frequency domains. Wei et al. (2024) used shaking table tests to examine the effects of near-fault pulses on the seismic responses and pile-soil interactions in a soil-cable-stayed-bridge system model, while Bao et al. (2021) compared the dynamic responses of slopes subjected to PLGM versus non-pulse-like ground motion (NPLGM). In another study, Fan et al. (2016) explored the dynamic response differences between bedding slopes and anti-dip slopes. Wang et al. (2024) also established two slope models, bedding rock and debris slopes, and investigated their dynamic response characteristics and instability mechanisms using shaking table tests. Compared to NPLGMs, PLGMs exhibit significantly stronger seismic effects, with studies indicating that PLGMs induce approximately 7% greater seismic responses, thereby increasing slope instability risks (Antwi, Buah et al., 2024). Song et al. (2013) demonstrated that waves containing velocity pulses significantly amplify PGA, particularly in middle and upper slope sections, due to increased horizontal inertial forces. Furthermore, Li et al. (2024) established a direct correlation between high-energy velocity pulses and landslide initiation, emphasizing their critical role in slope instability mechanisms. Quantitative analyses using the Newmark method by Gao et al. (2014) revealed that near-fault velocity pulse ground motions induce larger sliding displacements and stronger destructive forces. Similarly, Song et al. (2014) found that slope slip characteristics are closely linked to velocity pulse properties, with slippage typically occurring early in seismic activity and exhibiting higher velocity and energy, thereby amplifying destructive impacts. In summary, while previous research has demonstrated that PLGMs significantly influence energy release patterns-particularly due to the distinct characteristics of the velocity pulse segments-and induce stronger dynamic responses compared to NPLGMs, the underlying mechanisms driving these phenomena remain to be further explored. Additionally, a more comprehensive investigation is needed required to quantify the differences in seismic dynamic responses between PLGMs and NPLGMs.

Numerical methods can be also used as effective means to analyze the seismic performance and failure mechanisms of slopes (Li et al., 2018). Commonly used approaches employed to address practical problems in earthquake engineering include continuum-based methods such as finite element method, finite difference method, and boundary element method, as well as discontinuous medium approaches like discrete element method, particle method, and meshless method (Lin et al., 2018). For instance, Yang et al. (2012) applied discrete element method to investigate the dynamic response and failure modes of slopes with weak interlayers subjected to near-fault ground

motions. Similarly, Song et al. (2024) used FLAC finite difference software (Itasca, 2014) to examine the dynamic response of slopes under near-fault ground motion, taking into account factors such as forward directivity effect, slip effect, and the presence or absence of velocity pulses. Li et al. (2018) conducted studies using UDEC discrete element numerical simulations to examine the failure process of anti-dip rock slopes with varying joint spacing and inclination under seismic loading. In another relevant study, Ning et al. (2024) investigated the dynamic behavior, failure evolution, and failure plane location of three typical toppling slopes in a basin under seismic waves using universal distinct element code (UDEC) simulations (Itasca, 2014). However, few studies have employed the UDEC discrete element method to explore the dynamic response characteristics and instability mechanisms of rock slopes under near-fault ground motion. Additionally, very limited research has compared the instability characteristics and failure processes of slopes subjected to PLGM versus NPLGM.

Current research has yet to fully investigate the dynamic response and failure mechanisms of rock slopes under near-fault PLGM, despite their substantial impact on slope stability. Specifically, the fundamental mechanisms responsible for the enhanced dynamic responses induced by PLGMs, as opposed to NPLGMs, are not yet fully understood. Furthermore, quantitative analyses are still lacking regarding how velocity pulse segments contribute to the amplification of dynamic responses in PLGMs and their correlation with seismic energy release. To address this research gap, this study proposes the RSER as a quantitative indicator to reveal the mechanisms behind dynamic response variations. The RSER serves two purposes: distinguishing between PLGM and NPLGM, and analyzing response differences among various PLGMs. Furthermore, the AIAF is introduced to quantify the positive correlation between RSER values and amplification effects, showing that higher RSER values lead to proportionally greater AIAF magnitudes. Additionally, wavelet packet transform further clarifies the relationship between ground motion energy release and velocity pulses, improving interpretation of shaking table tests and dynamic UDEC numerical results. It begins by outlining the instrumentation, the shaking table test setup, and the development of the numerical model. The study then presents a detailed analysis of the differences in slope dynamic responses under PLGM versus NPLGM, examining the shaking table test results through time-domain, frequency-domain, and time-frequency domain analyses. These findings are compared with the results from UDEC simulation. The study establishes a solid foundation for designing of earthquake-resistant slopes in seismically active areas.

2 Prototype case

The prototype of the shaking table tests is based on a cut slope along the Sanbao–Qingshui Expressway, located

between Qujing City and Kunming City. This area lies in the northern part of the Yiliang Basin, within the collapsed section of the Xiaojiang fault zone, an active fault zone from the Holocene epoch, as illustrated in **Figure 3 (a)**. The fault zone is an NNE-trending Holocene active fault, exhibiting overall characteristics of high-angle, left-lateral strike-slip faults that dip primarily toward the northwest or west, with a width of approximately 20 km. Due to the strong seismic activity in this region, the cut slope of the expressway is particularly vulnerable to the effects of PLGM generated by the fault. Furthermore, the study area is located within the seismically active Sichuan-Yunnan block, a high-risk tectonic region. Data from the National Scientific Seismic Data Center show that between 2010 and 2023, Yunnan Province experienced over 30 earthquakes with magnitudes ≥5.0. These events caused substantial economic losses, casualties, and severe geological hazards, highlighting the region's ongoing seismic activity. A significant event was the Mw 6.5 Ludian earthquake in August 2014, which occurred at the southeastern edge of the Tibetan Plateau, within the tectonic boundary between the Sichuan-Yunnan rhombic block and the South China block. The Ludian region, located at the intersection of the Xiaojiang and Zhaotong-Ludian fault zones, experiences strong tectonic activity and frequent earthquakes (Tang et al., 2020). The earthquake triggered numerous landslides, notable for their large numbers, concentrated distribution, and extensive coverage. Significant landslides included the Ganjiazhai landslide (5 million m^3), the Wangjiapo landslide (1.2 million m^3), and the Hongshiyan mega-landslide (12.24 million m^3) (Fu et al., 2020; Luo et al., 2019; Luo et al., 2020). Additionally, according to the Seismic Ground Motion Parameter Zonation Map of China (GB18305-2015), the seismic fortification intensity is rated as Grade VIII, which corresponds to considerable damage to ordinary buildings, including partial collapse. Field drilling and sampling results indicate that the slope predominantly consists of siltstone and sandstone, characterized by laminated bedding structures. The rock mass exhibits well-developed joints and fractures, with a loose structure and low cementation, making it particularly vulnerable to seismic impacts. The strata display a monocline structure, with the rock layers an orientation of 138º and a dip angle of 35º. The joint spacing ranging from 20 to 25 cm. These joints are unfilled and extend approximately 10 to 20 cm. According to geological survey results and the Code for Geological Investigation of Water Conservancy and Hydropower Engineering (GB 50487-2022), the cut slope is classified as a bedding parallel rock slope (Xin et al., 2024a), where the orientation of the rock layer adversely affects slope stability. Under strong external forces, such as high intensity earthquakes, the slope becomes highly prone to instability. To mitigate this risk, the slope has been excavated in three stepped levels, with excavation slopes of 1:1. The lowest slope of the last level is 1:1.25, as illustrated in **Figure 3 (b)**.

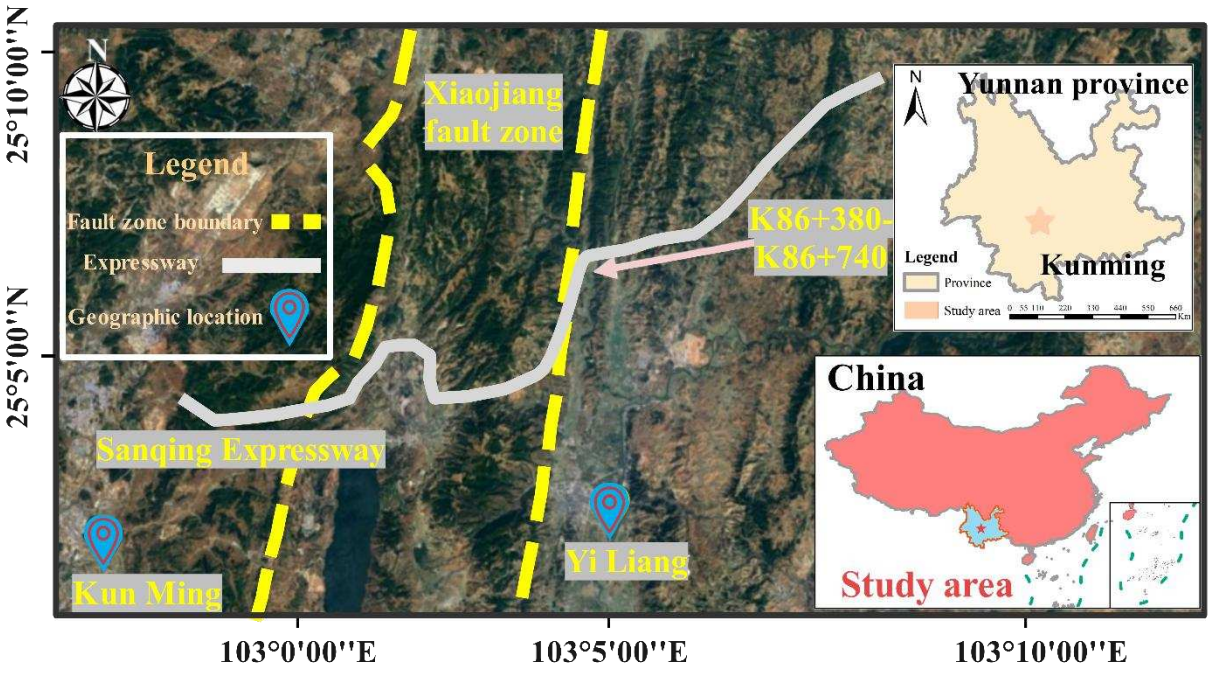

(a)

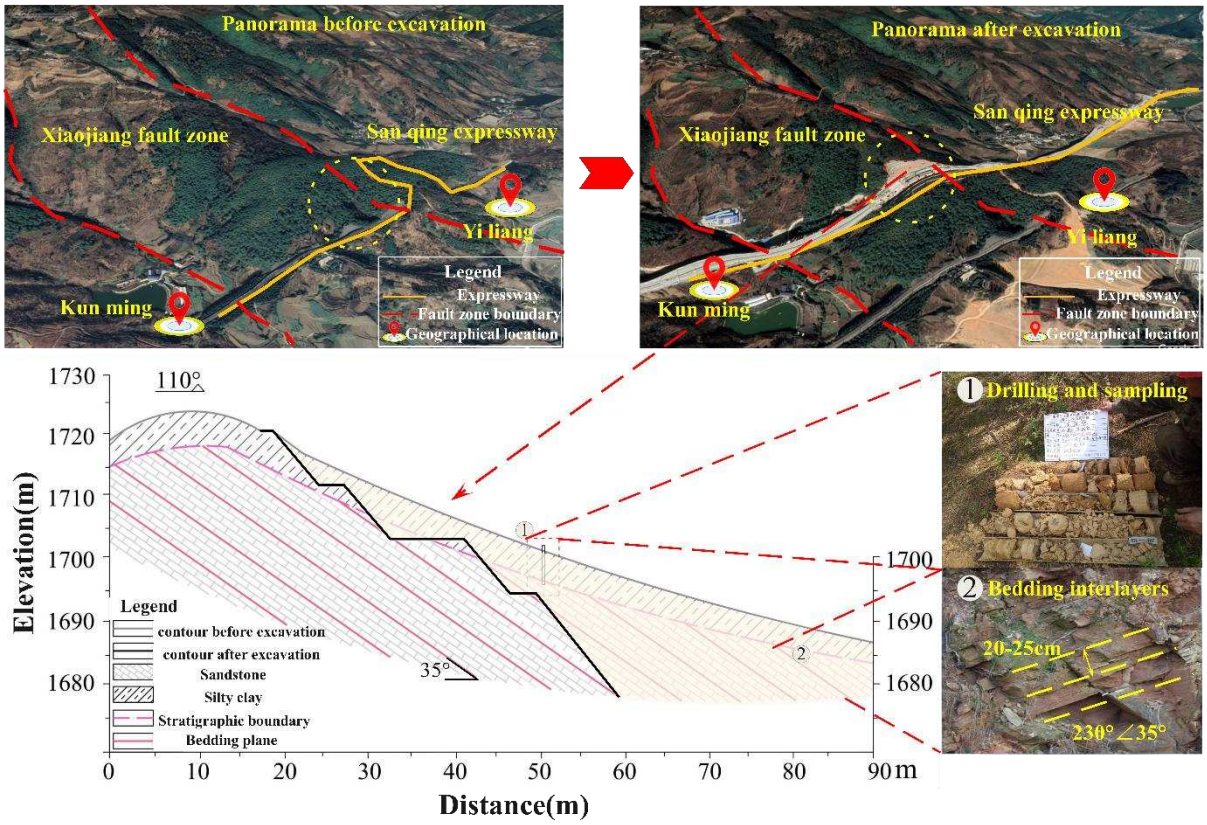

(b)

Figure 3. The topographical characteristics and geological section of the study area: (a) The topographical characteristics; (b) The geological section of the road cut slope engineering.

To determine the physical and mechanical parameters of the rock mass and its structural surfaces, extensive geotechnical and structural tests were conducted, including laboratory direct shear tests and in-situ shear tests,

as shown in **Figure 4**. Standard samples were prepared, and in-situ shear tests were performed under normal stress conditions of 0.5 MPa, 1.0 MPa, 1.5 MPa, and 2.0 MPa. These tests aimed to evaluate shear strength parameters, including cohesion and internal friction angle, under varying stress conditions, as illustrated in **Figure 4 (a)** and **(b)**. Additionally, to accurately assess the physical and mechanical properties of the model slope rock-soil mass, laboratory direct shear tests and uniaxial compressive strength tests were conducted on the prepared standard specimens, as shown in **Figure 4 (c)-(e)**. The stress-strain curves and test results are detailed in **Figure 4 (f)** and **(g)**. The resulting physical and mechanical properties of both the prototype and model materials used for the slopes are presented in **Table 1**.

(a)

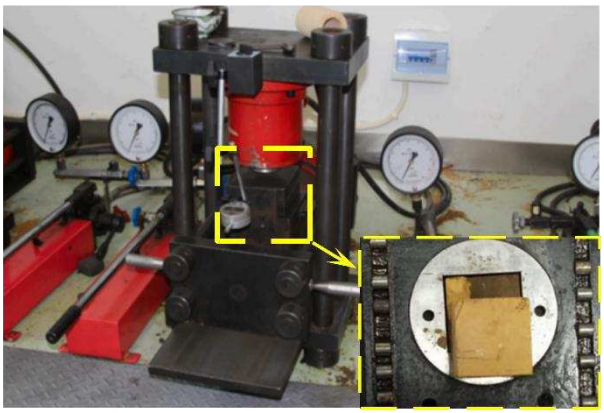

(b)

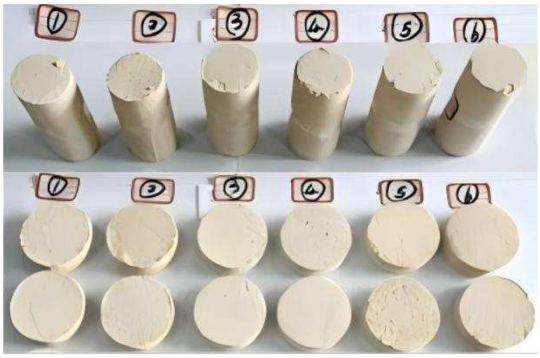

(c)

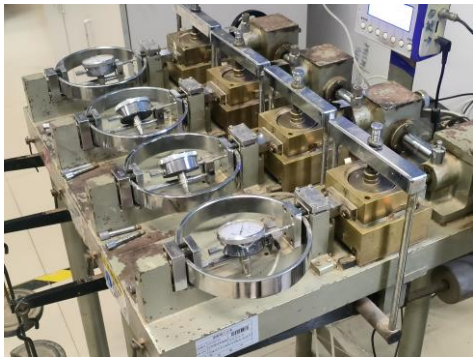

(d)

(e)

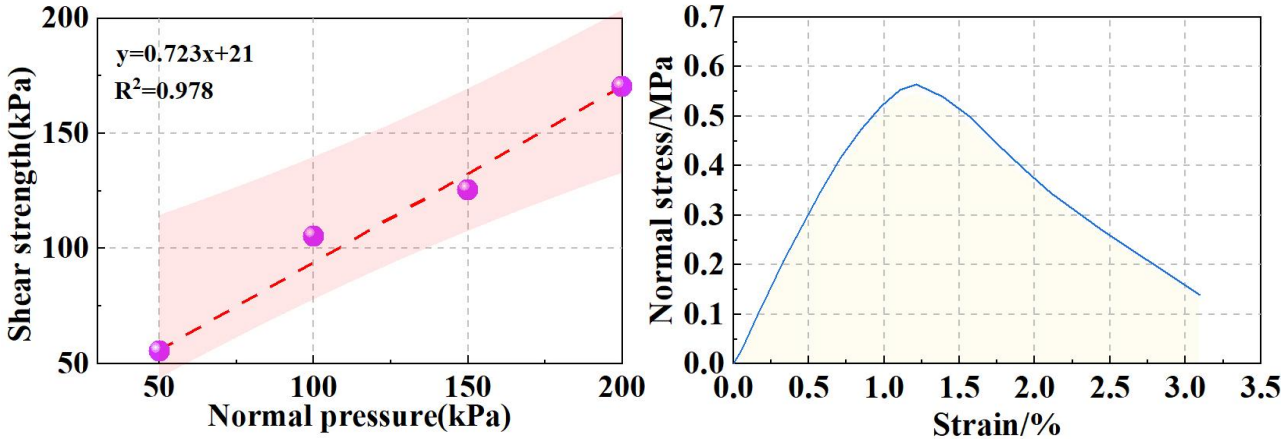

(f) (g)

Figure 4 The determination of the physical and mechanical properties of both the prototype and model materials used for the slopes: (a) drilling core diagram; (b) in-situ shear tests; (c) specimens for physico-mechanical tests; (d) direct shear test; (e) uniaxial compression test; (f) shear stress-normal stress fitting curve for the direct shear test; (g) stress-strain curves under uniaxial compression.

Table 1 The physical mechanical parameters of prototype materials and model materials

Parameters	Density ρ(kg/m^3)	Elastic modulus E(MPa)	Cohesion force c(kPa)	Internal friction angle φ(°)	Poisson's ratio (μ)
Prototype rock mass	2250	780	493	36	0.32
Model rock mass	2200	50	20	36	0.34
Prototype structural surfaces	1950	94	77	25	0.36
Model structural surfaces	1950	3.42	3	23	0.36

3 Methodology

3.1 Shaking table system

To explore the dynamic response characteristics and failure mechanisms of slopes under near-fault PLGM, comprehensive large-scale shaking table tests were conducted. The experiments were conducted in the Seismic Simulation Shaking Table Laboratory at the State Key Laboratory of Geohazard Prevention and Geoenvironmental Protection, Chengdu University of Technology, as illustrated in **Figure 5**. The shaking table system comprises several key components, including the shaking table, a computer control center, a hydraulic power supply, an accumulator, servo valves, actuators, and a multi-channel data acquisition system. The

shaking table is designed to securely hold and mount test specimens. Input waveforms are transmitted as signal commands from the control center to the servo valves, which convert electrical signals into analog signals. By regulating hydraulic flow, the actuators control the platform's motion, effectively simulating seismic waveforms. The system is equipped with a multi-channel, real-time data acquisition system to monitor and record the dynamic response of the slope model during the experiments. This setup enables real-time data recording and preliminary analysis, providing essential support for subsequent research and data processing.

The shaking table platform measures 4 meters in width and 6 meters in length and is supported by eight hydraulic actuators that enable six degrees of freedom motion along the X, Y, and Z axes. Specifically, four horizontal actuators and four vertical actuators support the platform. Motion along the X and Y axes is controlled by two actuators each, while motion along the Z axis is controlled by four actuators. The arrangement of the actuators and the six degrees of freedom motion capabilities are depicted in **Figure 5**. The system utilizes a Pulsar digital control system, capable of generating various types of excitation waves, including periodic waves, random waves, and real seismic waves. The actuators can achieve maximum horizontal and vertical accelerations of 15 m/s^2 and 10 m/s^2, respectively, with corresponding maximum displacements of 300 mm (horizontal) and 150 mm (vertical).

Additionally, a large, rigid model container was used to house the slope model, measuring 2.2 m × 0.7 m × 1.2 m (length × width × height). The container was securely attached to the shaking table with high-strength bolts, and the slope model was placed inside the rigid container.

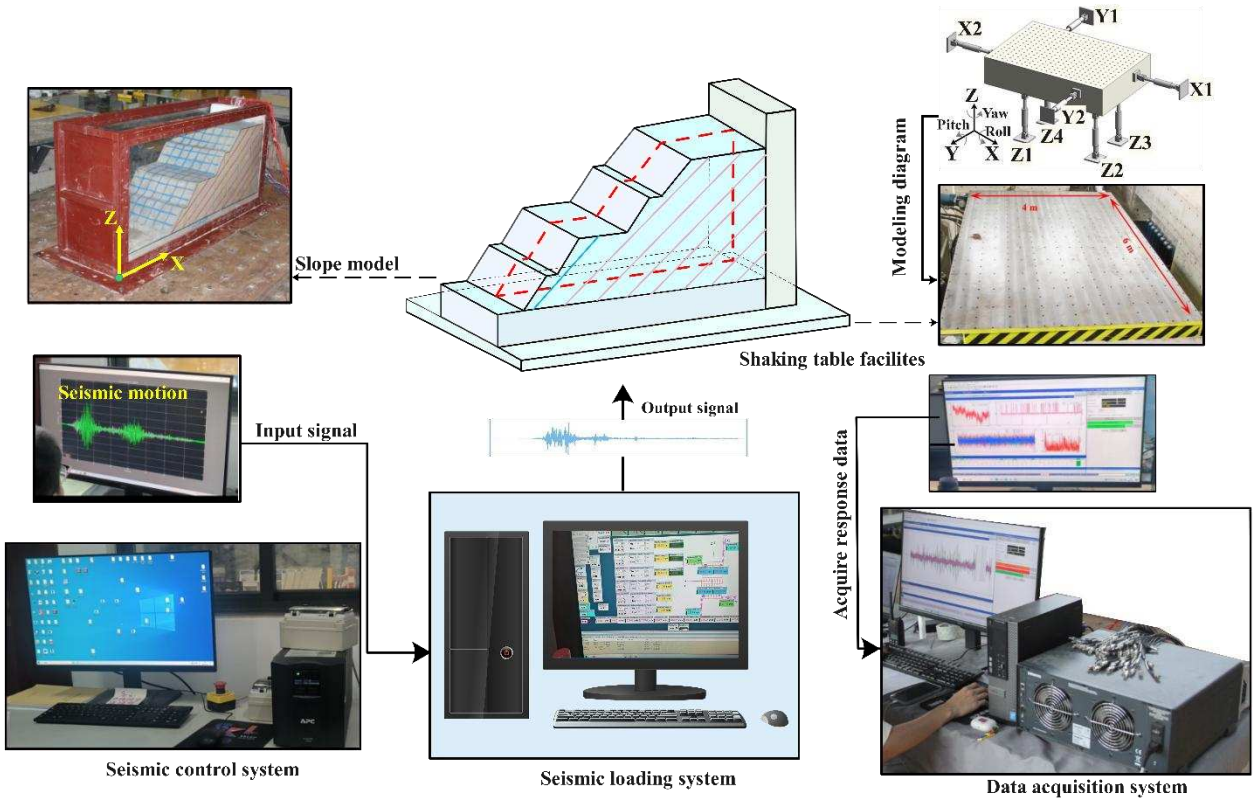

Figure 5 Shaking table facilities.

3.2 Similarity relationships and model fabrication

In this study, the cut slope between sections K86+380 and K86+740 of the Yunnan-Kunming Expressway was used as the prototype slope. In existing shaking table test research, scaled model testing has been extensively employed by researchers owing to physical constraints in testing equipment dimensions and load-bearing capacities (Shi et al., 2023; Yang et al., 2023; Xin et al., 2024a; Xin et al., 2024c; Fan et al., 2016). Consequently, the real dynamic response characteristics of this slope were simulated using a scaled model test incorporating geometric, kinematic, and dynamic similarity principles. To accurately replicate the prototype's dynamic behavior in the shaking table tests, similitude relations were applied. These relations ensure appropriate scaling of key parameters including geometric dimensions [L], time [T], mass [M], as well as boundary and initial conditions. Based on the Buckingham-π theorem and dimensional analysis, physical quantities must satisfy constraint equations derived from base quantities. These equations establish a rigorous similarity relationship system between the scaled model and the prototype slope, ensuring the scaled model closely represents the full-scale prototype's behavior (Miao et al., 2024; Wei et al., 2024). By adopting a geometric scaling ratio of 1:25 and carefully controlling other key similarity parameters (including displacement, velocity, acceleration, frequency, and stress), the scaled model ensures close alignment with the

prototype in dynamic response characteristics, enabling accurate representation of the prototype's key dynamic behaviors and providing reliable simulations of structural responses under dynamic loading conditions. Previous research has demonstrated that scaled models can effectively replicate the dynamic response of practical engineering structures when primary similarity criteria are satisfied (Yang et al., 2023; Yang et al., 2025a; Shi et al., 2023). In this study, a total of 13 parameters were considered, and these parameters satisfy the physical function described by **Equation (1)**. [*M*], [*L*], and [*T*] are regarded as fundamental dimensions, and based on dimensional consistency, each parameter can be represented by **Equation (2)** and **Equation (3)**. Furthermore, the similarity criterion function can be expressed as **Equation (4)**, where π_i represents the dimensionless similarity criterion. Consequently, the general similarity criterion can be written as **Equation (5)**. The similarity criterion and the similarity ratios of all 13 parameters can be determined using the matrix method (Fan et al., 2016, Pai at al., 2023), as listed in **Table 2**.

$$f\left(l,\rho,a,E,\mu,c,\varphi,\sigma,\varepsilon,t,d,v,\zeta\right)=0 \tag{1}$$

$$F(\pi_1,\pi_2,\ldots\pi_{10}) \tag{2}$$

$$M^0L^0T^0 = L^{a_1}\cdot(ML^{-3})^{a_2}\cdot(LT^{-2})^{a_3}\cdot(ML^{-1}T^{-2})^{a_4}\cdot(1)^{a_5}\cdot(ML^{-1}T^{-2})^{a_6}\cdot(1)^{a_7}\cdot(ML^{-1}T^{-2})^{a_8}\cdot(1)^{a_9}\cdot(T)^{a_{10}}\cdot(L)^{a_{11}}\cdot(LT^{-1})^{a_{12}}\cdot(1)^{a_{13}} \tag{3}$$

$$\left.\begin{aligned} &a_1-3a_2-2a_3-a_4-a_6-a_8+a_{11}+a_{12}=0\\ &-2a_3-2a_4-2a_6-2a_8+a_{10}-a_{12}=0\\ &a_2+a_4+a_6+a_8=0\\ &a_5+a_7+a_9+a_{13}=cons\tan t \end{aligned}\right\} \tag{4}$$

$$\pi_i=[l]^{a_1}\cdot[\rho]^{a_2}\cdot[a]^{a_3}\cdot[E]^{a_4}\cdot[\mu]^{a_5}\cdot[c]^{a_6}\cdot[\varphi]^{a_7}\cdot[\sigma]^{a_8}\cdot[\varepsilon]^{a_9}\cdot[t]^{a_{10}}\cdot[d]^{a_{11}}\cdot[v]^{a_{12}}\cdot[\zeta]^{a_{13}} \tag{5}$$

Table 2 The similarity criterion based on the matrix method and similarity ratios.

	E a_4	μ a_5	c a_6	φ a_7	σ a_8	ε a_9	t a_{10}	d a_{11}	v a_{12}	ξ a_{13}	ι a_1	ρ a_3	a a_2	Equation	Similarity criterion	Similarity ratios
π_1	1	0	0	0	0	0	0	0	0	0	-1	-1	-1	$\pi_1=E/(l\rho a)$	$C_E=C_lC_\rho C_a$	$C_E=25$
π_2		1	0	0	0	0	0	0	0	0	0	0	0	$\pi_2=\mu$	1	$C_\mu=1$
π_3			1	0	0	0	0	0	0	0	-1	-1	-1	$\pi_3=c/(l\rho a)$	$C_c=C_lC_\rho C_a$	$C_c=25$
π_4				1	0	0	0	0	0	0	0	0	0	$\pi_4=\varphi$	1	$C_\varphi=1$
π_5					1	0	0	0	0	0	-1	-1	-1	$\pi_5=\sigma/(l\rho a)$	$C_\sigma=C_lC_\rho C_a$	$C_\sigma=25$
π_6						1	0	0	0	0	0	0	0	$\pi_6=\varepsilon$	1	$C_\varepsilon=1$
π_7							1	0	0	0	-1/2	0	1/2	$\pi_7=t/(a/l)^{1/2}$	$C_t=C_l^{1/2}C_a^{-1/2}$	$C_t=5$
π_8								1	0	0	-1	0	0	$\pi_8=d/l$	$C_d=C_l$	$C_d=25$
π_9									1	0	-1/2	0	-1/2	$\pi_9=v/(al)^{1/2}$	$C_v=C_l^{1/2}C_a^{1/2}$	$C_v=5$
π_{10}										1	0	0	0	$\pi_{10}=\xi$	1	$C_\xi=1$

Additionally, orthogonal experimental results from previous shaking table tests on rock slopes with similar

material compositions were utilized (Song et al., 2021; Song et al., 2020; Xin et al., 2024a). The selected proportions of the similarity material used to replicate the prototype rock mass were 65:13:5: 13:3 for barite powder, bentonite, gypsum, paraffin oil, and water, respectively (see **Figure 6**).

In this study, 15 cm × 10 cm polyethylene film units were utilized to simulate structural surface in the bedding rock slope model, with their mechanical parameters derived from existing research (Xin et al., 2024c). The connectivity rate was calculated based on field observations of vertical spacing, rock internal friction angle, and average structural plane length, following **Equations (6)** and **(7)**

$$k_l = \frac{L_{cp}}{L_k + L_{cp}} \tag{6}$$

where, k_l represents the connectivity rate, L_{cp} represents the average length of a single structural surface, and L_k denotes the modified value derived from the average spacing of the structural surfaces in accordance with the rock failure criterion, calculated using the following equation:

$$L_k = \frac{a}{\sin(45° - \frac{\varphi}{2})} \tag{7}$$

The structural surfaces in the shaking table tests were assigned a 60% connectivity rate, consistent with the methodology employed in comparable experimental studies (Cui et al., 2024; Yang et al., 2023; Xin et al., 2024c; Wang et al.,2018).

During the fabrication of the slope model, the process was divided into three sequential parts (serial numbers 1-3). Step 1 (Serial Number 1): The model materials were prepared by mixing materials according to similarity material proportions for slope modeling. Step 2 (Serial Number 2): The preparation of similar materials for slope modeling was carried out. The similar materials were thoroughly mixed and sifted according to the specified similarity ratio to ensure precise preparation. At the same time, physical and mechanical property tests were conducted to verify the suitability of the materials for accurate slope modeling. Step 3 (Serial Number 3): The construction process of the slope model was carried out. To minimize boundary effects and ensure the model accurately simulates the seismic response, 10 cm thick polystyrene foam plates were placed on both the front and rear sides of the slope model. A 20 cm thick base was then fabricated and compacted to provide a stable foundation. The slope was gradually constructed using a layered compaction method, with each layer carefully smoothed to ensure uniformity. After each layer was completed, 15 × 10 cm polyethylene films were applied to simulate structural surfaces. Sensors were embedded at specified locations to monitor the dynamic response of the slope model in real time during the experiment. Once construction was completed, the surface

was smoothed with a wooden board, and reference points were marked to facilitate the subsequent analysis of the slope's shattered process. The detailed steps of the entire construction process are illustrated in **Figure 6**.

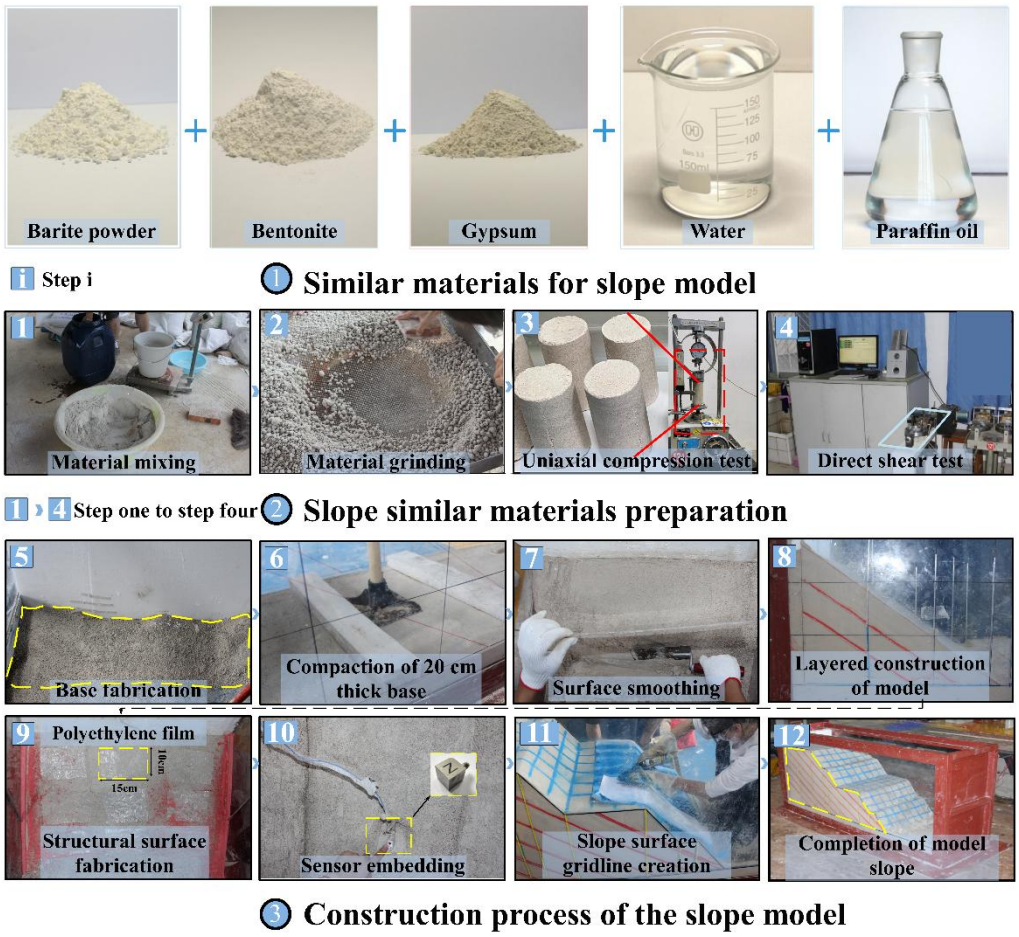

Figure 6 Manufacturing processes of rock slope model.

3.3 The scheme of tests and loading

This series of experiments aimed to investigate how rock slopes dynamically respond to various seismic excitations. Accelerometers were installed at various elevations within the model, as well as at the internal and external corners of the slope, to monitor the dynamic response. The monitoring cross-section of the slope model, which represents the central section of the slope, is marked with a red dashed line, as shown in **Figure 7(a)**. The accelerometer used are three-axis piezoelectric sensor with a sensitivity of 10 mV/m·s^{-2} and a frequency response range of 0.5 Hz to 2000.0 Hz. Each sensor measures 10 mm in length, width, and height. A reference accelerometer (A0) was fixed on the shaking table to monitor the input waveform. All sensors were set to a sampling frequency of 512 Hz. Additionally, the high-speed cameras with a resolution of 2048×1024 pixels were positioned on the side of the slope to capture and record the asymptotic damage evolution in real time.

The data acquisition system collected real-time acceleration data based on the input ground motion from the control system, allowing for detailed analysis of the dynamic response characteristics of the slope.

This study utilizes four representative ground motion recordings from destructive earthquakes in Southwest China, selected for their engineering seismology significance: the Wolong (WL), Ludian (LD), Menyuan (MY), and Qingping (QP) seismic motions (Cui et al., 2023; Wang et al., 2023; Zhang et al., 2016). Characterized by pronounced velocity pulse effects and broadband spectral components, these records have been extensively adopted as input motions in shaking table tests for slope dynamic response investigations (Yang et al., 2025a; Xin et al., 2024a; Xin et al., 2024c; Feng et al., 2025; Liu et al., 2024). Recent studies have demonstrated that employing 3-4 representative seismic motion meets the requirements for shaking table test investigations (Liu et al., 2024; Shi et al., 2024; Yang et al., 2025b). Accordingly, this study adopts these four records as seismic inputs for the investigation. To specifically investigate the effects of PLGM on rock slopes, three PLGM and one NPLGM were considered. The four seismic motions analyzed in this study were recorded at four distinct locations: Ludian, Qingping, Menyuan, and Wolong. Specifically, two of the recordings were obtained during separate earthquake events: (1) The LD record was obtained during the 2014 Ludian earthquake (Mw 6.5) at the Ludian Strong Motion Station (Station Code: 53LLT) in Zhaotong City, Yunnan Province. The estimated hypocentral distances for the event range between 10 to 15 km (Fu et al., 2020). (2) The MY record was captured during the 2022 Menyuan earthquake (Mw 6.9) at the Menyuan Integrated Seismic Station (Station Code: E63MHY) in Qinghai Province, with hypocentral distances of approximately 15 to 20 km (Wang et al., 2023). In contrast, the other two records represent near-field observations from the 2008 Wenchuan earthquake (Mw 8.0): (1) The QP seismic motion was recorded at the Mianzhu Qingping Station (Station Code: 51QP), with a hypocentral distance of 10–20 km. (2) The WL seismic motion was obtained at the Wolong Valley Station (Station Code: 51WL), with an estimated hypocentral distance of 30–40 km (Guo et al., 2015; Fan et al., 2018).The LD seismic motion was selected for its near-fault pulse characteristics, influenced by the Xiaojiang fault zone, while QP and MY seismic motions, which also display near-fault pulse characteristics, were used to examine the effects of different PLGM.

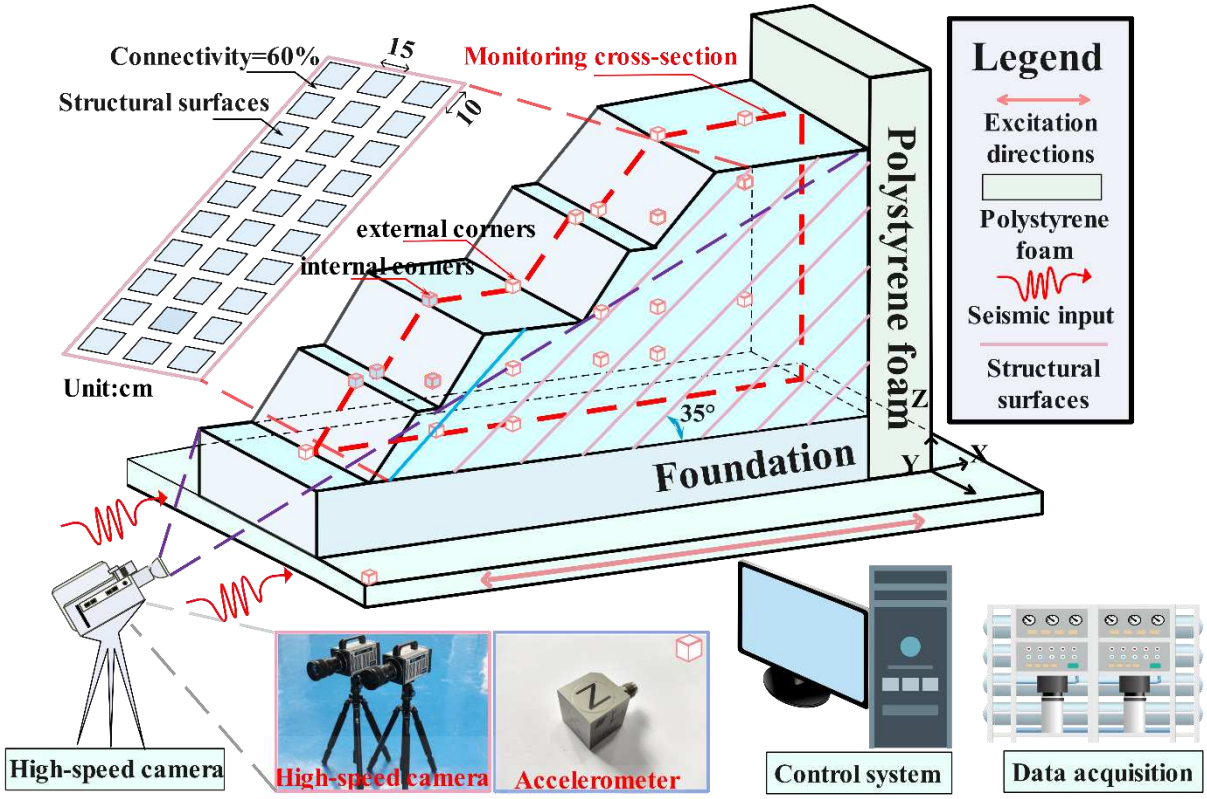

(a)

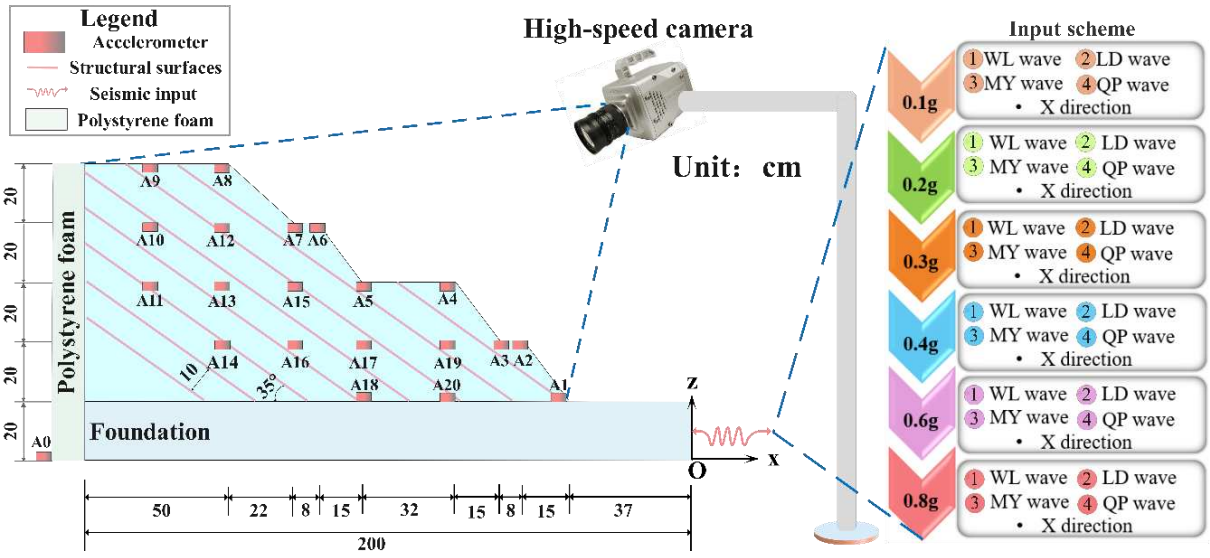

(b)

Figure 7 Conditions of test cases: (a) experimental setup; (b) monitoring plan and input scheme.

The WL seismic motion, in contrast to the other three, serves to differentiate between PLGM and NPLGM. The loading sequence starts with NPLGMs followed by transitions to PLGMs. The detailed input scheme is presented in **Figure 7 (b)**, with input acceleration peak values gradually increasing from 0.1 g to 0.8 g. Prior to each excitation, white noise (WN) was used to scan the slope model to assess changes in natural frequency and

damping ratio.

The acceleration time histories and Normalized Fast Fourier transform (NFFT) spectrum plots for the four different seismic motions are shown in **Figure 8**. Baseline correction and 0.5-50Hz band-pass filtering were applied using Seismosignal software (SeismoSoft, 2023). The results show that the frequency components of QP and MY seismic motions are relatively more complex, followed by LD and WL seismic motions. Similarly, the LD seismic motion, characterized as a shallow-focus earthquake with a relatively shallow focal depth, is heavily influenced by the Xiaojiang fault zones (Zhou et al., 2016). This seismic event exhibits distinct near-fault pulse characteristics, as evidenced by the velocity pulse segment in its velocity time-history curve. The seismic motion is primarily governed by low-frequency components in the range of 0.5 to 3 Hz, with a concentrated spectral composition, classifying it as a narrow-band seismic motion. In contrast, the MY seismic motion, another shallow-focus earthquake, concentrates seismic energy predominantly in the north-south direction (Cheng et al., 2024). Its frequency components largely fall within the mid-to-high-frequency range (1-5 Hz), displaying a relatively rich frequency spectrum, which classifies it as a broad-band seismic motion. The QP seismic motion, which is also a shallow-focus earthquake, exhibits a pronounced site amplification effect near the epicenter. Its ground motion frequencies cover a wide range, from 0.5 to 20 Hz, placing it firmly within the broad-band category. This broad frequency spectrum leads to a more complex dynamic response compared to other seismic motions. On the other hand, the WL seismic motion, associated with a deep-focus earthquake at an epicentral depth of approximately 25 km, exhibits significant attenuation, particularly in the high-frequency range (Li et al., 2008; Fan et al., 2018). The motion is primarily governed by low-frequency components ranging from 0 to 3 Hz, with a concentrated spectral distribution, classifying it as a narrow-band seismic motion. When compared to the WL seismic motion, the LD seismic motion exhibits a slightly broader frequency range. From a frequency-domain perspective, the broader frequency content of the QP and MY seismic motions indicates a higher potential for inducing stronger dynamic responses in slopes. Although the LD seismic motion shows less frequency complexity, it still exerts a significant impact. In contrast, the WL seismic motion generates the weakest dynamic response among the four types analyzed.

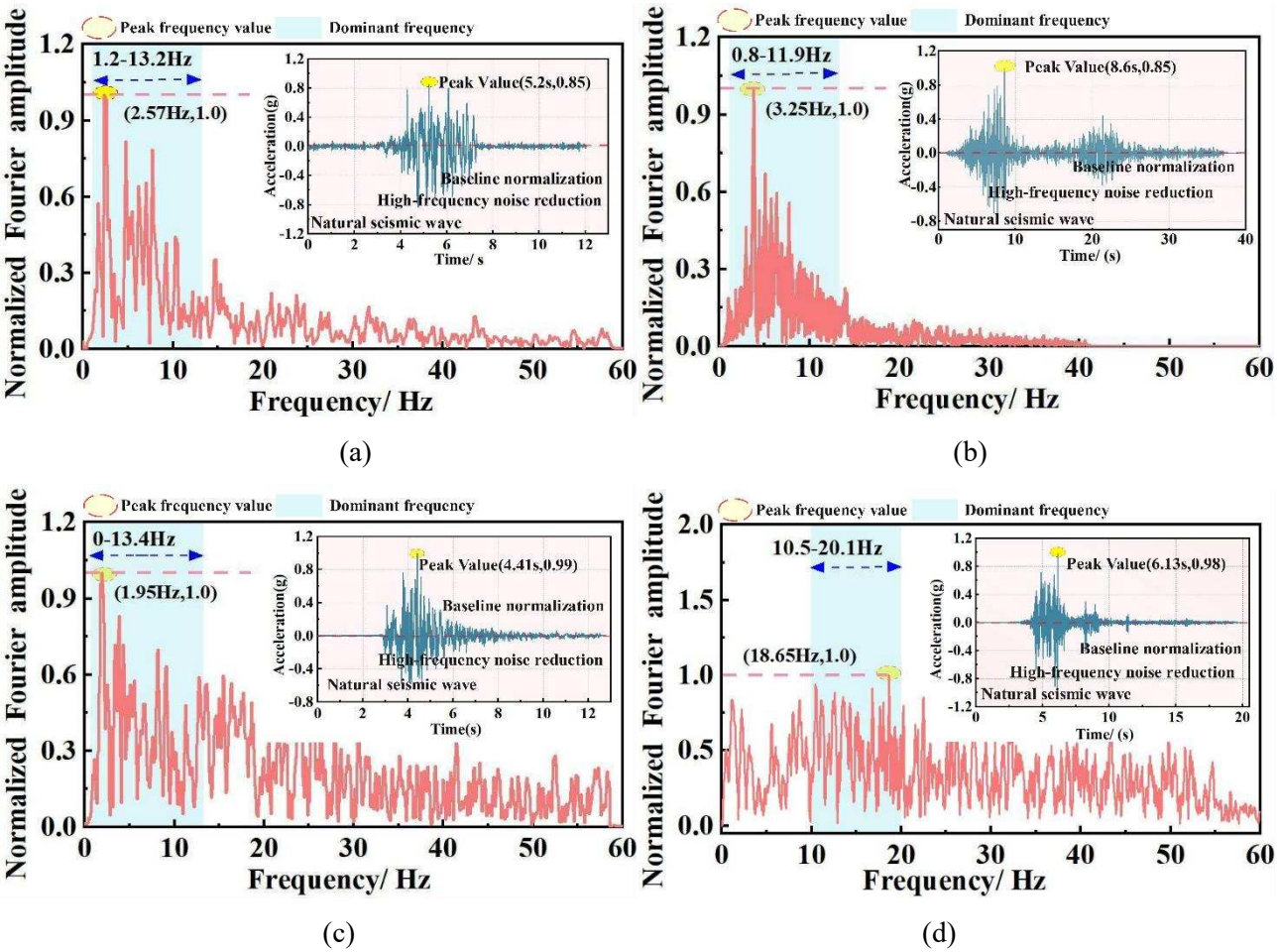

Figure 8 The time history curves and Fourier spectra of the input waveforms: (a) LD seismic motion; (b) WL seismic motion; (c) MY seismic motion; (d) QP seismic motion.

3.4 Identification of pulse-like seismic ground motion

A wide range of quantitative methods have emerged for identifying PLGM, each demonstrating good accuracy within specific research contexts. However, due to the inherent limitations of individual methods, they often produce inconsistent results for certain ground motion records, posing it challenging to establish a reliable classification criterion based solely on a single identification approach. To address this issue, Peng and Han (2024) adopted a multifaceted strategy for identifying pulse-like records. Instead of focusing on improving a single time-frequency analysis-based identification method, they conducted a systematic review to select seven baseline methods. The near-fault ground motion database used by their research reveals significant discrepancies in the identification reliability of the seven baseline methods. Based on the consistency of their determinations, ground motions are classified into four categories:

Category A: 6–7 methods identify the motion as pulse-like;

Category B: 4–5 methods identify the motion as pulse-like;

Category C: 2–3 methods identify the motion as pulse-like;

Category D: 0-1 methods identify the motion as pulse-like.

Analysis indicates that if a method classifies too many ground motions as pulse-like in Category D, it may be considered unreliable. To address this issue, this study employs the Analytic Hierarchy Process (AHP) to determine the weight ratios of the seven baseline methods. AHP is a structured decision-making technique that decomposes complex judgments into pairwise comparisons, synthesizes the results, and derives priority rankings to support optimal decision-making. By leveraging AHP, a comprehensive categorization method was developed to integrate the strengths of each approach, resulting in a more robust and credible classification criterion. The specific steps for applying AHP to assign weights to the baseline methods are as follows:

(1) For each method, based on the classification data and pre-categorized results, quantify the number of pulse-like ground motions and their distribution across Categories A–D. Similarly, determine the count and distribution of non-pulse-like ground motions among the same four categories.

(2) Based on the results obtained from Step (1), design scoring guidelines to score each method.

(3.) Using the scores of each method, apply the AHP to determine the weight ratio of each method.

If a method categorizes a significant number of ground motions as pulse-like but assigns them to Category D, this indicates a tendency for false positive identification (misclassifying non-pulse motions as pulse-like). Conversely, if a method classifies numerous motions as non-pulse-like yet distributes them in Categories A or B, this reveals a false negative tendency. To quantitatively evaluate each method's reliability, establishing the following scoring framework in Step (2): For classified pulse-like ground motions, assign 1 point if placed in Category A, 0.5 points if placed in Category B, 0 points if placed in Category C, and -1 point if placed in Category D. For classified non-pulse-like ground motions, assign -1 point if placed in Category A, -0.5 points if placed in Category B, 0 points if placed in Category C, and 1 point if placed in Category D. To calculate the composite score for each method, sum the scores from the aforementioned two scoring categories to obtain the raw score. The total raw score is computed as $NA+0.5NB+ND$, where NA, NB and ND denote the respective counts of ground motions classified into Categories A, B and D. Each method's scaled score is then derived by dividing its raw score by the total raw score and multiplying by the standardized maximum score of 100 points. In Step (3), Saaty's 1–9 scale method is used to evaluate the relative importance of each pair of methods (Saaty et al., 1983). Specifically, the values from 1 to 9 represent levels of importance from the equally important to the extremely more important.

For instance, if the scaled score difference between two methods falls within the range of 0 to 3, it is assigned

a scale value of 1, indicating equal importance. As the score difference increases, the assigned scale value increases accordingly, reflecting greater importance. Finally, the weight ratio of each method is calculated based on the final importance result of each method. This comprehensive categorization method is fully established, with the category indicator (CI) and the weight ratio for each method calculated using **Equations (8)** to **(12)**:

$$A'_{ij} = \frac{A_{ij}}{\sum_{i=1}^{n} A_{ij}} \tag{8}$$

$$S_i = \sum_{j=1}^{n} A'_{ij} \tag{9}$$

$$w_k = \frac{S_i}{\sum_{i=1}^{n} S_i} \tag{10}$$

$$\mathbf{w} = [0.066, 0.018, 0.279, 0.050, 0.178, 0.284, 0.125]^{\mathrm{T}} \tag{11}$$

$$CI = \alpha \cdot w \tag{12}$$

where, A is the original scale matrix, A_{ij} denotes the element in the i-th row and j-th column of A, and $\sum_{i=1}^{n} A_{ij}$ is the sum of the j-th column, A'_{ij} represents the normalized matrix, S is the vector of row sums, $\sum_{i=1}^{n} S_i$ is the total sum of all row sums, $\boldsymbol{w}_k$ is the normalized weight ratio for the k-th, and $\boldsymbol{w}$ is the weight ratio of each method, a 7×1 vector. All the weight ratios in the vector add up to 1, while α is a 1×7 vector containing only -1 or 1 to indicate the classification result using the selected seven baseline methods. It is marked 1 if a ground motion record is classified as pulse-like by a baseline method, and -1 if classified as non-pulse-like; therefore $-1 \leq CI \leq 1$. For example, **Table 3** shows the classification results of QP seismic motion, using the selected seven baseline methods. If a ground motion record is classified as pulse-like by all baseline methods except for Method 2, then $\alpha = [1, -1, 1, 1, 1, 1, 1]$.

According to this new categorization system, ground motions are classified into four categories: Category A comprises definitively PLGM; Category B includes apparently PLGM; Category C consists of probably PLGM; and Category D covers ground motions unlikely to exhibit pulse-like characteristics. In general the following four categories are defined: (i) Category A: $CI \geq 0.8$, which are classified as pulse-like by 6-7 methods; (ii) Category B: $0 \leq CI < 0.8$, which are classified as pulse-like by 4-5 methods; (iii) Category C: $-0.8 \leq CI < 0$, which are classified as pulse-like by 2-3 methods; and (iv) Category D: $CI < -0.8$, which are classified as pulse-like by 0-1 method. Method 1-7 are the WT, HHT, ITD, PPV, PP, SVHC, DLVTH based methods, respectively (Baker at al., 2007; Chen et al., 2019; Geng and Pu, (2023); Hayden et al., 2024; Panella et al.,2017; Zhai et al., 2013; Zhai et al., 2018). **Figure 9** illustrates the flowchart of the proposed categorization method.

Table 3 Classification results of QP seismic motion using the selected seven baseline methods.

Method	Key parameters	Criterion for classification	Identification results
M 1	PI=3.66, $t_{17\%,orgin}$ =4.75s, $t_{5\%,pulse}$=4.66s	PI＞0, $t_{17\%,orgin}$>$t_{5\%,pulse}$	pulse-like
M 2	ρ_2=0.12, $\Delta E_{c2,max}$ =0.45	ρ_i>0.12, $\Delta E_{ci,max}$>0.32	no-pulse-like
M 3	PI=0.88	PI≥0.65	pulse-like
M 4	PPV=62.2cm/s, Score=1.0	PPV≥25cm/s, Score≥0.6	pulse-like
M 5	PGV=32.2cm/s, E_p=0.35	PGV≥30cm/s, E_p>0.3	pulse-like
M 6	E_k=0.48, Number of SVHC=2	E_k≥0.42, Number of SVHC=2	pulse-like
M 7	IP_R=0.98, PGV=32.2cm/s	IP_R≥0.7, PGV≥30cm/s	pulse-like

M1: Wavelet transform (WT) method; M2: Hilbert-Huang Transform (HHT) method; M3: Intrinsic time-scale decomposition technique (ITD) method; M4: Peak-to-peak velocity (PPV) method; M5: Pulse period (PP) method; M6: Significant velocity half-cycles. (SVHC) method; M7: Development length of velocity time history (DLVTH) method.

(M1)PI: Pulse indicator, t_{xorgin}: attains x% of the total of the original signal, $t_{x\%,pulse}$: attains x% of the extracted pulse; (M2) ρ_i:PGV(c_i)/PGA(c_i), c(i) is the ith IMF ranked form high frequency to low frequency; $\Delta E_{ci,max}$:=Max[REc_i-REc_{i-1}], the REc_i =E_{cn}/E_{tot}, E_{cn} is the cumulative energy, starting from the high-frequency component to the low-frequency component, E_{tot} is the integral of the squared velocity time history from 0 to the total duration. (M3) PI: Pulse-like, indicator; (M4) PPV: The difference of the peak velocity, Score: A score criterion; (M5) PGV: Peak ground velocity, E_p: $E(p)=\int_{ts}^{te} dE(t)=E(t_e)-E(t_s)$, $E(t)=\frac{\int_0^t V^2(\tau)d\tau}{\int_0^\infty V^2(\tau)d\tau}$, where $V(\tau)$ is the velocity time history of original ground motion record, t_s and t_e represent the pulse-starting and pulse-ending points, respectively. PI(M6) E_k: ratio of the energy of the k-th half-cycle to the total energy in the velocity time history of ground motion., Number of SVHC: the criterion for classification according to energy ratio thresholds (M7) IP_R: $IP_R=\frac{1}{1+e^{5-0.45PGV+0.01LDV}}$, $LD_V=\sum_{i=1}^{n}(\sqrt{(\Delta t)^2+(\Delta V_i)^2})$ where Δt is the time lapse of the time history between two successive points, ΔV_i is the velocity increment, PGV: Peak ground velocity.

Using the velocity time history curves for the QP, MY, LD, and WL seismic motions (see **Figure 10)**, the AHP comprehensive categorization method was applied to determine four key ground motion parameters. This analysis was performed using Methods 1 to 7, in accordance with the prescribed classification criteria. The calculation results are presented in **Figures 11 (a)** and **(b)**. In these figures, colors shifting towards red signify a higher likelihood of being classified as PLGM, while colors shifting towards blue indicate a tendency towards NPLGM. For example, in the case of QP seismic motion, Method 1 predominantly shows red hues, indicating

that it is classified as PLGM, whereas Method 2 displays blue hues, suggesting it is categorized as NPLGM. Similarly, Methods 3 through 7 classify the QP motion as PLGM. Therefore, for α_{QP}, the value is [1, -1, 1, 1, 1, 1, 1]. Similarly, α_{MY}, α_{LD}, and α_{WL} are [1, 1, 1, -1, 1, -1, 1], [1, 1, 1, 1, 1, 1, -1, 1], and [-1, -1, -1, 1, -1, -1, -1], respectively. Substituting these into **Equation (5)** results in 0.982, 0.697, 0.538, and -0.95, respectively. As illustrated in **Figure 11 (c)**, QP seismic motion is classified as Category A, whereas MY and LD seismic motions are classified as Category B, and WL seismic motion falls into Category D. Consequently, QP, MY, and LD seismic motions are identified as PLGM, while WL seismic motion is categorized as NPLGM.

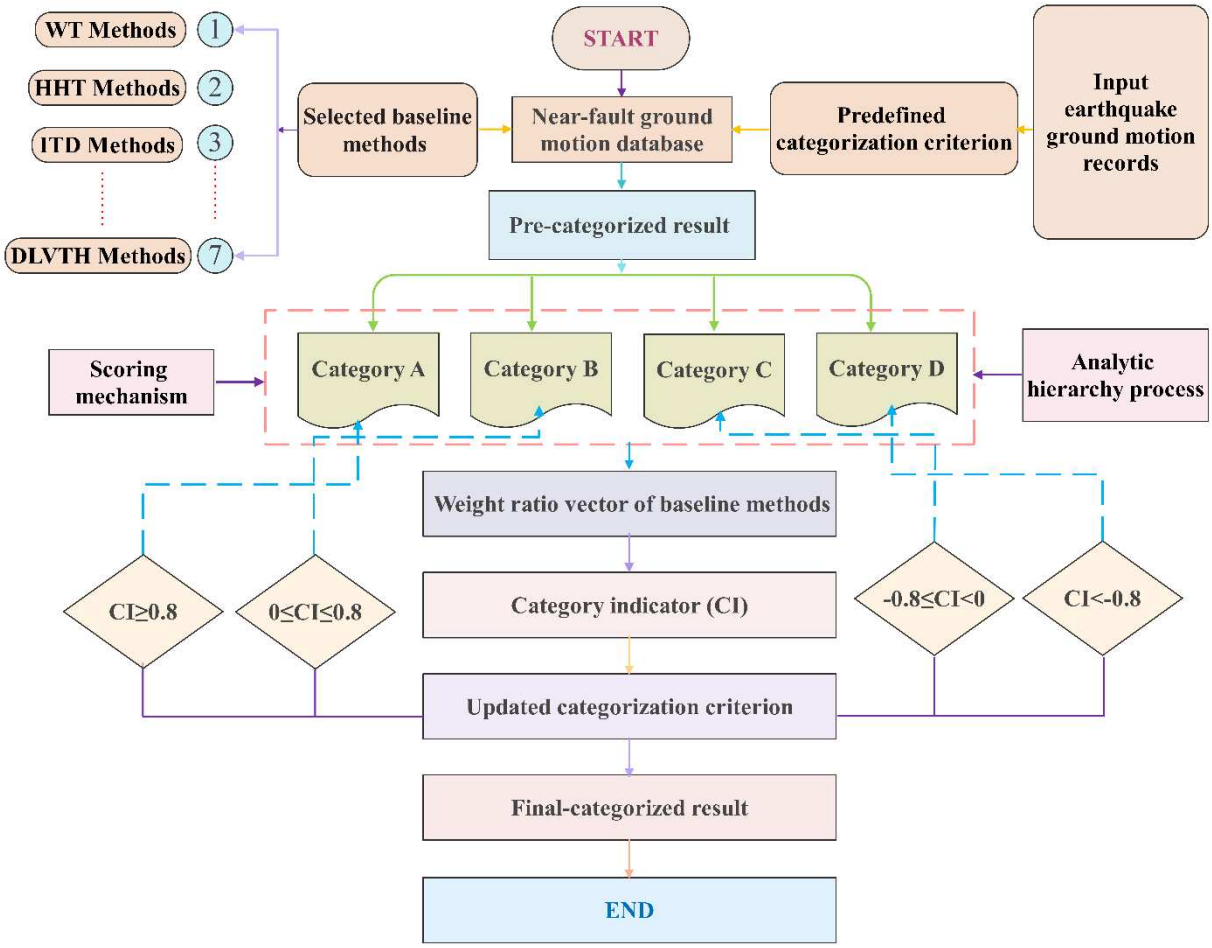

Figure 9 The flowchart of the proposed categorization method (Peng and Han, 2024).

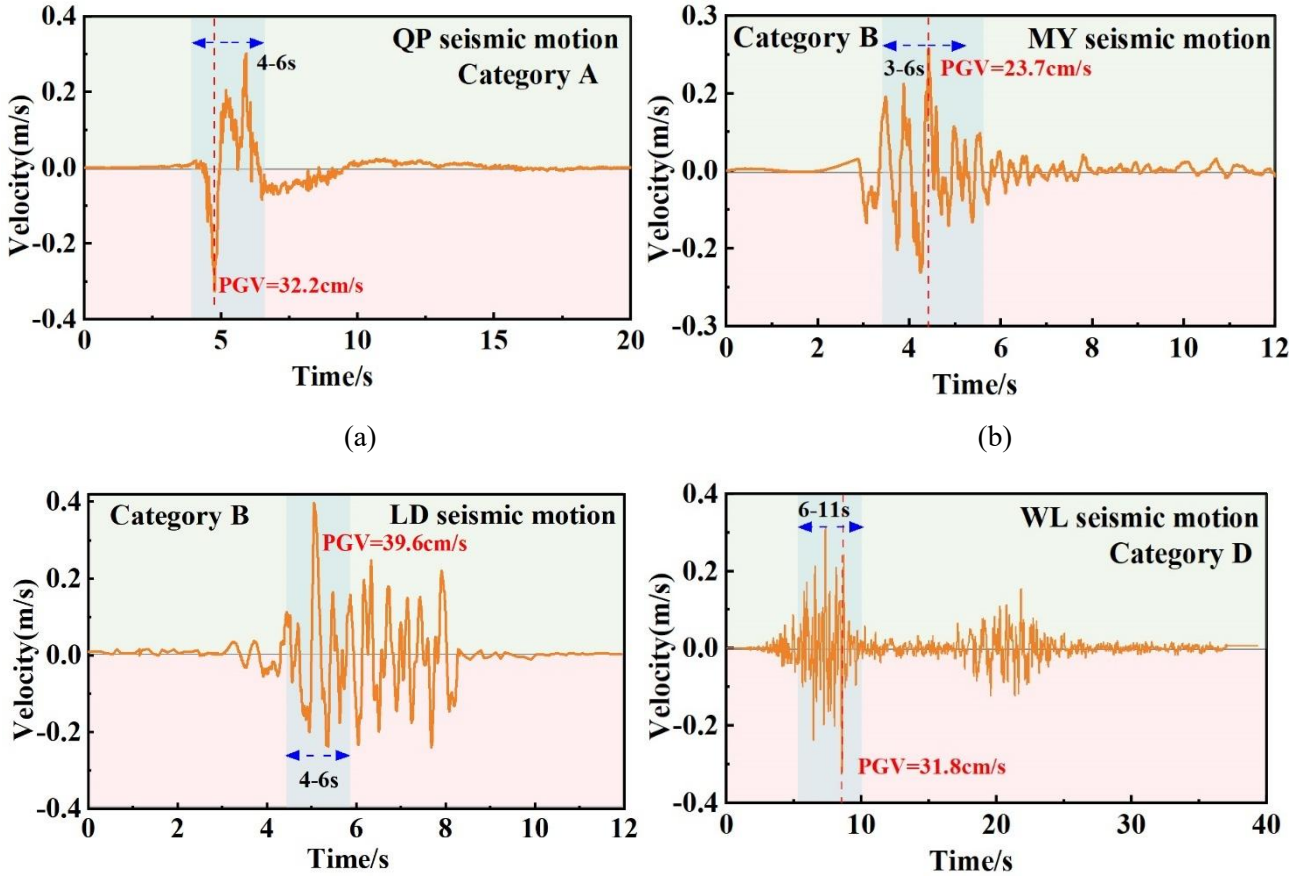

Figure 10 The velocity of time history of representative ground motions from the four categories: (a) QP seismic motion; (b) MY seismic motion; (c) LD seismic motion; (d) WL seismic motion.

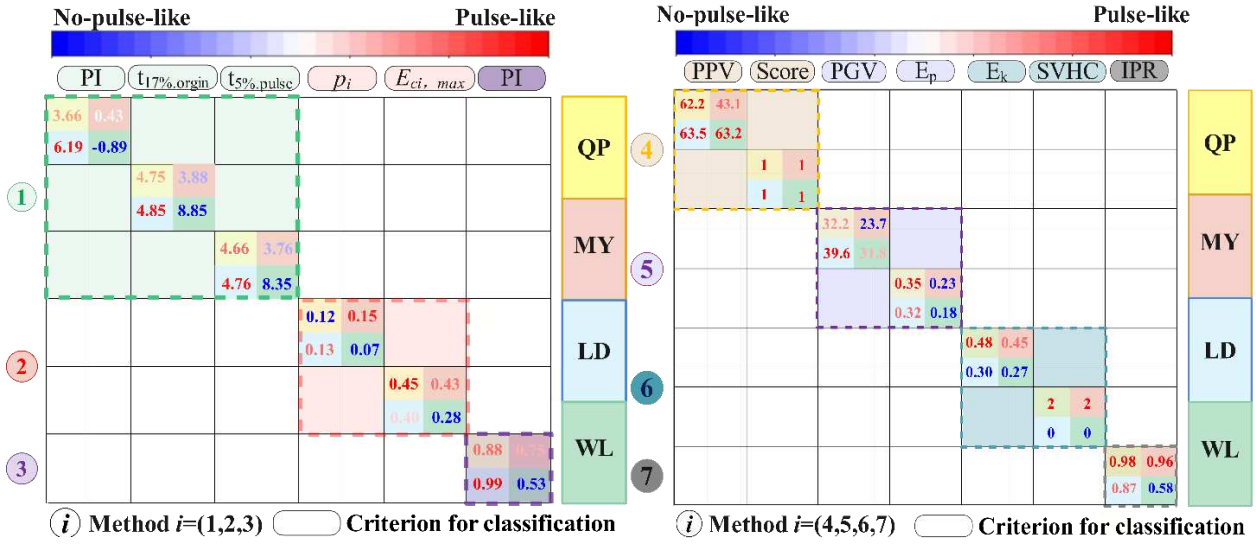

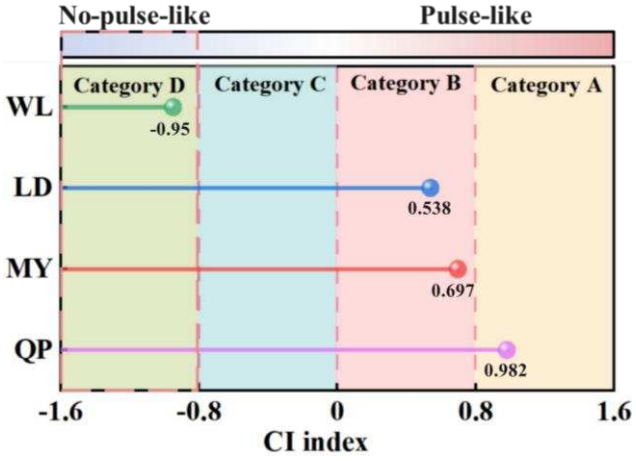

(c)

Figure 11 Velocity pulse identification reuslts: (a) Identification reuslts of method 1-3; (b) Identification reuslts of method 4-7; (c) Identification results based on the CI index.

4 Results and analysis

4.1 Acceleration response analysis

Different seismic motions, influenced by various source effects, can exhibit notable characteristic differences, such as the presence of velocity pulses and a broad spectrum of frequency domain components. These variations result in differing dynamic responses in slopes. In the time domain, acceleration serves as the key indicator of the magnitude of seismic inertial forces, with larger inertial forces generally leading to more intense dynamic responses in slopes. To quantitatively assess the differential dynamic responses of slopes under varying seismic motions, the acceleration amplification factor (AAF) is employed. The AAF is defined as the ratio of the peak acceleration at each measurement points to the peak value of the input signal, as shown in **Equation (13)**:

$$AAF = \frac{PGA_i}{PGA_o} \tag{13}$$

where, PGA_i represents the peak acceleration at various monitoring positions on the slope, and PGA_o represents the peak acceleration on the shaking table.

As shown in **Figures 12 (a)** and **(b)**, when the input acceleration peak value is 0.4 g, the AAF at both the external and internal corners of the slope increases with increasing elevation, reaching its maximum at the top of the slope. This indicates a clear acceleration amplification effect influenced by the elevation. Among the seismic motions, QP seismic motions shows the most pronounced amplification effect, followed by MY and LD seismic motions, with WL seismic motion showing the weakest effect. This result demonstrates that PLGMs produce significantly stronger amplification effects than NPLGMs. Notably, the AAF values at the internal

corners are higher than those at the external corners. This may be attributed to the different degree of freedom at these two types of corners. As illustrated in **Figures 12 (c)** and **(d)**, when the input acceleration peak value increases to 0.6 g, the AAF at both the external and internal corners of the slope decreases significantly. The QP seismic motion still demonstrates the strongest acceleration amplification effect, with AAF reductions of 21% at internal concerns and 30% at external concerns. The AAF for the MY seismic motion shows a slight decrease of 4.03%, 8.46%, 7.38%, and 5.29% at the external corners from A2 to A8, respectively, remaining relatively stable. In contrast, the AAF for the WL seismic motion increased by 3.03%, 5.42%, 14.07%, and 18.51% at the same external corners, while the LD seismic motion shows a smaller increase of 3.8%, 4.5%, 2.46%, and 2.8%. Both cases show a slight increasing trend. The stronger amplification effect of QP seismic motion can be attributed to its high-amplitude, short-duration seismic motion velocity pulse segment (SMVPS), which can introduce a substantial amount of energy into the slope in a very short period. This rapid energy input does not allow the slope sufficient time to recover elastically, causing a quick transition from the elastic phase to plastic failure. Under QP seismic motion, the increased amplitude intensifies seismic inertia forces, leading to cracking and the progressive expansion of secondary joints. These joints can obstruct the seismic wave propagation, partially blocking some of the seismic energy, which ultimately reduces the energy reaching the measurement points. Despite the reduced amplification effect of QP seismic motion, it remains stronger than the other three types of seismic motion. As illustrated in **Figures 12 (e)** and **(f)**, when the input acceleration peak value increased to 0.8g, a marginal rise in AAF is observed across all measurement points. Specifically, under the input of QP seismic motion, the AAF at A8 shows a modest increase of approximately 9.9%, while the AAF values at points A2, A4, and A6 increase by 6.05%, 12.60%, and 8.08%, respectively. This phenomenon indicates that the input ground motion energy is not fully transmitted to the measurement points, with energy losses primarily attributed to two factors: first, the attenuation of seismic waves due to reflection, refraction, and medium absorption during propagation; and second, the partial utilization of energy to induce slope instability (Shi et al., 2023). Based on the results of the analysis, it is evident that PLGM produce significantly stronger amplification effects and cause more damage compared to NPLGM.

Although both QP and MY seismic motions are classified as PLGM, their dynamic response characteristics show relative differences. Analyzing AAF alone does not effectively highlight the differences between their dynamic responses. To further quantify how different PLGMs affect the dynamic response of the slope, the difference in AAF (DAAF) is introduced. DAAF quantifies the amplification difference between QP and MY seismic motions, with DAAF defined as the difference between AAF_{QP} and AAF_{MY}. If DAAF is greater than 0,

546 it indicates that the amplification effect of QP seismic motion is stronger than that of MY seismic motion.
547 Conversely, if DAAF is less than 0, MY seismic motion has a stronger amplification effect than QP seismic
548 motion.

549

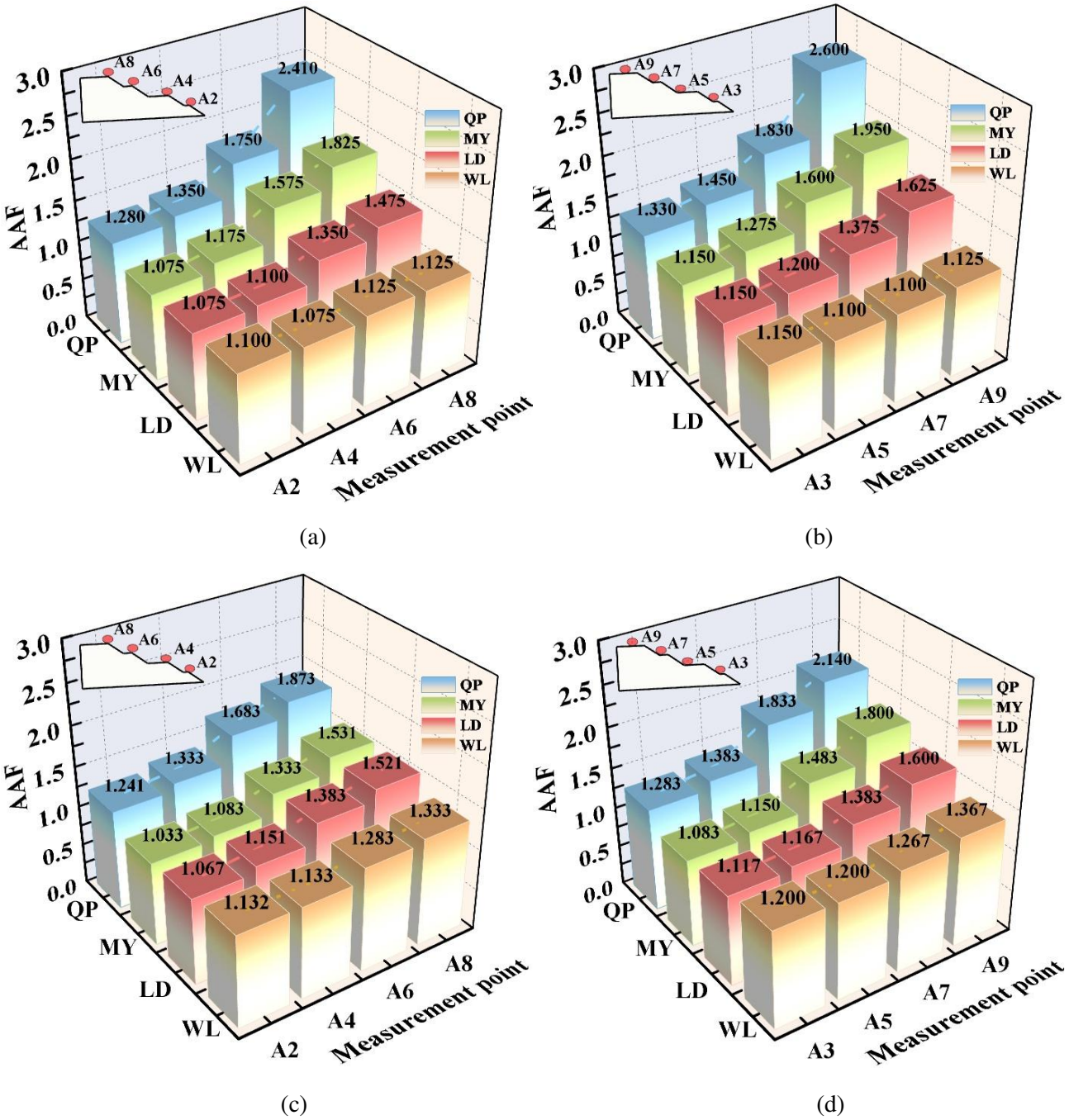

550

551

552

553

554

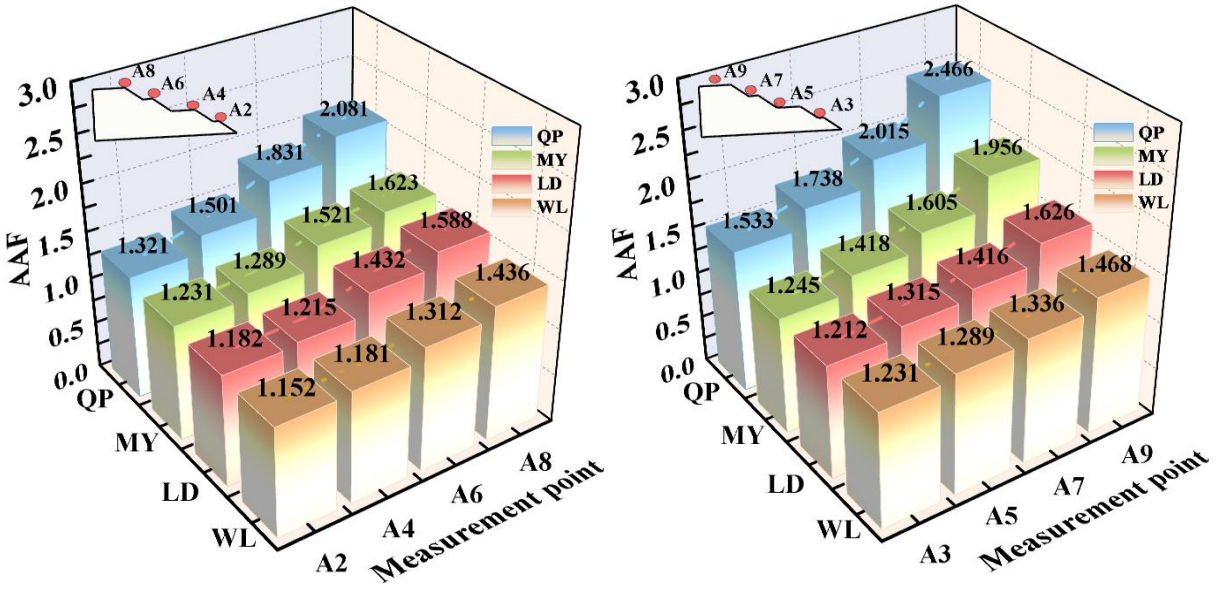

(e) (f)

Figure 12 The AAF values at the measurement points: (a) external corners of slope with 0.4 g input peak ground acceleration; (b) internal corners of slope with 0.4 g input peak ground acceleration; (c) external corners of slope with 0.6 g input peak ground acceleration; (d) internal corners of slope with 0.6 g input peak ground acceleration; (e) external corners of slope with 0.8 g input peak ground acceleration; (f) internal corners of slope with 0.8 g input peak ground acceleration.

The DAAF results shown in **Figure 13 (a)** reveal that at measurement points A2, A6, and A8, both AAF and DAAF increase sharply as relative elevation and peak ground acceleration (PGA) rise. However, the AAF increases nonlinearly with elevation, highlighting a pronounced “elevation amplification effect”, where energy amplification effect shows significant nonlinear characteristics with increasing elevation. Specifically, when PGA is 0.2 g, the DAAF values follow the order A6 > A8 > A2. As the PGA increases to 0.6 g, the DAAF at A8 becomes approximately equal to A6, and both are greater than A2. When PGA reaches 0.8 g, A8 surpasses A6. These observations indicate that as PGA increases, the DAAF at higher elevations rises progressively, highlighting significant variations in dynamic response due to the varying characteristics of PLGM. It is worth noting that the growth rate of DAAF at A8 and A2 is significantly greater than at A6, indicating that these points are more sensitive to PLGM excitation. This phenomenon may be due to the amplification of specific energy components as they reach the top of the slope. The mechanism behind this effect will be discussed in further detail in the following sections.

Under low amplitude PGA excitation, there is a significant difference in DAAF. However, as the peak acceleration increases, this difference diminishes. This behavior suggests that the velocity pulse characteristics

of PLGM introduce large amounts of energy into the slope. The repeated tensile and shear forces of the high-intensity ground motion cause numerous cracks within the slope, dividing the rock mass into loose blocks. This fragmentation enhances the isolation and damping effects of the slope, resulting in a decrease in DAAF as PGA increases. The variation of DAAF at the internal corners is generally similar to that observed at the external corners, as shown in **Figure 13 (b)**. However, it is noteworthy that the DAAF at A9 surpasses that at A8, indicating a more intense and sensitive dynamic response at the internal corners under PLGM with varying characteristics. This is due to the fact that the exteral corners are close to the free surface, resulting in a higher degree of freedom. Consequently, deformation is more likely to occur under seismic tension and shear, leading to weaker energy transfer effects compared to internal corners. As a result, both the AAF and DAAF are smaller at the external corners than at the interal corners.

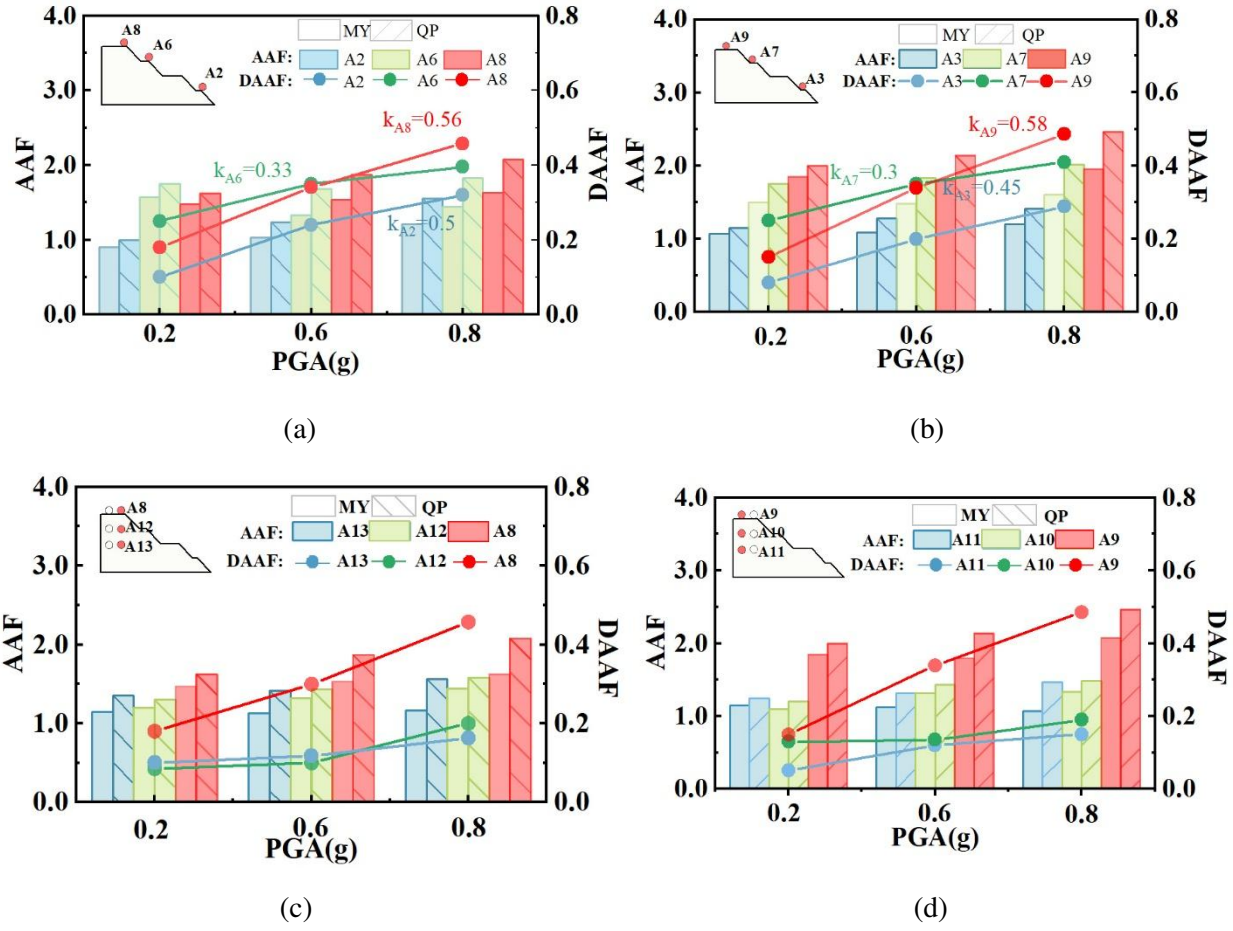

Figure 13 The AAF and DAAF measurements at various points along the slope under different peak accelerations: (a) external corners of slope; (b) internal corners of slope; (c) A13~A8; (d) A11~A9.

As shown in **Figure 13 (c)**, the DAAF results at measurement points A13, A12, and A8 reveal that DAAF increases sharply with rising both elevation and PGA. The energy amplification effect shows significant nonlinear characteristics with increasing elevation. By comparing the results for the internal and external corners, the following observations can be made:

Under the influence of two different types of PLGM, the difference in dynamic response at the top of the slope becomes more pronounced with increasing elevation. This indicates that higher elevations experience a stronger dynamic response and are more sensitive to PLGM, thereby increasing the risk of cracking at the top of the slope.

Under different PGA amplitudes, the overall DAAF values for A12 and A13 are significantly smaller than that for A8, indicating less variation in the dynamic response within the slope. As elevation increases, the difference in dynamic response at the top of the slope becomes more pronounced. This phenomenon can be explained by the stress state within the slope. Inside the slope, the overlying soil layer provides a more stable stress condition compared to the slope surface. When seismic waves act as external loads on the slope, the internal stress state remains relatively stable. In contrast, the top of the slope lacks the constraint of an overlying soil layer, and hence is more vulnerable to disturbances, resulting in a stronger dynamic response. This phenomenon, known as the “surface effect”, highlights the more pronounced differences in dynamic response at the top of the slope.

With increasing elevation, the DAAF results shown in **Figure 13 (d)** indicate that at A11, A10, and A9, the variation in DAAF near the trailing edge follows a similar pattern to that observed in **Figure 13 (c)**. Notably, the DAAF of A9, located at the top of slope, is larger than at A11 and A10, which are situated inside the slope. This suggests that the stress state becomes more stable closer to the interior of the slope, enhancing its resistance to seismic inertia forces. Consequently, the DAAF at the top of the slope (A9) is significantly greater than at A11 and A10.

Under the PLGM, the seismic disturbance is most pronounced at the top of the slope. Additionally, due to the elevation amplification effect of seismic waves, the dynamic response differences between QP and MY seismic motions are greatest at the top. Consequently, the DAAF values at the measuring points inside the slope are significantly smaller compared than those at the surface and the top of the slope. The degree of decrease in DAAF can be used to characterize the progressive damage in different parts of the slope as PGA increases.

4.2 FFT spectrum analysis

By applying the Fourier Transform, the acceleration signals in the time domain are converted into frequency

domain representations, showing the distribution of seismic energy at different frequencies. Examining the spectrum plots is crucial for identifying the primary frequency components of seismic motion and understanding their impact on the slope, which is essential for designing earthquake-resistant structures and assessing seismic risks. **Figure 14** shows the Fourier spectra of MY, LD, QP and WL seismic motions at the A8, with an input peak acceleration of 0.4 g. It is evident that, except for the WL seismic motion, the high-frequency components of the other three seismic motions are amplified to varying degrees, with QP seismic motion exhibiting the largest range of high-frequency amplification. This indicates that the amplification effect on high-frequency components of PLGM is stronger than for NPLGM. The order of amplification is as follows: QP seismic motion > MY seismic motion > LD seismic motion > WL seismic motion.

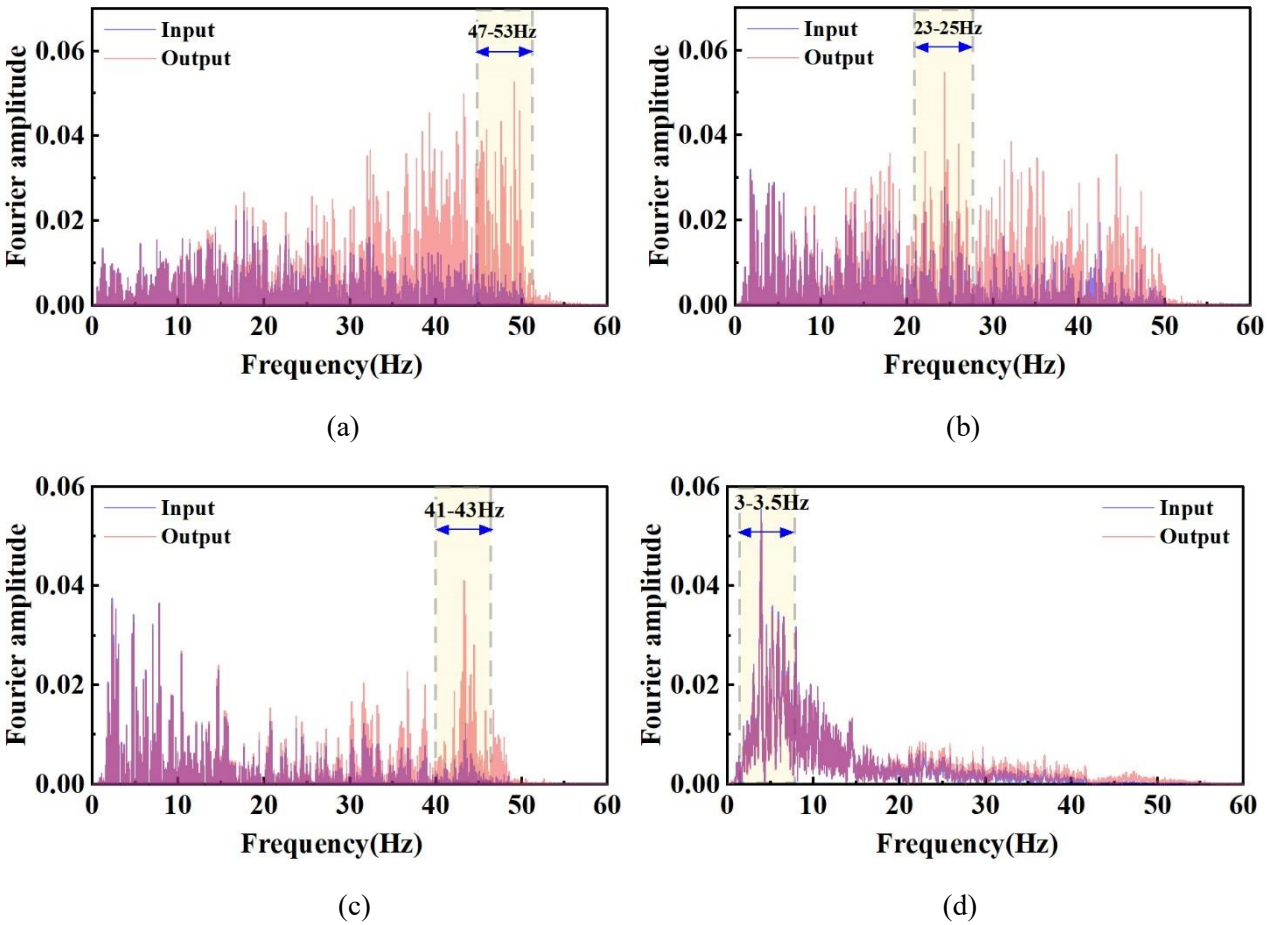

Figure 14 The spectrum for a peak acceleration of 0.4 g: (a) QP seismic motion; (b) MY seismic motion; (c) LD seismic motion; (d) WL seismic motion.

To better examine the variation patterns of the frequency spectrum at different measurement points on the slope under various seismic motions, the Peak Fourier Spectrum Amplitude (PFSA) is introduced. PFSA is defined as the ratio of the FFT peak value of the response waveform to that of the input waveform. As illustrated

in **Figures 15 (a)** and **(b)**, for LD and WL seismic motions from A2 to A8, the PFSA increases gradually. On the contrary, for QP and MY seismic motions, the PFSA increases slowly from A2 to A4, but from A6 to A8, the PFSA continues to increase with a larger growth rate. The growth rate for QP seismic motion is stronger than for MY seismic motion.

This indicates that under the effect of PLGM with different characteristics, higher elevations are more sensitive to seismic motions, resulting in a more intense dynamic response. This observation explains why the DAAF increases with elevation, as the difference in dynamic response becomes more pronounced at higher elevations, with PFSA amplification being greatest for QP seismic motion, followed by MY and LD seismic motions, and weakest for WL seismic motion. This phenomenon can be attributed to the concentrated energy of PLGM in the SMVPS. As the seismic motion ascends, the concentrated energy intensifies reflection and refraction effects at higher elevations. At the top of the slope, where terrain or geological conditions frequently undergo significant changes, seismic waves are more prone to pronounced refraction and reflection. This can result in significant amplification of seismic motion energy. Therefore, the PFSA values of PLGM at the top of the slope are typically higher than those of NPLGM.

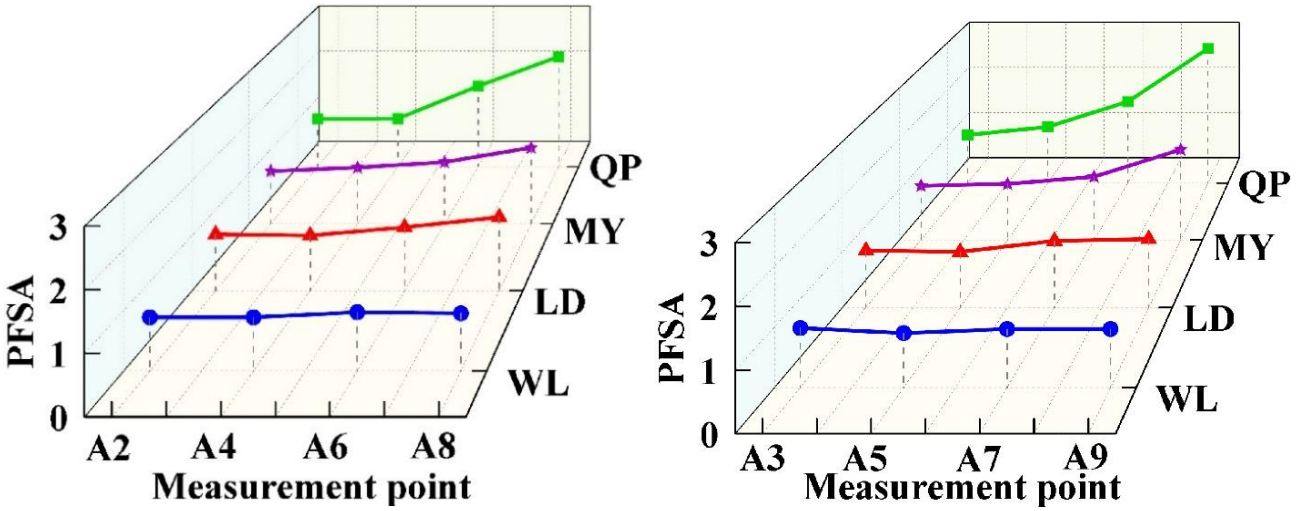

(a) (b)

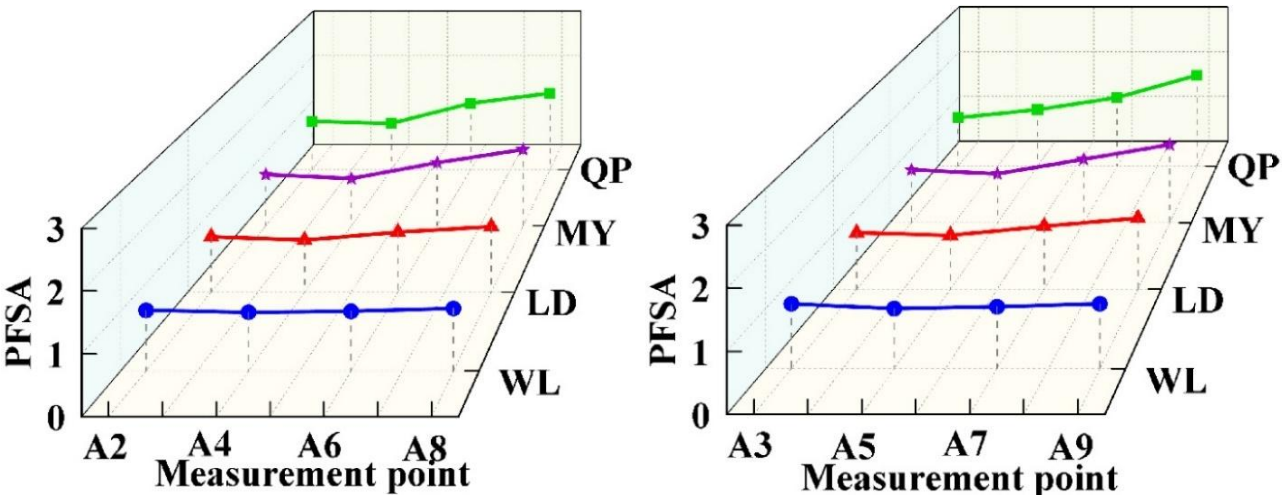

(c) (d)

Figure 15 PFSA variation curves: (a) the measurement points of external corners with 0.4 g input peak ground acceleration; (b) the measurement points of internal corners with 0.4 g input peak ground acceleration; (c) the measurement points of external corners with 0.6 g input peak ground acceleration; (d) the measurement points of internal corners with 0.6 g input peak ground acceleration.

As illustrated in **Figures 15 (c)** and **(d)**, when the peak input acceleration reaches 0.6 g, the pattern resembles that observed at 0.4 g. However, it is worth noting that the PFSA values for A6 to A8 show a certain degree of reduction, and it can be seen that the growth rate of the PFSA decreases. This phenomenon can be explained by the increased excitation amplitude and persistent influence of repeated sequence of strong earthquakes, which cause numerous cracks within the slope. These cracks obstruct seismic wave propagation and reduce the effectiveness of energy transfer, thereby decreasing the growth rate of the PFSA.

The Fourier spectrum of MY and QP seismic motions at various measurement points on the slope surface is illustrated in **Figure 16**, with an input peak acceleration of 0.4 g. From the results of **Figures 16 (a)** and **(b)** at A1 to A3, the dominant frequency range for MY seismic motion is between 3 Hz to 5 Hz, whereas for QP seismic motion, it is between 15 Hz to 20 Hz. As elevation increases beyond the A3, the low-frequency energy of both MY and QP seismic motions progressively shifts to higher frequencies, concentrating in the ranges of 23 to 25 Hz for MY seismic motion and 47 to 53 Hz for QP seismic motion. This observation suggests that predominant frequency band of PLGMs exhibits a transition from lower to higher frequencies as elevation increases. The results show that rock mass at the higher elevation is more sensitive to the high-frequency energy of PLGM, potentially due to the influence of SMVPS, as will be discussed in the next section. Furthermore, as elevation increases, the PFSA amplification effect of QP seismic motion exceeds that of MY seismic motion, highlighting that the energy transfer in the frequency domain of PLGM varies with its characteristics. In general,

higher frequency domain components lead to more severe dynamic responses.

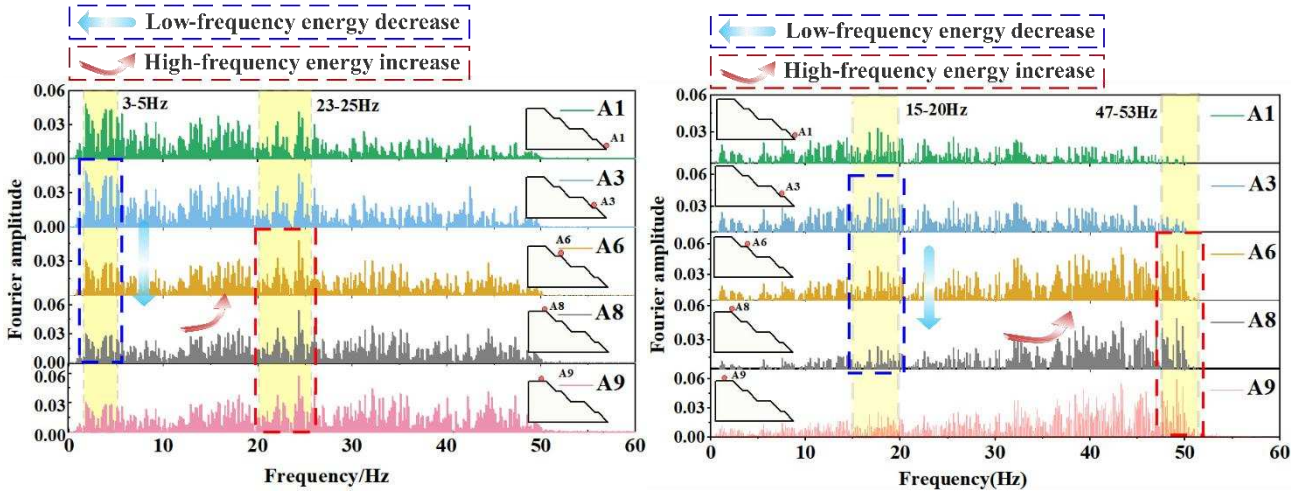

Figure 16 The Fourier spectrum at A1-A9 on the slope surface: (a) MY seismic motion; (b) QP seismic motion.

4.3 Time-frequency domain energy analysis using wavelet package transform

Real earthquake waves possess complex frequency components with varied and uneven energy distribution across different frequency bands. These frequency components can induce distinct dynamic responses, leading to unique time-frequency characteristics. While the FFT converts time-domain information of seismic waves into frequency-domain by decomposing signals into sinusoidal or cosine functions, it does not capture how frequencies change over time. To address this limitation, this research employs wavelet package transforms to explore the time-frequency characteristics of different seismic motions. Wavelet analysis is a signal processing method that utilizes a fixed window area with a variable shape, enabling precise localization in both time and frequency domains. This method is especially effective for analyzing seismic signals, which often include relatively low-frequency components (Rasheed et al., 2023). The decomposition spectrum of the wavelet package transform is illustrated in **Figure 17**. In this experiment, the accelerometer sampling frequency is set to 512 Hz, providing an analysis frequency range of 0-256 Hz. Selecting an appropriate decomposition level is essential. If the level is too low, the frequency bands will be too broad, whereas excessive decomposition can reduce frequency resolution. To balance resolution and accuracy, a 6-level wavelet packet decomposition is selected, resulting in 64 distinct wavelets (Wu et al., 2009). Various wavelet basis functions, including Haar, Daubechies, Symlets, Morlet, and Mexican Hat wavelets, each exhibit distinct advantages and are suited for specific applications in signal processing. The optimal selection depends on key characteristics such as

orthogonality, support length, regularity, and symmetry. (Yaghmaei et al., 2010). For this analysis, Daubechies wavelets are selected due to their excellent orthogonality and smooth decomposition properties. Specifically, Daubechies (db4) is used as the wavelet basis for data analysis in these experiments (Yaghmaei et al., 2013).

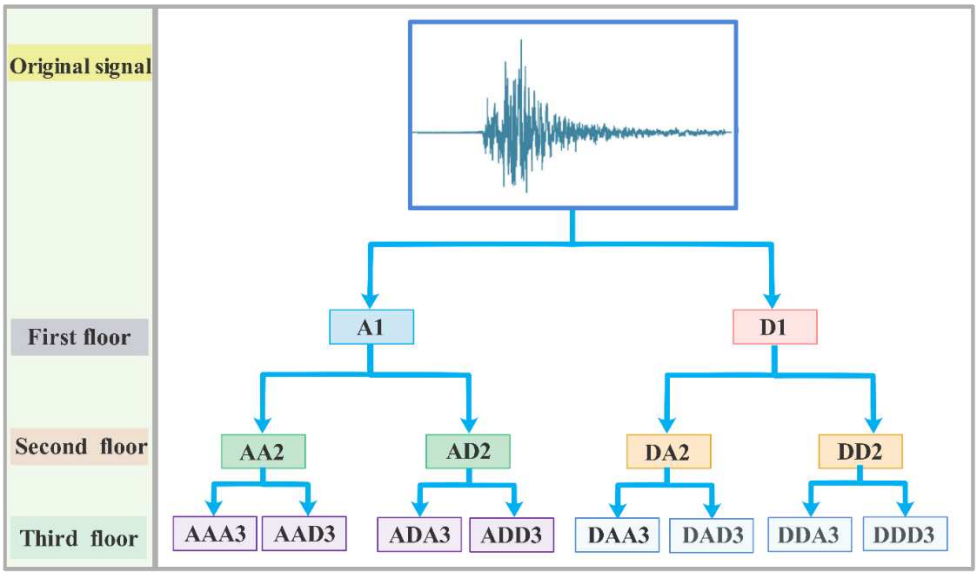

Figure 17 The decomposition spectrum of the wavelet package transform.

Figure 18 (a) shows the time-frequency distribution characteristics of the QP seismic motion at various measurement points on the slope, with an input peak acceleration of 0.4 g. The distribution shows that seismic energy is predominantly concentrated between 4s and 6s in the time domain, which corresponds to a decrease in velocity pulse duration. In the frequency domain, the energy is primarily concentrated across a broad band: from A2 to A4, the dominant frequencies span 15 Hz to 20 Hz, while from A6 to A8, the energy progressively shifts to higher frequencies, concentrating between 47 Hz and 53 Hz.

Similarly, **Figure 18 (b)** illustrates the time-frequency distribution characteristics of the MY seismic motion at various measurement points on the slope with the same input peak acceleration of 0.4 g. The time-frequency distribution shows that seismic energy is concentrated between 3 s and 6 s in the time domain, corresponding to the duration of the velocity pulse duration. In the frequency domain, the energy is distributed across a broad band: from A2 to A4, it spans 3 Hz to 5 Hz, while from A6 to A8, it shifts from lower frequencies to between 23 Hz and 25 Hz. A strong correlation is observed between the SMVPS and the energy release segment in PLGM. Additionally, the response of rock mass materials to the frequency domain components of seismic motions varies with elevation and is closely related to the SMVPS. This demonstrates that the characteristics of the velocity pulse are the primary factors influencing the differences in the dynamic response of rock mass materials at various elevations in the frequency domain. Different pulse characteristics lead to varied response behaviors, with higher frequency domain components causing more intense dynamic responses.

The above discussed results provide additional validation for both the time domain and frequency domain analyses. Additionally, the wavelet energy amplitude analysis indicates that the time-frequency domain energy of QP seismic motion is considerably higher than that of MY seismic motion, with energy ratios of 4.57, 5.07, 6.50, and 7.50 from A2 to A8. This finding aligns with the DAAF analysis, confirming a greater disparity in dynamic response as elevation increases.

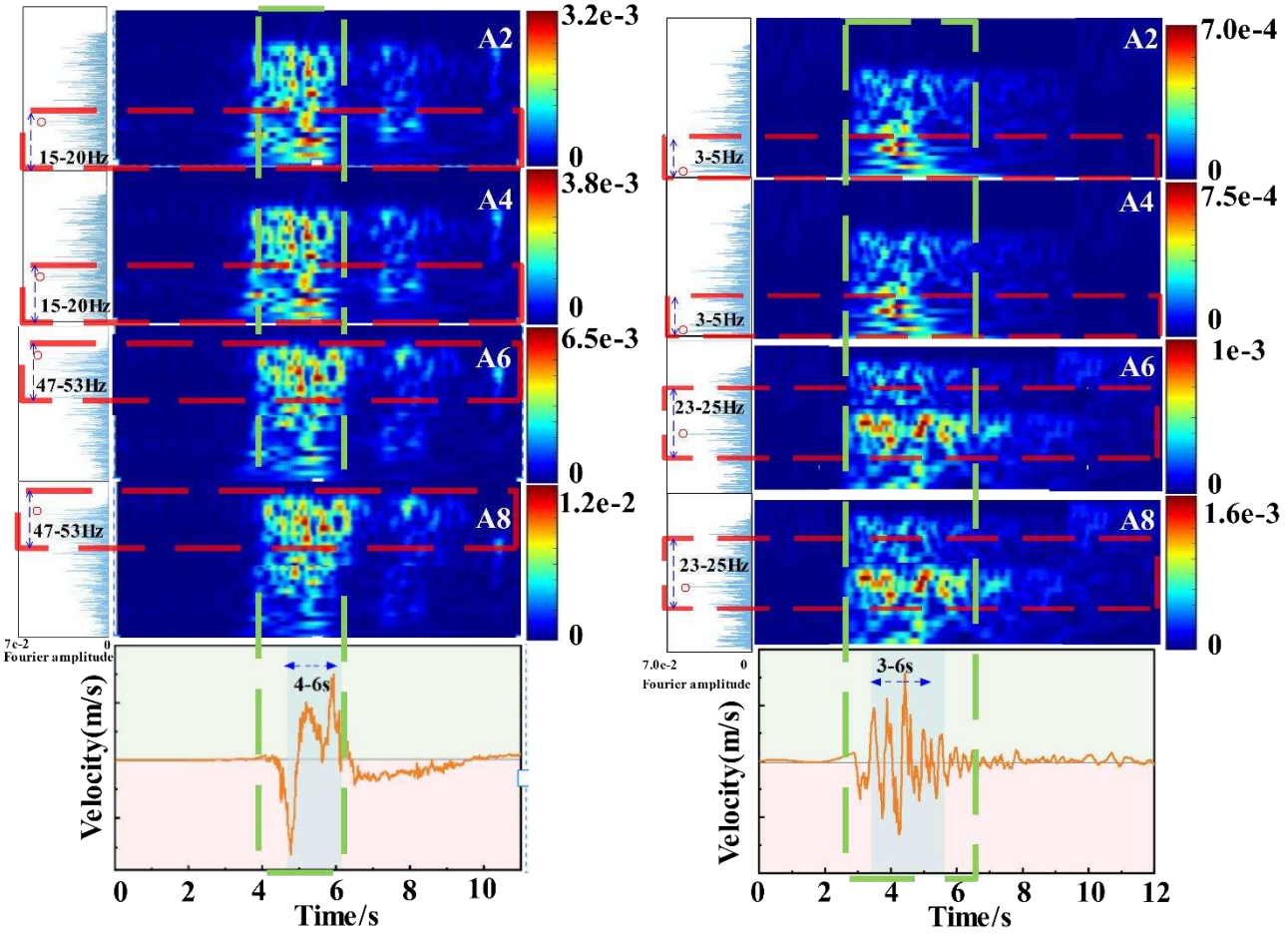

(a) (b)

Figure 18 Time-frequency characteristics of different measurement points of slope: (a) QP seismic motion; (b) MY seismic motion.

4.4 Verification of ground motion energy effect based on energy analysis

Arias intensity (I_a) offers a clear physical interpretation by quantifying the total energy imparted by seismic motion. It integrates factors such as amplitude, duration, and frequency of ground movement, thereby providing a more precise representation of the energy released by a seismic event as recorded by the instrument. By

743 incorporating these aspects, I_a gives a comprehensive measure of energy experienced during an earthquake and
744 enhances the understanding of its impact (Wei et al., 2024). In this research, an evaluation index based on I_a is
745 introduced to characterize the energy amplification effect of ground motion on slopes. I_a quantifies the energy
746 intensity of seismic motions by integrating the squared acceleration time history data over the event's duration
747 (Liu et al., 2024). To assess the dynamic response of the slope under different seismic motions, this study
748 proposes the Arias Intensity Amplification Factor (AIAF) as a parameter. AIAF is defined as the ratio of the I_a
749 at any measurement point on the slope to that at the reference shaking table, effectively reflecting the energy
750 released by ground motion. It can be calculated using **Equation (14)**.

751 $$I_a = \frac{\pi}{2g}\int_0^t a^2(t)dt \tag{14}$$

752 where, t is the duration of each excitation, g is the gravity acceleration, and $a(t)$ is the seismic motion
753 acceleration time history.

754 The results depicted in **Figures 19 (a)** and **(b)** demonstrate that AIAF values consistently increase with
755 elevation, whether measured at the internal or external corners of the slope. These findings are consistent with
756 the notion that the slope exhibits an elevation amplification effect. Among the seismic motions, QP seismic
757 motion exhibits the most pronounced increase, particularly at the crest of the slope, signifying that QP seismic
758 motion delivers the greatest amount of seismic energy. The peak AIAF value at the top of the slope underscores
759 this region as the most vulnerable to damage during seismic activity. This observation aligns with the previously
760 discussed DAAF analysis results, confirming that the ground motion energy is concentrated at the top of the
761 slope. Under QP seismic motion, as the peak acceleration increases, the AAF value at the top of the slope
762 gradually decreases, demonstrating a distinct nonlinear dynamic response. The dynamic response order is
763 observed to be: QP seismic motion > MY seismic motion > LD seismic motion > WL seismic motion. This is
764 due to the prominent SMVPS in the velocity time history of QP seismic motion, resulting in a concentrated
765 release of energy and pronounced acceleration during propagation. This, in turn, enhances the wave field
766 superposition effect at the top of the slope, making QP seismic motion induce the most intense dynamic
767 response. It is also worth noting that the AIAF values at the internal corners are significantly higher than those
768 at the external corners. This discrepancy occurs because the external corners are more prone to displacement
769 toward the free surface due to the repeated tensile and shear forces exerted by the ground motion, which
770 increases the likelihood of cracking and energy absorption. Consequently, the AIAF values at the external
771 corners tend to be lower compared to the internal corners.

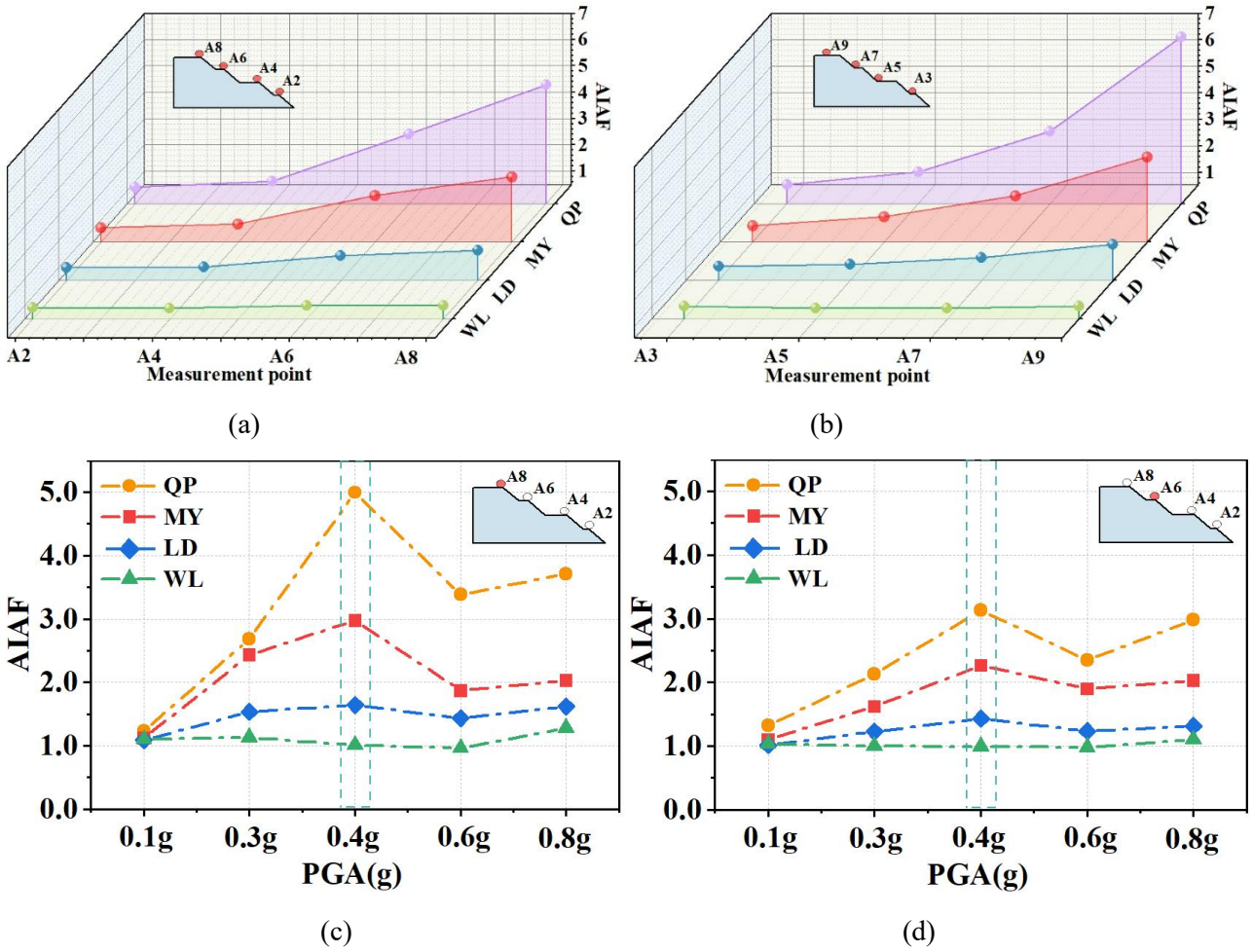

Figure 19 The value of AIAF under the various peak acceleration: (a) the external corners with 0.4 g input peak ground acceleration; (b) the internal corners with 0.4 g input peak ground acceleration; (c) measurement point of A8 under various peak ground accelerations; (d) measurement point of A6 under various peak ground accelerations

Further analysis of the AIAF values under varying peak acceleration levels reveals the following trends, as illustrated in Figure **19 (c)** and **(d)** (measurement points A6 and A8). When the peak acceleration increases from 0.1g to 0.4g, the AIAF values at A6 and A8 show a gradual upward trend. This suggests that the slope remains in the elastic deformation stage during this phase, allowing seismic energy to propagate to the measurement points with minimal dissipation, thereby increasing the AIAF values continuously. However, when the peak acceleration reaches 0.6g, the AIAF values at A6 and A8 begin to decline. This indicates that the slope has transitioned from the elastic stage to plastic failure. During this phase, seismic energy is significantly dissipated during propagation, reducing its transmission efficiency to the measurement points. As the peak acceleration further increases to 0.8g, the AIAF values exhibit only a marginal rise despite the higher input ground motion amplitude. This demonstrates a pronounced weakening of the slope's dynamic response,

accompanied by substantial energy dissipation. The energy loss primarily results from plastic deformation and slope failure, which absorb a portion of the ground motion energy. These observations align well with the AAF analysis results, further confirming the slope's dynamic evolution from elastic deformation to plastic failure.

4.5 Analysis of the influence of velocity pulse on the energy release rate of ground motion

From the previous analysis, it is evident that the short-term velocity pulse in ground motion significantly influences slope dynamic response by briefly releasing intense energy. Although QP, MY, and LD seismic motions all exhibit PLGM with distinct SMVPS, their dynamic response characteristics differ significantly. For instance, the dynamic response induced by QP seismic motion is notably more intense than that caused by MY or LD seismic motions, particularly at the top of the slope. The AIAF of QP seismic motion exceeds that of MY and LD seismic motions. However, the precise mechanisms driving these differences in dynamic response are not yet fully understood. To investigate the reasons behind these discrepancies, further research is needed, especially considering the limited studies on the contribution of SMVPS to ground motion energy. Therefore, as one of its key objectives, this study aims to explore the differences in dynamic response between PLGM and NPLGM affecting slopes. By integrating SMVPS, energy release time interval, and energy release magnitude, this research seeks to quantitatively assess the influence of the velocity pulse section on energy release rate. To this end, the ratio of seismic energy release (RSER) is introduced as a key metric for analysis:

$$RSER = \frac{\Delta I_a}{\Delta t_a} \tag{15}$$

where, ΔI_a is the I_a difference of the ground motion from the beginning to the end of the release of energy, and Δt_a is the time interval from the beginning to the end of the release.

Figure 20 illustrates the time-varying I_a curves for PLGM and NPLGM at measurement points A1, A6, and A8. The curves show that the I_a progressively increases with elevation from A1 to A8, with QP seismic motion exhibiting the most significant energy release, followed by MY, LD and WL seismic motions. Furthermore, the energy release effect of QP seismic motion intensifies with increasing elevation, resulting in a more pronounced dynamic response at higher points on the slope. Substituting the time-varying I_a curve at A8 into **Equation (8)** yields RSER values of 1.30E-4 for QP seismic motion, 1.02E-4 for MY seismic motion, and 0.80E-4 for LD seismic motion. For NPLGM, the RSER values are 0.28E-4 for the first energy release section and 0.07E-4 for the second section. The lower RSER value and the extended interval between the two energy release sections for NPLGM indicate a weaker overall effect. These results indicate that the QP seismic motion has the highest RSER value, demonstrating that under QP seismic motion, the energy input per unit time is maximized,

resulting in the most intense dynamic response of slope. In summary, PLGM leads to notably higher RSER values compared to NPLGM, confirming that the slope's dynamic response is more pronounced under PLGM. This highlights the importance of considering the energy release rate in evaluating seismic effects on slopes.

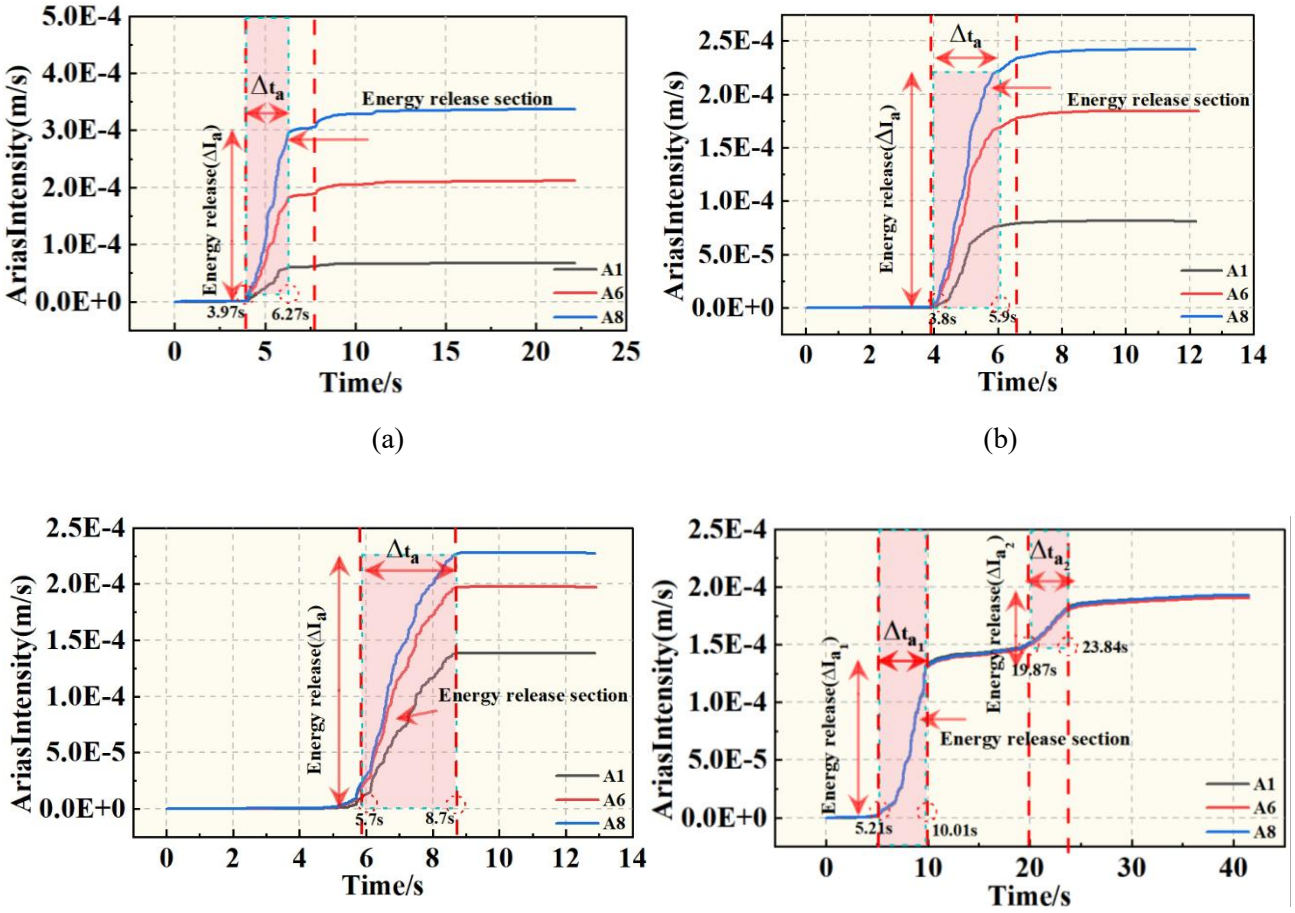

(a) (b)

(c) (d)

Figure 20 The impact of SMVPS on energy release rate: (a) energy releases section of QP seismic motion; (b) energy releases section of MY seismic motion; (c) energy releases section of LD seismic motion; (d) energy releases section of WL seismic motion.

5 Numerical analyses and verification

5.1 Model establishment and parameters selection

To investigate the dynamic response of the slope to different seismic motion characteristics, numerical simulation models were created based on shaking table tests. By rigorously applying geometric similarity principles and utilizing the Buckingham-π theorem for dimensional analysis, the geometric scaling ratio between the model and the prototype was established. Based on this scaling ratio and the dimensions of the model slope, the size of the numerical model was determined. The numerical model was subsequently designed

with dimensions of 165 cm in length and 80 cm in height, ensuring precise alignment with the height of the shaking table slope model. This dimensional consistency guarantees the accuracy and reliability of the simulation results. The width and height of the model's extended area were chosen following the recommendations of Bouckovalas and Papadimitriou, (2005) to minimize boundary effects and reduce wave reflections. The mesh generation of the model adhered strictly to the recommendations of Kuhlemeyer and Lysmer, (1973). The boundary conditions for the slope model were set with free-field boundaries on the sides and a viscous boundary at the bottom. According to **Equation (16)**, the local damping coefficient was calculated to be 0.157, assuming a 5% critical damping ratio (Xu et al., 2024). The monitoring scheme and the dynamic boundary setup for the numerical modeling are illustrated in **Figure 21**.

$$\beta_L = \pi\xi \tag{16}$$

where, β_L is the local damping coefficient, ξ is the critical damping ratio and π is a constant. The value of ξ for rock and soil material is generally 2 % ~ 5 %. Moreover, Kuhlemeyer and Lysmer, (1973) demonstrated that to accurately represent wave transmission through a model, the element size Δl should be less than approximately 1/10 to 1/8 of the wavelength corresponding to the highest-frequency component of the input wave, which can be determined **Equations (17)** to **(21)**:

$$\lambda_{\min} = C_s T_{\min} \tag{17}$$

$$C_s = \sqrt{\frac{E}{2\rho(1+\mu)}} = \sqrt{\frac{G}{\rho}} \tag{18}$$

$$T_{\min} = 1 / f_{\max} \tag{19}$$

$$\lambda_{\min} = \frac{\sqrt{\frac{E}{2\rho(1+\mu)}}}{f_{\max}} = \frac{\sqrt{G/\rho}}{f_{\max}} \tag{20}$$

$$\Delta l \le (\frac{1}{10} \sim \frac{1}{8})\lambda \tag{21}$$

where, C_s is wave velocity and T_{min} is the minimum period, E is the elastic modulus, ρ is the rock density, μ is the Poisson's ratio, G is the shear modulus, and f_{max} is the maximum frequency of the input wave. So, the maximum frequency of the input wave f_{max} in the shake table test is 40 Hz, and substituting it with the parameters in **Table 4** gives $\lambda_{min} \approx 20$ cm (Li et al., 2018; Ning et al., 2019; Liu et al., 2023). Ultimately, the mesh size is appropriately set at 2 cm.

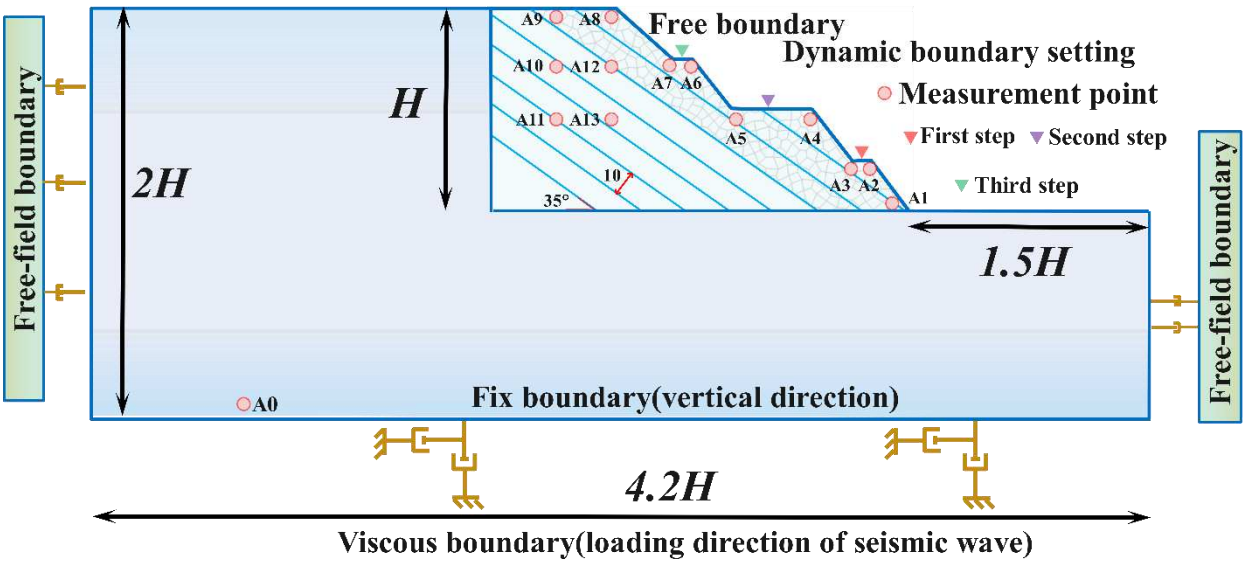

862

863 **Figure 21** UDEC numerical modeling.

864 **Table 4** the parameters of numerical simulation

Rock parameters		Joint parameters	
Elastic modulus *E*(Mpa)	50.0	Normal stiffness *kn* (Gpa/m)	2.0
Density ρ (kg/m^3)	2200	Shear stiffness *k*s (Gpa/m)	2.0
Friction angle φ (°)	36.0	Cohesion C (kPa)	3.0
Cohesion c (kPa)	20.0	Tension strength T(kPa)	10.0
-	-	Friction angle φ (°)	23.0

865

866 In the numerical simulation, the seismic motion is introduced from the base, which must first be converted
867 into stress before being applied to the model boundary, the conversion equations of velocity and stress are as
868 follows:

869 $$\sigma_n = 2(\rho C_p)V_n \tag{22}$$

870 $$\sigma_s = 2(\rho C_s)V_s \tag{23}$$

871 where, σ_s is the applied shear stress of SV wave, ρ is the rock density, C_s is the speed of the SV wave
872 propagation through the medium, σ_n is the applied normal stress of P wave, C_p is the speed of the P wave,
873 and V_n and V_s are the normal and shear velocity components of the input seismic motion, respectively.

874 5.2 Numerical results verification

875 To verify the accuracy and reliability of the numerical simulation, the time-history accelerations from the
876 shaking table tests are compared with the numerical analysis results. Specifically, **Figures 22 (a)** and **(b)** show
877 the acceleration time history curves at A0 for peak accelerations of 0.4 g and 0.6 g under MY seismic motion.

The amplitudes of the numerical simulations and shaking table tests are nearly identical, though minor discrepancies are observed at the beginning of the time-history. Additionally, the results indicate that the time-history accelerations from the numerical simulation are smoother and more stable compared to those from the shaking table tests. To quantitatively assess the consistency between numerical simulations and experimental results, the following computational formulations were applied, based on **Equation (24)** in this study:

$$\delta = \frac{|PGA_N - PGA_S|}{PGA_N} \tag{24}$$

the δ represents the errors, PGA_N denotes the PGA from the numerical simulation results, and PGA_S refers to the PGA from the shaking table tests.

The errors calculated from the peak acceleration data of the two methods are 8.4% and 2.9%, respectively, which fall within an acceptable range, confirming that the ground motion input in the numerical simulation aligns well with that of the shaking table tests. In order to further verify the validity of the numerical analysis, measurement points A2, A4 and A6 on the slope surface were selected. The numerical analysis results presented in **Figures 22 (c)** to **(h),** obtained under MY seismic motion, show that the PGA at these points increases with elevation, demonstrating a clear elevation amplification effect. The numerical simulation results align well with the shaking table test data. When the input acceleration peak is 0.4 g, the PGA errors for A2, A4, and A6 are 8.4%, 7.8%, and 8.6%, respectively. When the input acceleration peak reaches 0.6 g, the PGA errors for A2, A4, and A6 are 2.1 %, 24.1 % and 14.1 %, respectively. These results confirm that the input waveforms of MY seismic motions in the numerical calculations match those used in the shaking table tests.

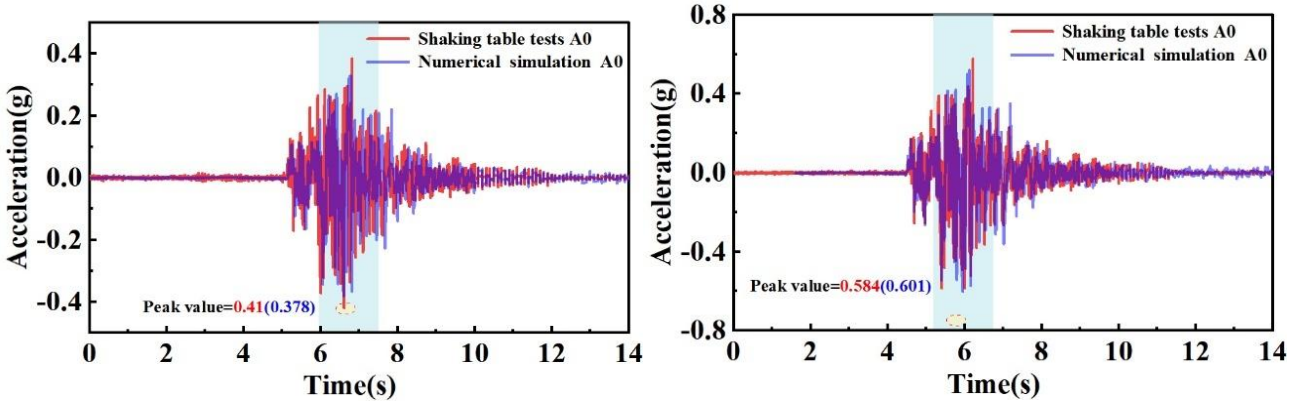

(a) (b)

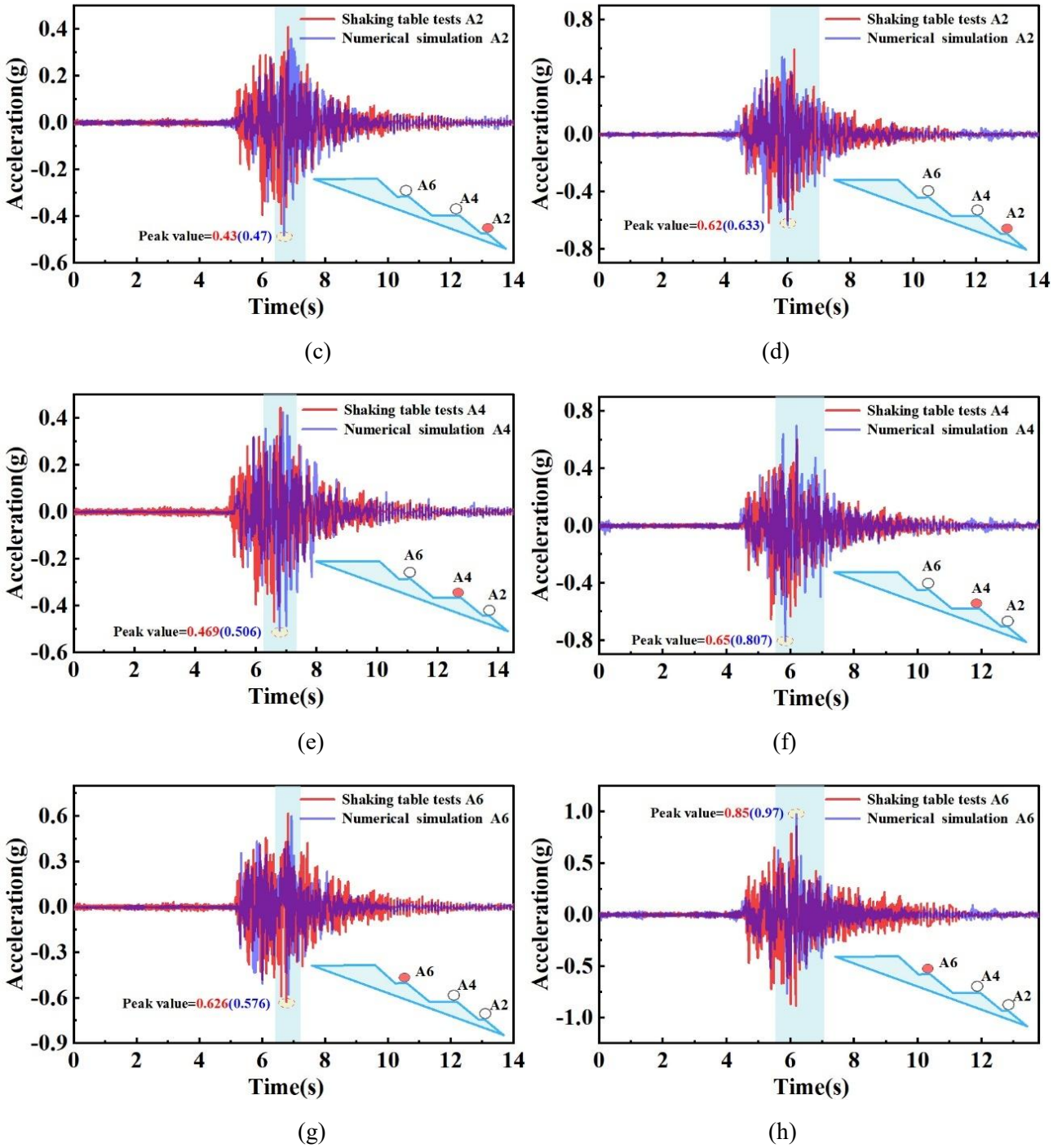

Figure 22 Comparison of acceleration response under the MY seismic motion with acceleration peak of: (a) 0.4 g, A0; (b) 0.6 g, A0; (c) 0.4 g, A2; (d) 0.6 g, A2; (e) 0.4 g, A4; (f) 0.6 g, A4; (g) 0.4 g, A6; (h) 0.6 g, A6.

To explore the differences in slope dynamic responses under various characteristic ground motions, the QP seismic motions were selected for detailed comparison. The comparison results for the input waveform at the A0 are shown in **Figures 23 (a)** and **(b)**. The errors calculated from the peak acceleration data are 5.6% and 0.97%, respectively. When the input acceleration peak is 0.4 g, the PGA errors for A2, A4, and A6 are 2.0%, 4.8%, and 0.57%, respectively. For an input acceleration peak of 0.6 g, the PGA errors at these points are 8.0%,

2.8%, and 5.4%, respectively, as presented in **Figures 23 (c)** to **(h)**. Additionally, the QP seismic motion inducing the strongest dynamic response was extracted from numerical simulations, and its displacement time-history at measurement point A8 was analyzed under various peak ground accelerations (0.1g, 0.4g, 0.6g, and 0.8g), with particular focus on peak ground displacement (PGD) and residual displacement (RD) variations. As shown in **Figure 23(i)-(l),** the PGD at A8 exhibits progressive increase with higher peak ground accelerations. Under lower accelerations (0.1g and 0.4g), the displacement time-history curves show RD = 0, confirming the slope maintains structural integrity within the elastic deformation range while preserving full load-bearing capacity (Yang et al., 2025a). A critical transition occurs at 0.6g input peak ground acceleration, where RD first appears (RD = 3.21 mm) in the time-history curve, indicating the slope's transition to plastic deformation. When the input peak ground acceleration increases to 0.8g, both PGD and RD show continuous growth, with RD reaching 9.175 mm, indicating the progressive development of slope failure.

These results, which clearly illustrate the slope's dynamic evolution from elastic deformation to plastic failure (consistent with time-domain analyses indicating a rapid transition at 0.6g input peak ground acceleration), also demonstrate that the numerical simulation agrees with the shaking table test results, further validating the numerical analysis accuracy.

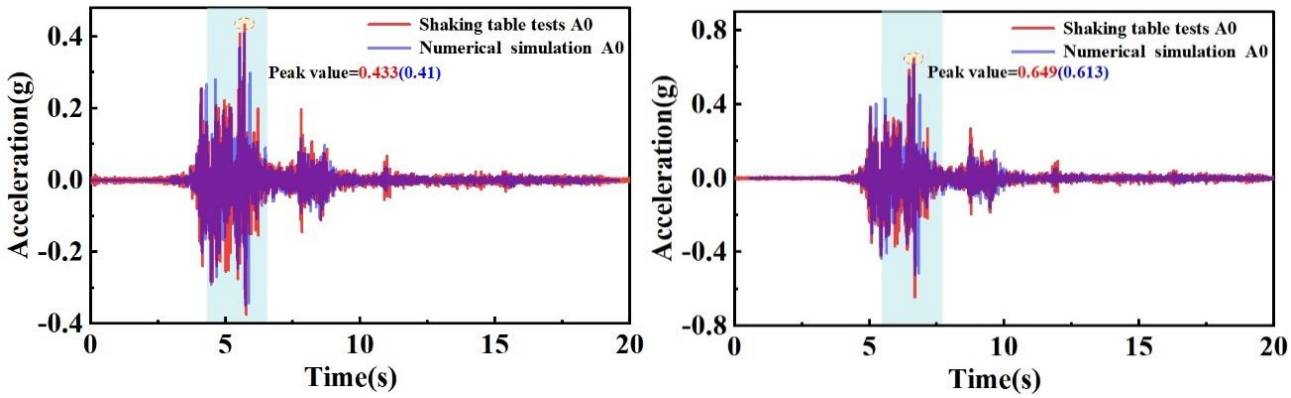

(a)

(b)

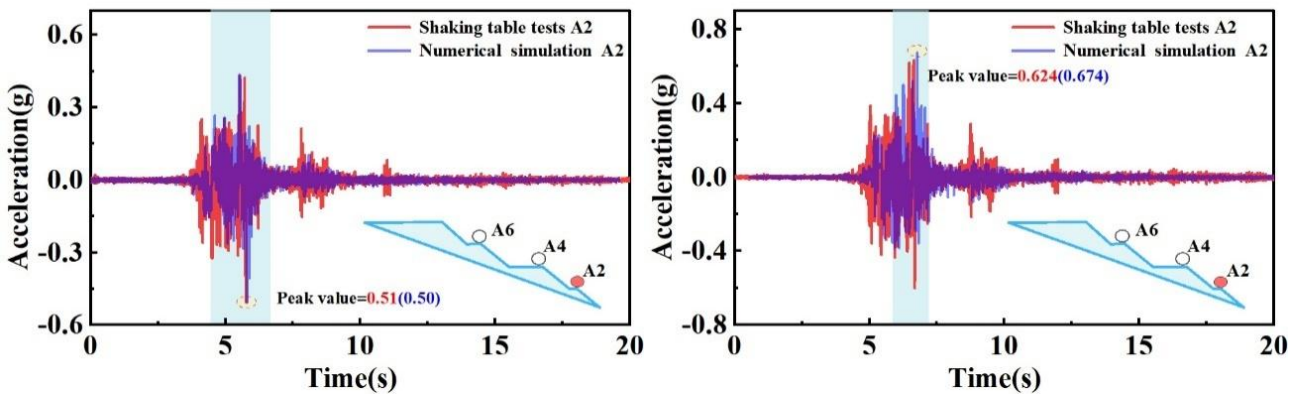

(c)

(d)

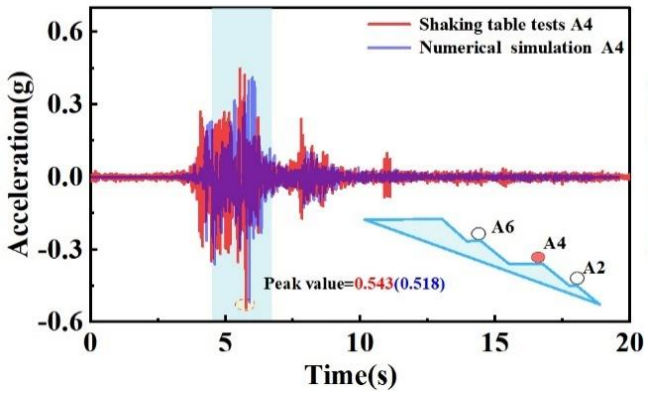
Shaking table tests A4
Numerical simulation A4
Acceleration(g)
Time(s)
A6
A4
A2
Peak value=0.543(0.518)

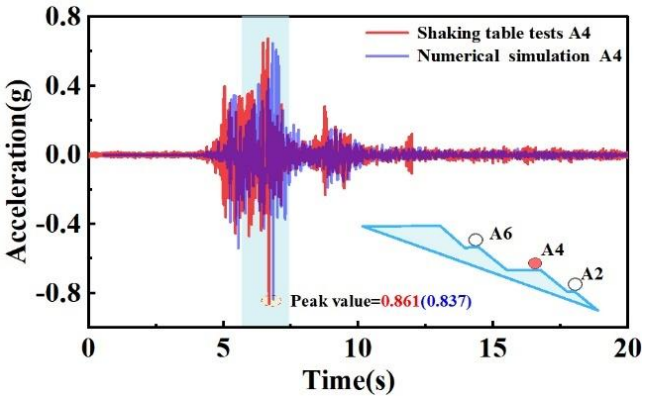
Shaking table tests A4
Numerical simulation A4
Acceleration(g)
Time(s)
A6
A4
A2
Peak value=0.861(0.837)

(e) (f)

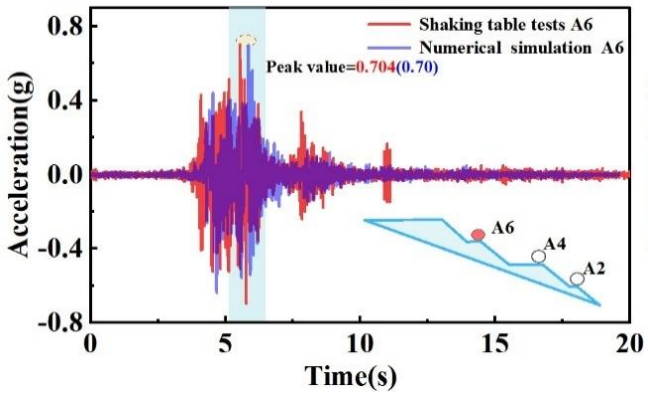
Shaking table tests A6
Numerical simulation A6
Acceleration(g)
Time(s)
A6
A4
A2
Peak value=0.704(0.70)

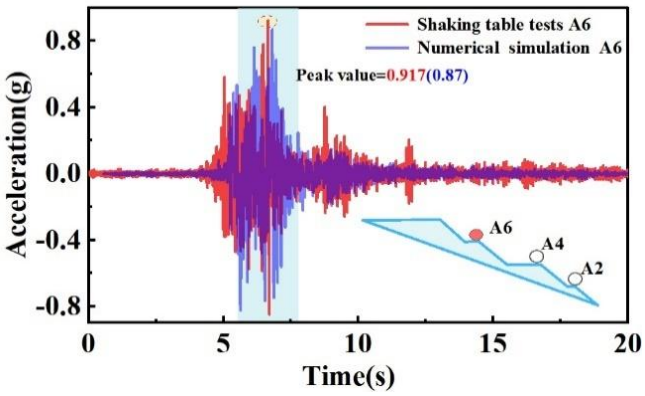
Shaking table tests A6
Numerical simulation A6
Acceleration(g)
Time(s)
A6
A4
A2
Peak value=0.917(0.87)

(g) (h)

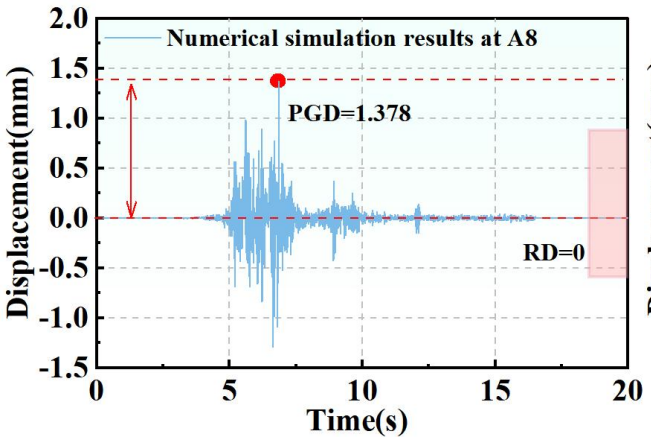
Numerical simulation results at A8
Displacement(mm)
Time(s)
PGD=1.378
RD=0

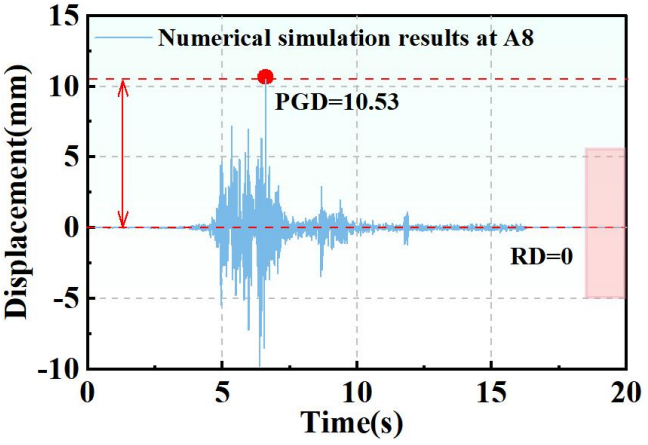
Numerical simulation results at A8
Displacement(mm)
Time(s)
PGD=10.53
RD=0

(i) (j)

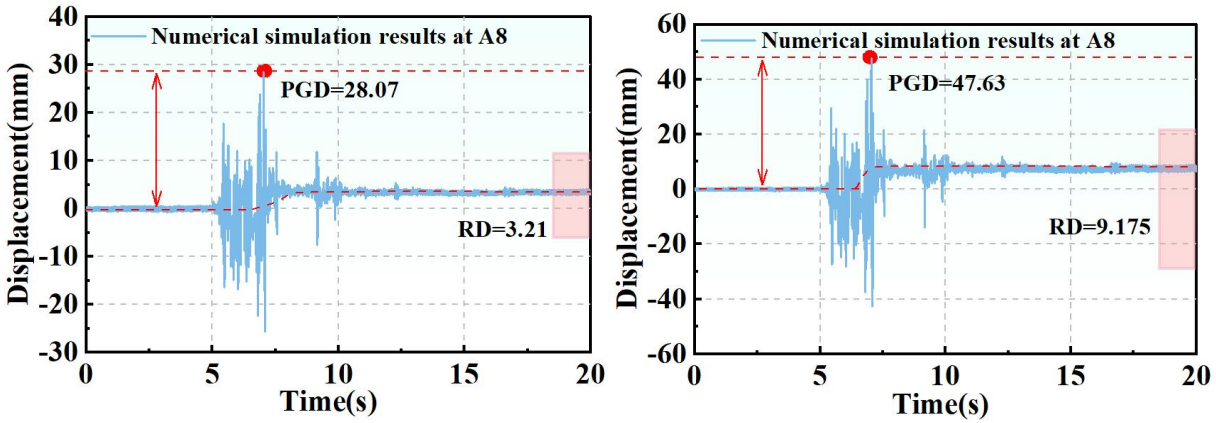

(k) (l)

Figure 23 Comparison of acceleration and displacement response under the QP seismic motion with acceleration peak of: (a) 0.4 g, A0; (b) 0.6 g, A0; (c) 0.4 g, A2; (d) 0.6 g, A2; (e) 0.4 g, A4; (f) 0.6 g, A4; (g) 0.4 g, A6; (h) 0.6 g, A6; (i) 0.1g, A8 (displacement); (j) 0.4g, A8 (displacement); (k) 0.6g, A8 (displacement); (l) 0.8g, A8 (displacement).

To ensure alignment between numerical simulations and shaking table test results, and to further explore failure modes associated with PLGM and NPLGM, the MY and QP seismic motions at 0.1 g, 0.4 g, and 0.8 g, along with WL seismic motion were selected for analysis. The results confirm consistent dynamic response strength for PLGM across varying characteristics. At a peak acceleration of 0.1 g, numerical simulation results depicted in **Figure 24 (a)** and **Figure 25 (a)** show slightly greater slope settlement induced by QP seismic motion compared to MY seismic motion, with QP causing 1.1 times greater displacement. As the acceleration reaches 0.4 g, as shown in **Figure 24 (c)** and **Figure 25 (b)**, settlement under QP seismic motion intensifies, causing local uplift and parallel cracks, particularly at the third step of the slope. In contrast, MY seismic motion results in minor settlement and less overall damage. The peak displacement under QP seismic motion is 1.36 times that of MY seismic motion. At a peak acceleration of 0.8 g, shown in **Figure 24 (e)** and **Figure 25 (c)**, settlement under QP seismic motion becomes significantly more intense than under MY seismic motion, leading to more severe damage at the top of the slope, exacerbated existing cracks, and significant fragment accumulation at the third step. In this case, a noticeable reduction is observed in the slope's overall integrity. Conversely, the MY seismic motion only causes a few vertical cracks at the top of the slope and some bulging at the toe of the slope. It is noteworthy that the peak displacement from QP seismic motion is 1.6 times greater than that from MY seismic motion. These results align with the shaking table tests analysis, showing that QP seismic motion causes more severe damage and a stronger dynamic response than MY seismic motion. Furthermore, the numerical simulation results shown in **Figures 24** confirm the consistency of the dynamic

response strength between PLGM and NPLGM, in agreement with the shaking table tests. As shown in **Figures 24 (a)** and **(b)**, at the peak acceleration of 0.1 g, the integrity of the slope is better preserved under WL seismic motion, resulting in less settlement compared to MY seismic motion. Displacement data reveals that the peak displacement under MY seismic motion is 1.2 times greater than that under WL seismic motion. As shown in **Figures 24 (c)** and **(d)**, by increasing the peak acceleration, MY seismic motion causes significantly greater damage on the slope compared to WL seismic motion. Specifically, settlement at the top is much more pronounced under MY seismic motion, with more evident cracks, local uplift and fragment accumulation. However, WL seismic motion only causes minor parallel cracks at the top of the slope and some initial cracks at the first step, with the slope maintaining overall integrity. The MY seismic motion produces approximately 1.5 times more displacement than WL seismic motion, resulting in stronger dynamic response and more damage. Furthermore, as shown in **Figures 24 (e)** and **(f)**, when the peak acceleration reaches 0.8 g, the slope experiences more severe settlement under MY seismic motion compared to WL seismic motion. In this case, existing cracks worsen, with new vertical fractures appearing at the third step and noticeable bulging at the toe of the slope. Displacement at the third step is more pronounced than at other locations. Under the WL seismic motion, cracks at the top of the slope undergo minor expansion, with slight increases in settlement. At the first step, cracks widen further and some local uplift occurs. Overall, the displacement is less significant compared to MY seismic motion, with MY seismic motion producing roughly 1.53 times more displacement than WL seismic motion. These findings confirm that PLGM produces a significantly stronger dynamic response and hence greater damage to the slope compared to NPLGM, which aligns with the findings from the shaking table test analysis.

In summary, the slope experiences the most intense dynamic response and seismic damage under QP seismic motion, followed by MY seismic motion, both of which exhibit PLGM and have significant impacts. In contrast, WL seismic motion, characterized by NPLGM, leads to the least severe effects. These findings are consistent with previous shaking table tests, which validated the numerical simulations, including failure observations and analyses across time, frequency, and time-frequency domains. The amplification effect of PLGM is shown to be significantly stronger than NPLGM, as indicated by AAF results, becoming more pronounced at higher levels. Moreover, based on AIAF, the energy amplification effect of PLGM is more significant than NPLGM, particularly at higher elevations. This is reflected in the RSER, where PLGM consistently exceeds NPLGM and intensifies with increasing elevation. These analysis indicators are interconnected and mutually explanatory, providing deeper insight into the failure mechanisms under QP seismic motion. By examining the internal

relationships among these indexes, a more comprehensive understanding of slope failure mechanism under QP seismic motion can be achieved.

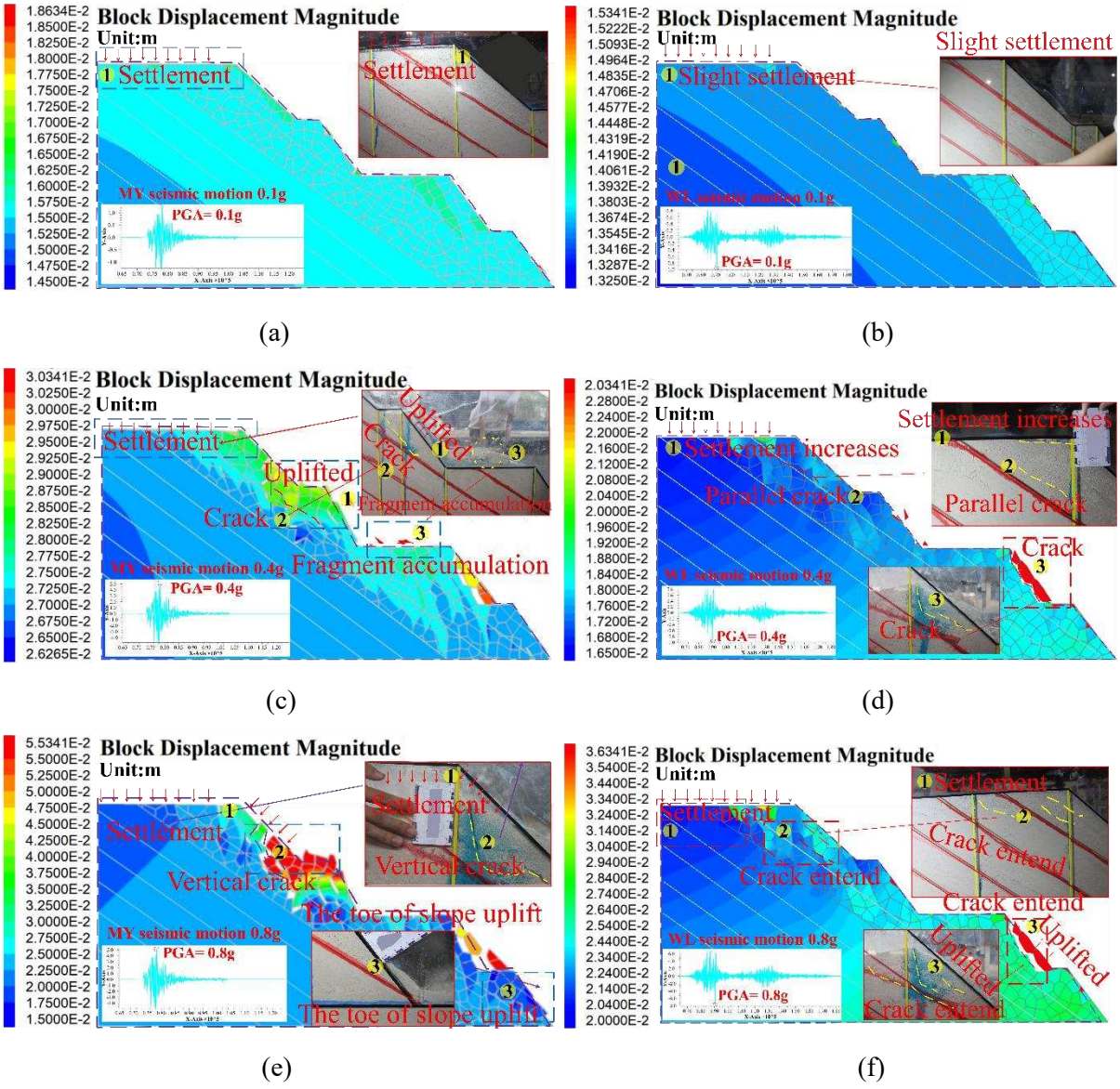

Figure 24 Comparison of asymptotic damage evolution process of the slope at different peak accelerations: (a) at 0.1g under MY seismic motion; (b) at 0.1g under WL seismic motion; (c) at 0.4g under MY seismic motion; (d) at 0.4g under WL seismic motion; (e) at 0.8g under MY seismic motion; (f) at 0.8g under WL seismic motion.

For analyzing the failure mechanism, the QP seismic motion and the final failure phenomena observed in the shaking table test were selected. As shown in **Figure 25 (a)**, when the input acceleration peak is 0.1 g, the slope remains largely undeformed, demonstrating considerable stiffness under low peak acceleration level. However, minor settlement occurs at the top of the slope, with displacement at the slope shoulder being greater than in other areas. At low peak acceleration, ground motion amplitude is not the main factor in causing deformation.

Instead, local damage is primarily caused by high-frequency components of the motion. As elevation increases, the energy of PLGM shifts toward higher frequencies, resulting in cyclic tension and shear at the top of the slope, leading to local settlement without sliding between layers. As shown in **Figure 25 (b)**, when the input acceleration peak is increased to 0.4 g, the amplification of the high-frequency components in higher-intensity PLGM amplifies settlement at the slope crest and induces significant local uplift. The increased intensity of seismic motion leads to a larger AIAF, in turn, amplifying the repeated transverse shear from the seismic waves. This gradually reduces the shear strength of the structural surfaces, leading to the development of parallel cracks between the layers. Under the combined influence of seismic forces and gravity, fragment ejection is observed. In **Figure 25 (c)**, when the input acceleration peak reaches 0.8 g, the AIAF is significantly amplified, intensifying the transformation of high-frequency components in the rock mass and resulting in a stronger dynamic response due to the higher RSER. Consequently, the top of the slope experiences a stronger seismic inertial force, resulting in increased seismic energy. This causes a sharp rise in settlement and the formation of parallel cracks, primarily in the upper region of the slope. The SMVPS of PLGM further amplifies the effect. The seismic motion, with its higher RSER, causes the structural surfaces to repeatedly open and close, continuously deteriorating the physical and mechanical properties of the rock mass in contact with the structural surfaces. This cumulative damage reduces the slope stability, leading to an increase in horizontal displacement between the layers. As the fragmented body at the top of the slope begins to protrude outward, debris accumulates, and cracks develop at the slope shoulder. Existing vertical cracks continue to expand, and new tensile cracks gradually form. Simultaneously, bulging occurs at the toe of the slope occurs, leading to slope instability.

Under PLGM, slopes typically undergo progressive failure initiated by tensile crack formation at the trailing edge. As seismic forces persist, the slope exhibits distinct deformation patterns: The fragmented body at the top of the slope protrudes outward, leading to debris accumulation and crack development at the slope shoulder. Existing vertical cracks continue to expand, while new tensile cracks gradually form. Simultaneously, bulging occurs at the toe of the slope, contributing to instability. Ultimately leads to global slope instability. This typical damage pattern was fully observed during the Qingping and Ludian earthquakes, as evidenced by case studies including: The Zengjiashan landslide in Pingxi Township, Hanwang Town, Mianzhu City. The Zhaojiagou landslide in Gaopu Village, Guozhu Township, Zhenxiong County (**Figures 26** (**b)** and **(d)**). Notably, shaking table tests successfully reproduced the failure mechanisms involving: collapse at slope top, tensile crack development at the rear fracture edge (**Figures 26** (**a) and (c)**). These experimental results not only confirm the

reliability of this failure mode but also demonstrate its repeatability-a critical feature for validation.

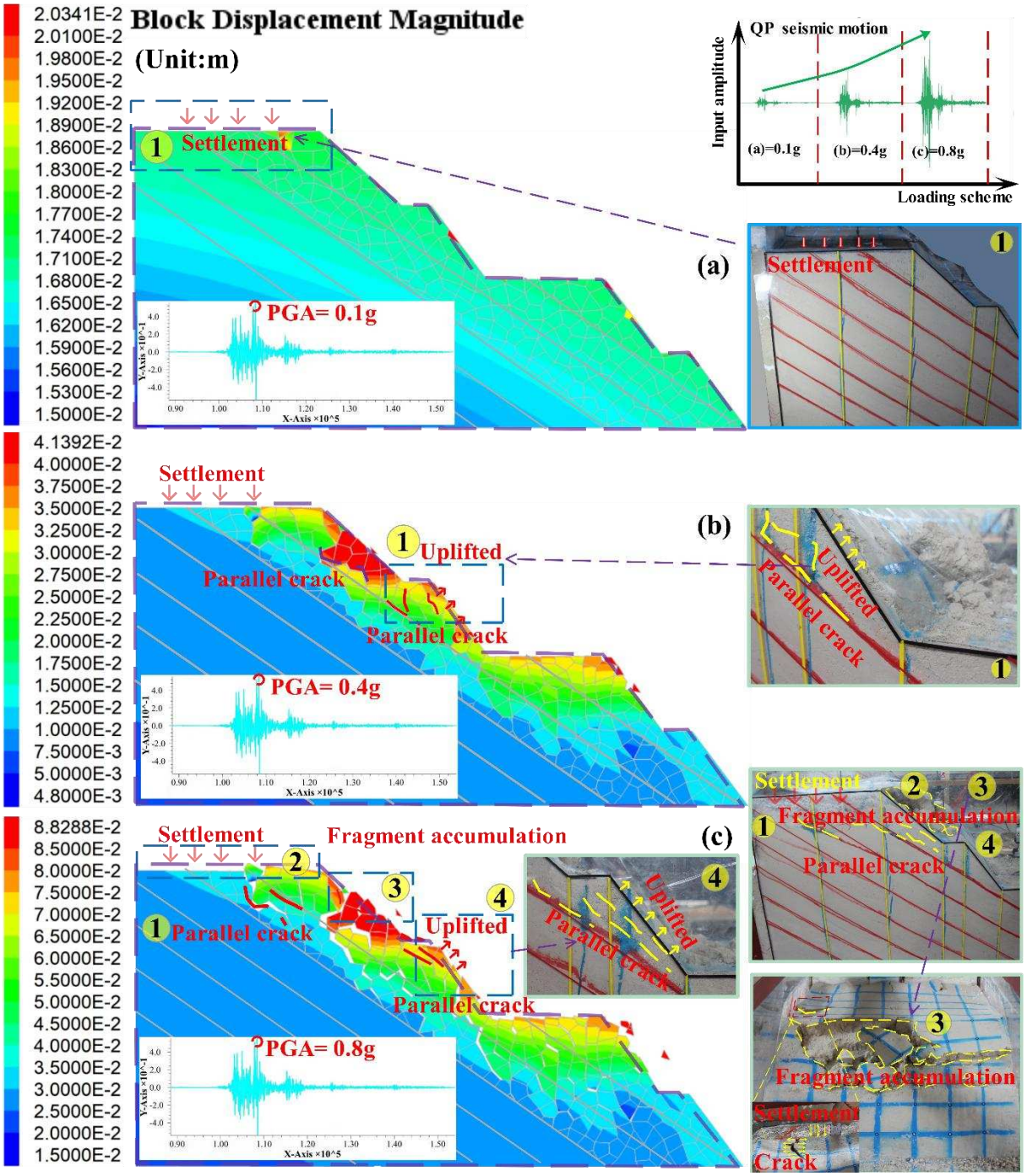

Figure 25 Comparison of slope damage phenomena: (a) 0.1g; (b) 0.4g; (c) 0.8g.

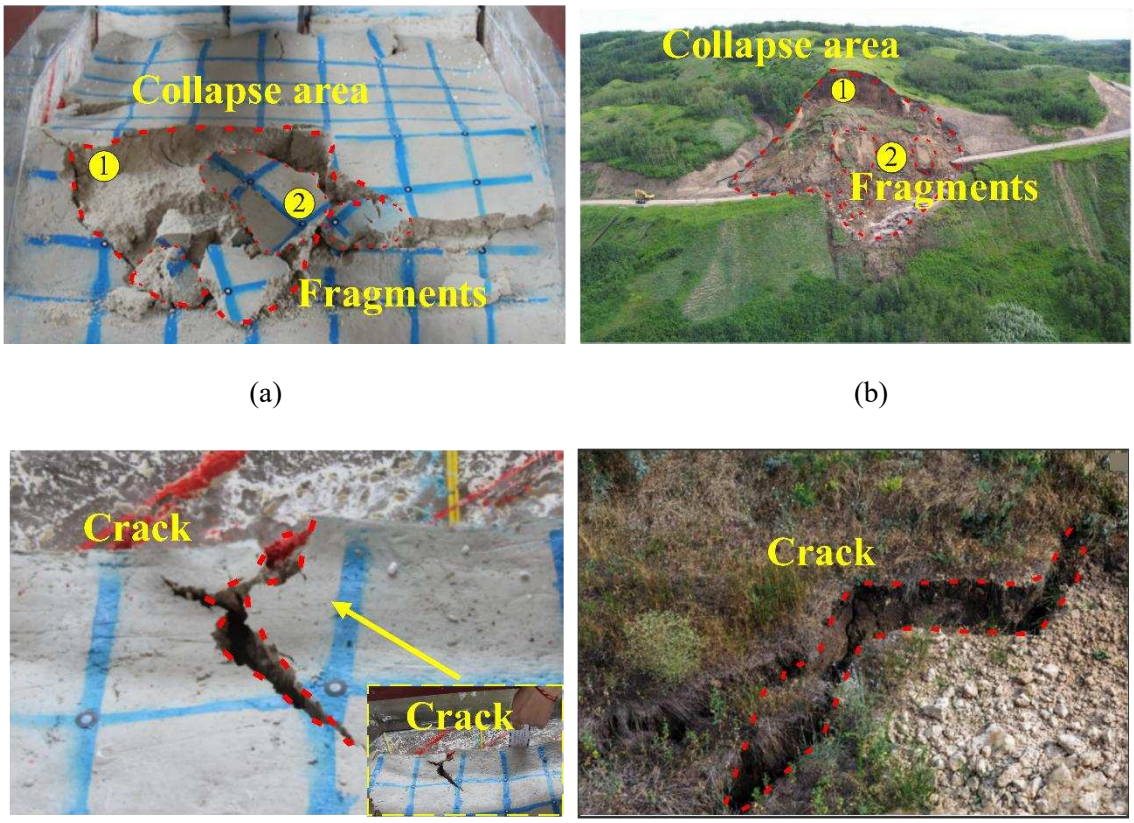

Figure 26 Comparison between experimental results and post-earthquake field investigations (a) the fragmented body at the top of the slope begins to protrude outward in shaking table test; (b) the fragmented body at the top of the slope begins to protrude outward of the Zengjiashan landslide in Pingxi Township, Hanwang Town, Mianzhu City; (c) the tension cracks at the slope top in shaking table test; (d) the tension cracks at the slope top of the Zhaojiagou landslide in Gaopu Village, Guozhu Township, Zhenxiong County.

6 Discussion

The dynamic response differences of slopes subjected to PLGM and NPLGM remain a key scientific issue to be solved in geotechnical earthquake engineering. Previous research has mainly focused on qualitative PGA-based comparisons, while quantitative investigations into the underlying mechanisms-such as frequency-domain energy transfer in PLGM and the relationship between velocity pulse segments and energy release-remain rarely investigated. These limitations hinder a comprehensive understanding of the seismic performance of slopes under near-fault PLGM. Therefore, in this study, the aforementioned issues are considered while offering novel insights from an energy-based perspective. The ratio of seismic energy release is proposed as a critical parameter fulfilling two analytical functions: effectively discriminating between PLGM and NPLGM, while simultaneously providing a quantitative metric to interpret the underlying mechanisms of dynamic

response among variations characteristics PLGM. Notably, the ratio of seismic energy release of PLGM is 319.54% higher than that of NPLGM, as evidenced in the cases of QP and WL seismic motions. This significant difference stems primarily from the characteristic velocity pulse segment unique to PLGM, the energy of PLGM is highly concentrated and released over an exceptionally brief duration, typically lasting between 1 and 3 seconds. In this study, the concentrated energy release period for QP seismic motion was measured at 2.3 seconds, with the velocity pulse segment occurring between 3.97s and 6.27s. This rapid release of energy generates high-amplitude velocity pulses, significantly increasing the energy density per unit time. This fundamental characteristic explains the notably larger Arias intensity amplification factor observed in PLGM compared to NPLGM. The acceleration time-history of PLGM displays distinct characteristics, with its waveform featuring several extremely high-amplitude peak pulses. For example, as shown in **Figure 8**, the QP seismic motion exhibits a pulse with a peak acceleration of 0.98g at 6.13 seconds. These sudden, intense pulses impose enormous impact inertial forces on the slope in a very short time frame, making it difficult for the slope to effectively adjust and recover its stress within such a brief period. As a result, when subjected to high-intensity PLGM, the slope enters the plastic deformation stage much sooner, thus accelerating its instability process. In contrast, the energy release process of NPLGM is relatively uniform and does not generate instantaneous, strong impact inertial forces. Consequently, PLGM produces more pronounced acceleration amplification effects and induces stronger dynamic responses than NPLGM. The risk of slope instability induced by PLGM is also significantly higher than that caused by NPLGM. This fundamental distinction directly explains the larger Arias intensity amplification factor observed in PLGM, which consequently leads to more pronounced acceleration amplification effects and stronger dynamic response than those observed in NPLGM. Furthermore, the investigation reveals a distinct energy transfer mechanism characterized by progressive high-frequency shifting with increasing elevation, according the Peak Fourier spectrum amplitude. This highlights the enhanced sensitivity of the rock mass at higher elevations to high-frequency energy components in PLGM. Simultaneously, energy transfer varies significantly among various PLGM, resulting in distinct dynamic response behaviors.

To investigate the energy transfer mechanisms of different PLGM, this study employs wavelet packet transform to reveal critical insights into PLGM characteristics. It extends the understanding of the relationship between velocity pulse segments and energy release, demonstrating a strong correlation between the seismic motion velocity pulse segment and energy release segments in PLGM. The results indicate that velocity pulse characteristics are the predominant controlling factor in progressive high-frequency energy transfer with

increasing elevation, where higher frequency components consistently trigger more intense responses under varying PLGM characteristics. For example, when comparing the QP and MY seismic motions, the ratio of seismic energy release of the QP seismic motion is 27.45% higher than that of the MY seismic motion, along with a greater Arias intensity amplification factor. From the frequency perspective, the Peak Fourier spectrum amplitude of the QP seismic motion is 36.36% higher than that of the MY seismic motion at higher elevations. This indicates that the high-frequency energy transfer effect at elevation is stronger for the QP seismic motion than for the MY seismic motion. Consequently, the dynamic response induced by the QP seismic motion is stronger than that induced by the MY motion. Specifically, this correlation manifests through distinct features: the velocity pulse segment exhibits the maximum ratio of seismic energy release, leading to a larger Arias intensity amplification factor. The progressive high-frequency shifting with increasing elevation—directly governed by seismic motion velocity pulse segment characteristics-enhances energy concentration in upper slope regions, thereby intensifying PLGM-induced dynamic responses through amplified seismic energy transfer. Consequently, this mechanism results in significant PGA amplification at higher elevations, which also explains the differences in dynamic response mechanisms between seismic motions with different pulse characteristics.

While the findings of this study enhance our comprehension of rock slope dynamics subjected to PLGM, certain factors should be considered. Although the selected PLGM records in this research demonstrate to a certain extent representativeness, they exhibit specific characteristics that warrant further investigation, particularly regarding varying pulse features. This consideration underscores the necessity to extend the scope of ground motion analysis to incorporate a more comprehensive range of seismic characteristics, including unilateral pulses and bidirectional pulses. Consequently, future research should focus on conducting in-depth quantitative analyses to systematically evaluate the influence of pulse characteristics on dynamic response variations (Chen et al., 2019). Additionally, this study investigates a representative high-steep cut slope in a high-intensity seismic zone through scaled model testing. The selected prototype site, situated within an active fault zone, exhibits regionally characteristic geological structures and demonstrates susceptibility to PLGM, thereby ensuring its engineering representativeness. Nevertheless, it is crucial to recognize that slope behavior is governed by site-specific characteristics, particularly three key controlling factors: (1) geometric configuration of the slope surface, (2) spatial distribution and mechanical properties of structural surfaces, and (3) spatial variability of geotechnical material properties. These factors collectively influence the slope's dynamic response characteristics under seismic loading conditions, highlighting several critical areas that

warrant further investigation (Liu et al., 2023; Chen et al., 2022). Future research should systematically explore the combined effects of slope surface morphology and structural surfaces, particularly focusing on varying joint angles and their interaction, as well as the different reinforcement measures in higher elevations of the slope. Furthermore, the investigations of this study not only align with previous research outcomes but also demonstrate some advancements in understanding the elevation amplification effect in PLGMs and the energy concentration characteristics within velocity pulse segments. These results provide a robust theoretical framework for subsequent research in related domains, while offering practical theoretical foundations and technical guidance for seismic fortification strategies in near-fault engineering structures.

7 Conclusions

This paper investigates the dynamic response characteristics of rock slopes subjected to near-fault pulse-like earthquakes through large-scale shaking table tests and complementary numerical simulations. Using different response parameters, it is shown that the results from shaking table tests and numerical simulations are in good agreement. By examining the time domain, frequency domain, and time-frequency domain, the study explores the differences in dynamic responses between PLGM and NPLGM. The dynamic response and instability mechanisms of rock slopes subjected to near-fault PLGM are then investigated, with the introduction of the RSER to quantify the differences. Based on the presented results, the following conclusions can be drawn:

(1) Under both PLGM and NPLGM, the slope shows significant elevation amplification and surface effects, with QP seismic motion causing the strongest amplification, followed by MY, LD, and WL, where the AAF values for QP, MY, and LD are 114.22%, 62.22%, and 31.11% higher than for NPLGM (WL seismic motion) at the slope shoulder (A8) when PGA = 0.4g. As PGA increases to 0.6g, the AAF for QP decreases by 30% at A8, while MY decreases by only 5.29%, and AAF values for LD and WL continue to rise. This indicates that QP seismic motion poses the greatest risk of severe structural damage.

(2) The analysis of DAAF also reveals that it progressively increases as elevation increases, exhibiting nonlinear energy amplification effects. The amplification effect of QP seismic motion at the top of the slope is 32.50% stronger than that of MY seismic motion when PGA= 0.4g. With the increase of PGA, DAAF gradually decreases, further characterizing the cumulative damage effect of the slope.

(3) Compared to NPLGM, PLGM significantly amplifies high-frequency energy with increasing elevation, which can induce localized damage. This damage accumulates, leading to substantial collapse in the slope's crest region, highlighting the heightened sensitivity of high rock masses to PLGM's high-frequency energy. Additionally, PLGM shows a shift in frequency bands with elevation, revealing notable differences in dynamic

responses at varying heights. These phenomena are closely linked to SMVPS, offering valuable insights into PLGM's impact on higher rock masses.

(4) The wavelet packet transform analysis reveals that the energy of PLGM is primarily concentrated during the SMVPS, resulting in increased energy release during seismic events. Time-frequency energy analysis, supported by both frequency-domain and time-domain methods, confirms that the energy spectra of PLGM shift toward higher frequencies with increasing elevation, further underscoring the impact of elevation on the spectral composition of PLGM. These findings provide a robust theoretical foundation for understanding elevation-dependent spectral characteristics of PLGM and offer valuable insights for seismic design and performance assessment of high-steep slope structures in near-fault areas.

(5) The AIAF values for PLGM (QP, MY, and LD seismic motions) are significantly higher by 397.26%, 195.33%, and 64.32%, respectively, compared to NPLGM (WL seismic motion) at A8 when PGA = 0.4g, indicating that the energy release of PLGM is notably greater compared to NPLGM, with has a high energy release capacity, with rapid energy release generating high-amplitude velocity pulses, particularly as elevation increases, highlighting the distinct elevation amplification effects between PLGM and NPLGM. This difference is especially evident when comparing PLGM with varying characteristics. These findings are consistent with DAAF analysis, confirming the reliability of the results.

(6) The RSER quantitatively explains the differences in dynamic response, with PLGM showing a 319.35% and 229.03% higher energy release rate per unit time compared to NPLGM, based on PLGM (QP, MY seismic motion), and NPLGM (WL seismic motion). This pattern highlights the distinct energy release characteristics of PLGM, which consistently enhance its energy release compared to NPLGM. Additionally, PLGM induces enhanced dynamic responses compared to NPLGM. These findings not only provide a deeper quantitative understanding of the mechanisms behind the dynamic response differences but also clarify the causes of varying dynamics among the varying characteristics of PLGM. These findings are consistent with the UDEC numerical simulation results, which show that QP seismic motion causes severe slope damage, with the greatest impact occurring at the top part of the slope. The shaking table test results further confirm that the QP seismic motion has the highest RSER, resulting in the highest AIAF, the most severe dynamic response, and hence, the greatest slope damage.

CRediT authorship contribution statement

Chunlei Xin: Methodology, Supervision, Funding acquisition, Investigation, Project administration, Writing

– original draft. **Lei Zeng**: Methodology, Data curation, Formal analysis, Writing – original draft. **Zhao Wang**: Formal analysis, Writing – Review and Editing; **Wenkai Feng:** Writing – Review and Editing, Funding acquisition; **Fei Yang:** Review and Editing, Investigation, Resources; **Iman Hajirasouliha:** Writing – Review and Editing, Validation, Conceptualization; **Xinyuan Yu:** Software.

Declaration of competing interest

The authors declare that they have no known competing financial interests or personal relationships that could have appeared to influence the work reported in this paper.

Data availability statement

The original data supporting the conclusions of this article will be made available by the authors, without undue reservation.

Acknowledgements

This research was supported by the National Natural Science Foundation of China (Grant Nos. 52108361 and 41977252), the Sichuan Science and Technology Support Program (Grant Nos. 2024ZYD0154 and 2024NSFSC0159), and the State Key Laboratory of Geohazard Prevention and Geoenvironment Protection (Grant Nos. SKLGP2022Z015 and SKLGP2020Z001). All the authors acknowledge the anonymous reviewers for their comments.

List of symbols

E	Elastic modulus	A	The original scale matrix
μ	Poisson's ratio	A_{ij}	Denotes the element in the i-th row and j-th column of A
c	Cohesion	A'_{ij}	The normalized matrix
φ	Internal friction angle	S	The vector of row sums
σ	Stress	$\sum_{i=1}^{n} S_i$	The total sum of all row sums
ε	Strain	w	The weight ratio of each method
t	Time	w_k	The normalized weight ratio for the k-th

d	Displacement	CI	The category indicator
v	Velocity	α	1×7 vector containing only -1 or 1
ξ	Damping ratio	PI	Pulse-like indicator
L	Geometric dimension	$t_{17\%,orgin}$	Attains 17% of the total of the original signal
ρ	Density	$t_{5\%,pulse}$	Attains 5% of the extracted pulse
a	Acceleration	ρ_i	Ratio of PGV(c_i) to PGA(c_i)
c_i	The i th IMF ranked form high frequency to low frequency	PPV	The difference of the peak velocity
E_{tot}	The integral of the squared velocity time history from 0 to the total duration.	E_{cn}	The cumulative energy, starting from the high-frequency component to the low-frequency component
PGV	Peak ground velocity	E_k	Ratio of the energy of the k-th half-cycle to the total energy in the velocity time history of ground motion
$V(\tau)$	The velocity time history of original ground motion record	Δt	The time lapse of the time history between two successive points
$SVHC$	The criterion for classification according to energy ratio thresholds	t_s	The pulse-starting points
ΔV_i	The velocity increment	$Score$	A score criterion
t_e	The pulse-ending points	I_a	Arias intensity
$a(t)$	Acceleration time-histories	ΔI_a	Difference of the ground motion from the beginning to the end of the release of energy
Δt_a	The time interval from the beginning to the end of the release.	β_L	Local damping coefficient
kn	Normal stiffness	ks	Shear stiffness
T	Tension strength	σ_n	Normal stress of P wave
σ_s	Normal stress of SV wave	C_s	Speed of the SV wave
C_p	Speed of the P wave	G	Shear modulus

References:

Antwi, Buah. P., Zhang, Y. B., Abdulrazig, M., Xiao, Y. 2024. Effect of geometry on the natural frequency and seismic response characteristics of slopes subjected to pulse-like ground motions. Computers and Geotechnics, 2024, 176(106777). https://doi.org/10.1016/j.compgeo.2024.106777

Bao, Y. J., Hu, H. Q., Gan, G. 2023. Seismic response analysis of slope reinforced by pile-anchor structures under near-fault pulse-like ground motions. Soil Dynamics and Earthquake Engineering. 2023, 164, 107576. http://10.1016/j.soildyn.2022.107576

Bao, Y. J, Huang, Y., Zhu, C. Q. 2021. Effects of near-fault ground motions on dynamic response of slopes based on shaking table model tests. Soil Dynamics and Earthquake Engineering. 2021, 149, 106869. http://10.1016/j.soildyn.2021.106869

Baker, J. W. 2007. Quantitative Classification of Near-Fault Ground Motions Using Wavelet Analysis. Bulletin of the Seismological Society of America. 2007, 97(5), 1486-1501. http://10.1785/0120060255

Bouckovalas, G. D., Papadimitriou, A. G. 2005. Numerical evaluation of slope topography effects on seismic ground motion. Soil Dynamics and Earthquake Engineering. 2005, 25(7-10), 547-558. http://10.1016/j.soildyn.2004.11.008

Chen, J. C., Wang, L. M., Wang, P., Che, A. L. 2022 Failure mechanism investigation on loess–mudstone landslides based on the Hilbert–Huang transform method using a large-scale shaking table test. Engineering Geology, 2022, 302, 106630. http://10.1016/j.enggeo.2022.106630

Chen, Z. Y., Liu, Z. Q. 2019. Effects of pulse-like earthquake motions on a typical subway station structure obtained in shaking-table tests. Engineering Structures. 2019, 198, 109557. http://10.1016/j.engstruct.2019.109557

Cui, S. H., Pei, X. J., Yang, H. L., Zhu, L., Jiang, Y., Zhu, C., Jiang, T., Huang, R. Q. 2023. Bedding slope damage accumulation induced by multiple earthquakes. Soil Dynamics and Earthquake Engineering. 2023, 173, 108157. http://10.1016/j.soildyn.2023.108157

Chen, X. Y., Wang, D. S., Zhang, R. 2019. Identification of Pulse Periods in Near‐Fault Ground Motions Using the HHT Method. Bulletin of the Seismological Society of America, 2019, 109(6), 2384-2398. http://10.1785/0120190046

Cheng, Y., Jiang, Y. N., Hou, Z. J., Zeng, R., Luo, H. Y. 2024. InSAR deformation observation and regional. severe earthquake hazard analysis of the 2016 and 2022 strong earthquake activities in Menyuan, Qinghai. Journal of Geomechanics, 2016, 30(6):965-977.http://10.12090/.issn.1006-6616.2023197

Cui, S. H., Pei, X. J., Huang, R. Q., Zhu, L., Yang, H. L, Liang, Y. F., Zhu, C. 2024. The analysis of seismic

induced progressive instability and failure mechanisms: A case study. International Journal of Rock Mechanics and Mining Sciences, 2024, 174, 105646. http://10.1016/j.ijrmms.2024.105646

Fan, G., Zhang, J. J., Wu, J. B., Yan, K. M. 2016. Dynamic Response and Dynamic Failure Mode of a Weak Intercalated Rock Slope Using a Shaking Table. Rock Mechanics and Rock Engineering. 2016, 49(8), 3243-3256. http://10.1007/s00603-016-0971-7

Fan, X. M., Juang, C. H., Wasowski, J., Huang, R. Q., Xu, Q., Scaringi, G., van Westen, C. J., Havenith, H. B. 2018. What we have learned from the 2008 Wenchuan Earthquake and its aftermath: A decade of research and challenges. Engineering Geology, 2018, 241: 25-32. http://10.1016/j.enggeo.2018.05.004

Fu, X. D., Sheng, Q., Li, G., Zhang, Z. P., Zhou, Y. Q., Du, Y. X. 2020. Analysis of landslide stability under seismic action and subsequent rainfall: a case study on the Ganjiazhai giant landslide along the Zhaotong-Qiaojia road during the 2014 Ludian earthquake, Yunnan, China. Bulletin of Engineering Geology and the Environment. 2020, 79(10), 5229-5248. http://10.1007/s10064-020-01890-z

Feng, W. K., Yang, L. J., Xin, C. L., Wang, Z., Yu, X. Y., Shuai, Y. X., Tian, Y. X. 2025. Design of a type of strike-slip active fault container for shaking table tests. Journal of Rock Mechanics and Geotechnical Engineering, 2025, 1674, 7755. https://doi.org/10.1016/j.jrmge.2025.03.001.

Geng, Y. L, Pu, W. C. 2023. Quantitative identification of pulse-like ground motions based on intrinsic time-scale decomposition technique. Soil Dynamics and Earthquake Engineering, 2023, 171. http://10.1016/j.soildyn.2023.107977

Gao, G. Y., Song, J. 2014. Predictive models for permanent displacement of slopes induced by near-fault pulse-like ground motions. Rock and Soil Mechanics, 2014, 35(05): 1340-1347. https://doi.org/10.16285/j.rsm.2014.05.010 (in chinese)

Guo, D. P., He, C., Xu, C., Hamada, M. 2015. Analysis of the relations between slope failure distribution and seismic ground motion during the 2008 Wenchuan earthquake. Soil Dynamics and Earthquake Engineering, 2015, 72, 99-107. https://doi.org/10.1016/j.soildyn.2015.02.001

Hayden, C. P., Bray, J. D., Abrahamson, N. A. 2014. Selection of Near-Fault Pulse Motions. Journal of Geotechnical and Geoenvironmental Engineering, 2014, 140(7). http://10.1061/(asce)gt.1943-5606.0001129

Itasca, 2014. Software Manual of FLAC3D, Universal Distinct Element Code (UDEC) User's Guide, Version 7.0. Itasca, Minneapolis, Minnesota, USA.

Kuhlemeyer, R. L., Lysmer, J. 1973. Finite element method accuracy for wave propagation problems. Journal of the Soil Mechanics and Foundations Division. 1973, 99(5), 421–427. https://doi.org/10.1061/JSFEAQ.000188

Li, L. Q., Ju, N. P., Zhang, S., Deng, X. X., Sheng, D. C. 2018. Seismic wave propagation characteristic and its effects on the failure of steep jointed anti-dip rock slope. Landslides. 2018, 16(1), 105-123. http://10.1007/s10346-018-1071-4

Li, X. J., Zhou, Z. H., Yu, H. Y, Wen, R. Z., Lu, D.W., Huang, M., Zhou, Y. N., Cu, J. W. 2008. Strong motion observations and recordings from the great Wenchuan Earthquake. Earthquake Engineering and Engineering Vibration, 2008, 7(3): 235-246. http://10.1007/s11803-008-0892-x

Li, D. J., Li, H. K., Fu, J. W., Yu, Q. S., Zhang, Y. B., Cheng, X. 2024. Permanent displacement limit analysis of jointed rock slope under the near-fault pulse-like ground motion based on the rotational − translational combined failure model and tensile strength cutoff. Computers and Geotechnics, 2024, 173, 106564. https://doi.org/10.1016/j.compgeo.2024.106564

Liu, X. R., Wang, Y., Xu, B., Zhou, X. H., Guo, X. Y., Miao, L. L. 2023 Dynamic damage evolution of bank slopes with serrated structural planes considering the deteriorated rock mass and frequent reservoir-induced earthquakes. International Journal of Mining Science and Technology, 2023, 33(9): 1131-1145. http://10.1016/j.ijmst.2023.07.004

Liu, H., Luo, Y., Wang, Y. S., Wang, W. P., Zhu, X., Li, J. Y., Zhou, Z., Jing, J. J. 2024 Influence of surface wave impedance ratios on the dynamic response and damage characteristics of slopes based on shaking table tests. Engineering Geology, 2024, 332, 107452. https://doi.org/10.1016/j.enggeo.2024.107452.

Li, Z. Y., Chen, G. Q., Han, Z. S., Hazarika, H., Xia, M. Y., Feng, C. F. 2024. The influence of pulse-like ground motion caused by the directivity effect on landslide triggering. Bulletin of Engineering Geology and the Environment. 2024, 83(1), 48. http://10.1007/s10064-023-03514-8

Lin, C. H., Li, H. H., Weng, M. C. 2018. Discrete element simulation of the dynamic response of a dip slope under shaking table tests. Engineering Geology. 2018, 243, 168-180. http://10.1016/j.enggeo.2018.07.005

Luo, J., Pei, X. J., Evans S, G., Huang, R. Q. 2019. Mechanics of the earthquake-induced Hongshiyan landslide in the 2014 Mw 6.2 Ludian earthquake, Yunnan, China. Engineering Geology. 2019, 251, 197-213. https://doi.org/10.1016/j.enggeo.2018.11.011

Luo, J., Evans S, G., Pei, X. J., Huang, R. Q., Liu, M., Dong, X. J. 2020. Anomalous co-seismic surface effects produced by the 2014 Mw 6.2 Ludian earthquake, Yunnan, China: An example of complex faulting related to Riedel shear structures. Engineering Geology. 2020, 266, 105476. http://10.1016/j.enggeo.2020.105476

Liu, P., Xu, Z. W. 2024. Directionality of Arias intensity in the Wenchuan Mw 7.9 earthquake, China. Engineering Geology. 2024, 335, 107530. http://10.1016/j.enggeo.2024.107530

Mukhopadhyay, S., Gupta, V. K. 2013. Directivity Pulses in Near-Fault Ground Motions-I: Identification, Extraction and Modeling. Soil Dynamics and Earthquake Engineering. 2013, 50, 1-15. http://10.1016/j.soildyn.2013.02.017

Miao, S. S., Su, L. J., Zhang, C. L., Liu, Z. Y., Wang, B., Dong, Z. B. 2024. Dynamic response characteristics and damage failure process of bedding rock slope in shaking table test. Bulletin of Engineering Geology and the Environment. 2024, 83(9), 358. http://10.1007/s10064-024-03843-2

Ning, Y. B., Zhang, G. C., Tang, H. M., Shen, W. C., Shen, P. W. 2019. Process Analysis of Toppling Failure on Anti-dip Rock Slopes Under Seismic Load in Southwest China. Rock Mechanics and Rock Engineering. 2019, 52(11), 4439-4455. http://10.1007/s00603-019-01855-z

Peng, Y. B., Han, R. J. 2024. A comprehensive categorization method for identifying near‐fault pulse‐like ground motions. Earthquake Engineering & Structural Dynamics, 2024. http://10.1002/eqe.4225

Pai, S., Kaynia, A. M., Bhasin, R. K., Paul, D. K. 2011. Earthquake Stability Analysis of Rock Slopes: a Case Study. Rock Mechanics and Rock Engineering, 2011, 45(2): 205-215. http://10.1007/s00603-011-0145-6

Panella, D. S., Tornello, M. E., Frau, C. D. 2017. A simple and intuitive procedure to identify pulse-like ground motions. Soil Dynamics and Earthquake Engineering, 2017, 94, 234-243. http://10.1016/j.soildyn.2017.01.020

Rasheed, A., Osama, M., Rafique, M., Tareen, A. D. K., Lone, K. J., Qureshi, S. A., Kearfott, K. J., Alam, A., Nikolopoulos, D. 2023. Time-frequency analysis of radon and thoron data using continuous wavelet transform. Physica Scripta. 2023, 98(10), 105008. http://10.1088/1402-4896/acf694

Song, J., Gao, G. Y. 2014. Sliding displacement of slopes under near-fault pulse-like ground motions. Chinese Journal of Rock Mechanics and Engineering, 2014, 33(02):317-326. https://doi.org/10.13722/j.cnki.jrme.2014.02.007

Song, J., Gao, G. Y., Chen, Q. S., Zhao, H. 2013. Dynamie Response of Soil Slope under Near-fault Gound Motions. China Earthquake Engineering Journal, 2013, 35(01):62-90. https:// 10.3969/i.issn.1000-0844.2013.01.0062

SeismoSoft. 2023. SeismoSignal user manual (Version 5.1.0). https://seismosoft.com/products/seismosignal/

Song, D. Q., Liu, X. L., Huang, J., Zhang, J. M. 2020. Energy-based analysis of seismic failure mechanism of a rock slope with discontinuities using Hilbert-Huang transform and marginal spectrum in the time-frequency domain. Landslides. 2020, 18(1), 105-123. http://10.1007/s10346-020-01491-7

Song, D. Q., Liu, X. L., Huang, J., Zhang, J. M., Nkwenti, B. N. 2021. Seismic cumulative failure effects on a reservoir bank slope with a complex geological structure considering plastic deformation characteristics using

shaking table tests. Engineering Geology. 2021, 286, 106085. http://10.1016/j.enggeo.2021.106085

Song, J., Xue, Y. L., Zhang, S., Ji, J., Gao, Y. F. 2024. Directionality of earthquake-induced slope displacements from numerical analysis and sliding block approaches. Engineering Geology. 2024, 339, 107638. http://10.1016/j.enggeo.2024.107638

Saaty, T. L. 1983. Priority setting in complex problems. 1983. IEEE Transactions on Engineering Management. 1983, EM-30(3), 140-155. 10.1109/TEM.1983.6448606

Shi, W. P., Zhang, J. W., Song, D. Q., Liu, X. L., Wang, E. Z., Zhao, J. J. 2023 Dynamic Response Characteristics and Instability Mechanism of High-Steep Bedding Rock Slope at the Tunnel Portal in High-Intensity Seismic Region. Rock Mechanics and Rock Engineering, 2023, 57(2): 827-849. https://doi.org/10.1007/s00603-023-03629-0

Tang, Y., Che, A. L., Cao, Y. B., Zhang, F. H. 2020. Risk assessment of seismic landslides based on analysis of historical earthquake disaster characteristics. Bulletin of Engineering Geology and the Environment. 2020, 79(5): 2271-2284. https://doi.org/10.1007/s10064-019-01716-7

Wang, C., Guo, M. Z., Chen, X. L., Gu, K. H., Gong, Y. F., Qi, Y. P., Yuan, D. D., Zhu, C., Chen, B. B. 2024. Damage evolution of the bedding rock landslide and debris landslide under earthquakes in the Three-rivers Basin. Engineering Geology. 2024, 339, 107631. http://10.1016/j.enggeo.2024.107631

Wei, B., Tan, H., Wan, K. C., Sun, Z. C., Li, S. S. 2024. Seismic performance of railway bridges with novel ductile piers under near-fault earthquakes. Transportation Geotechnics. 2024, 46, 101241. http://10.1016/j.trgeo.2024.101241

Wu, J. D., Lin, B. F. 2009. Speaker identification using discrete wavelet packet transform technique with irregular decomposition. Expert Systems with Applications. 2009, 36(2), 3136-3143. http://10.1016/j.eswa.2008.01.038

Wei, H., Tao, Z. G., He, M. C., Wu, H. G., Lv, X. Q., Yu, H. J., Weng, H. Q. 2024. The Cumulative Damage Evolution Law Of Multi-Anchor Circular Piles Reinforced Landslide Under Earthquake Action. Rock Mechanics and Rock Engineering. 2024, 57(8), 6321-6336. http://10.1007/s00603-024-03857-y

Wu, Q., Li,D. Q., Liu, Y., Du, W. Q. 2021 Seismic performance of earth dams founded on liquefiable soil layer subjected to near-fault pulse-like ground motions. Soil Dynamics and Earthquake Engineering, 2021, 143(106623) https://doi.org/10.1016/j.soildyn.2021.106623

Wang, X. W., Wu, S. Q., Cai, J. X., Liu, G. X. 2023. Optimal Pair Selection Applied to Sentinel-2 Images for Mapping Ground Deformation Using Pixel Offset Tracking: A Case Study of the 2022 Menyuan Earthquake (Mw 6.9), China. Remote Sensing, 2023, 15(19), 4735. https://doi.org/10.3390/rs15194735

Xin, C. L., Shuai, Y. X., Song, D. Q., Liu, X. L. 2024b. Dynamic interaction and failure mechanism in tunnel-

slope systems: Mitigation insights from shaking table tests and numerical analysis. Tunnelling and Underground Space Technology. 2024, 152, 105940. http://10.1016/j.tust.2024.105940

Xin, C. L., Yang, F., Feng, W. K., Wang, Z., Li, W. H. 2024a. Seismic responses and shattering cumulative effects of bedding parallel stepped rock slope: Model test and numerical simulation. Journal of Rock Mechanics and Geotechnical Engineering. 2024. http://10.1016/j.jrmge.2024.03.031

Xin, C. L., Wang, Z., Hajirasouliha, I., Yang, F., Li, W. H., Chen, T., Gao, B. 2022. Seismic response mechanisms of casing-shape composite tunnel lining: Theoretical analysis and shaking table test verification. 2022, 162, 107440. https://doi.org/10.1016/j.soildyn.2022.107440

Xin, C. L., Wang, Z. Z., Zhou, J. M., Gao, B. 2019. Shaking table tests on seismic behavior of polypropylene fiber reinforced concrete tunnel lining. Tunnelling and Underground Space Technology. 2019, 88, 1-15. http://doi.org/10.1016/j.tust.2019.02.019

Xu, B., Liu, X. R., Liang, Y., Zhou, X. H., Zhong, Z. L. 2024. Stability of bedded rock slopes subjected to hydro-fluctuation and associated strength deterioration. Journal of Rock Mechanics and Geotechnical Engineering. 2024, 16(8), 3233-3257. http://10.1016/j.jrmge.2023.09.043

Xin, C., Li, W. H., Wang, Z., Feng, W. K., Hajirasouliha I., Yu, X. Y. 2024c. Shaking table tests on the stability of dip and anti-dip rock slopes with discontinuitys induced by seismic motions. Engineering Geology. 2024, 341. 107707. http://10.1016/j.enggeo.2024.107707

Yang, D. X., Wang, W. 2012. Nonlocal period parameters of frequency content characterization for near-fault ground motions. Earthquake Engineering & Structural Dynamics. 2012, 41(13), 1793-1811. http://10.1002/eqe.2157

Yaghmaei-Sabegh, S. 2013. Wavelet-based Analysis for Pulse Period of Earthquake Ground-motions. International Journal of Engineering. 2013, 26(10A), 1135-1144. http://10.5829/idosi.ije.2013.26.10a.04

Yaghmaei-Sabegh, S. 2010. Detection of pulse-like ground motions based on continues wavelet transform. Journal of Seismology. 2010, 14(4), 715-726. http://10.1007/s10950-010-9193-8

Yang, F., Xin, C. L., Wang, Z., Feng, W. K., Hu, Y. P. 2025. Investigating Deformation and Failure Mechanisms of Discontinuous Anti-dip Bench Rock Slopes Through Shaking Table Tests and Numerical Simulations. Rock Mechanics and Rock Engineering, 2025a, 1-33. https://doi.org/10.1007/s00603-024-04346-y

Yang, C. W., Fan, J., He, Y. F., Xu, X. Q., Wang, L., Su, K. 2025. Mechanisms of earthquake-induced unstable rock masses initiation and rockfalls impact on open-cut tunnels: insights from shaking table tests. Acta Geotechnica, 2025b, https://doi.org/10.1007/s11440-025-02615-w

Yang, H. L., Cui, S. H., Pei, X. J., Fan, X. M, Lei, J. 2023. Multiple earthquake-induced progressive failure of

bedding slopes with a saturated weak layer: Shaking table model tests. Soil Dynamics and Earthquake Engineering, 2023, 170, 107906. https://doi.org/10.1016/j.soildyn.2023.107906

Zhang, Y. B., Xiao, Y., Wang, B. R., Tang, W. Y., Yu, P. C., Wang, W., Xu, P. Y., Antwi Buah, P. 2024. Directivity effect of the spatial distribution of co-seismic landslides affected by near-fault ground motions. Computers and Geotechnics. 2024, 170, 106263. http://10.1016/j.compgeo.2024.106263

Zhou, H. X., Che, A. L., Shuai, X. H., Cao, Y. B. 2024. Seismic vulnerability assessment model of civil structure using machine learning algorithms: a case study of the 2014 Ms6.5 Ludian earthquake. Natural Hazards. 2024, 120(7), 6481-6508. http://10.1007/s11069-024-06465-9

Zou, D. G., Han, H. C., Liu, J. M., Yang, D. X., Kong, X. J. 2017. Seismic failure analysis for a high concrete face rockfill dam subjected to near-fault pulse-like ground motions. Soil Dynamics and Earthquake Engineering. 2027, 98, 235-243. http://10.1016/j.soildyn.2017.03.031

Zeng, C., Jiang, H., Song, G. S., Li, C., Zhao, X. Y., Ren, Y., Xue, Z. W. 2024. Quantitative classification of velocity pulse-like ground motions based on an adaptive response spectrum-based decomposition method. Soil Dynamics and Earthquake Engineering. 2024, 177, 108419. http://10.1016/j.soildyn.2023.108419

Zhai, C. H., Chang Z. W., Li, S., Chen, Z. Q., Xie, L. L. 2013. Quantitative Identification of Near-Fault Pulse-Like Ground Motions Based on Energy. Bulletin of the Seismological Society of America, 2013, 103(5), 2591-2603. http://10.1785/0120120320

Zhai, C. H, Li, C. H, Kunnath, S, Wen, W. P. 2018. An efficient algorithm for identifying pulse-like ground motions based on significant velocity half-cycles. Earthquake Eng Struct Dyn, 2018, 47(3), 757-771. http://10.1002/eqe.2989

Zhou, H. X., Che, A. L., Zhu, R. J. 2022. Damage Evolution of Rock Slopes Under Seismic Motions Using Shaking Table Test. Rock Mechanics and Rock Engineering, 2022, 55(8): 4979-4997. http://10.1007/s00603-022-02921-9

Zhou, S. H., Chen, G. Q., Fang, L. G. 2016. Distribution Pattern of Landslides Triggered by the 2014 Ludian Earthquake of China: Implications for Regional Threshold Topography and the Seismogenic Fault Identification. ISPRS International Journal of Geo-Information, 2016, 5(4):46-68. http://10.3390/ijgi5040046

Zhang, M., Yin, Y. P., McSaveney, M. 2016. Dynamics of the 2008 earthquake-triggered Wenjiagou Creek rock avalanche, Qingping, Sichuan, China. Engineering Geology, 2016, 200, 75-87. http://dx.doi.org/10.1016/j.enggeo.2015.12.008